Enhance ZDDP Tribofilm Growth and Fatigue Lifetime of

Rolling Bearings by Laser Surface Texturing

Dissertation

Zur Erlangung des Grades

des Doktors der Ingenieurswissenschaften

der Naturwissenschaftlich-Technischen Fakultät

der Universität des Saarlandes

UNIVERSITÄT
DES
SAARLANDES

von

Chia-Jui Hsu

許 嘉 睿

Saarbrücken

September 2021

Tag des Kolloquiums: 14. Feb. 2022

Dekan: Univ.-Prof. Dr. rer. nat. Jörn Walter

Berichterstatter: Univ.-Prof. Dr. -Ing. Frank Mücklich

Univ.-Prof. Dr. -Ing. Dirk Bähre

Vorsitz: Univ.-Prof. Dr. Christian Motz

Akad. Mitarbeiter: Dr. -Ing. Frank Aubertin

『敦品、勵學、愛國、愛人』

"Integrity, Diligence, Fidelity, and Compassion"

Ssu-Nien FU 傅斯年

Zusammenfassung

Die Laseroberflächenstrukturierung (eng.: Laser Surface Texturing (LST)) ist ein schnelles und präzises oberflächentechnisches Verfahren, welches es erlaubt die Reibung von Maschinenelementen zu reduzieren und somit zur Steigerung der Energieeffizienz beiträgt. Außerdem können die LST-Strukturen die Verwendung eines üblichen Verschleißschutzadditivs wie Zinkdialkyldithiophosphat (ZDDP) unterstützen. Allerdings ist der Einsatz von LST im Grenzreibungsregime noch nicht etabliert. Ziel dieser Arbeit war es, die Lebensdauer von Wälzlagern unter Grenzreibung durch eine Kombination aus LST und ZDDP-Einsatz zu verlängern. Zunächst wurde die chemische Beschaffenheit der Verschleißschutz-Triboschicht charakterisiert. Messungen mittels Atomsonden-Tomographie zeigen eine Anreicherung von Schwefel in der Grenzschicht zwischen Grund und Gegenkörper. Darüber hinaus wurde nachgewiesen, dass die LST-Strukturen den Verschleiß aufgrund von Schmiermittelspeicherung und einer verstärkten Triboschichtbildung verringern. Die Druckverteilung auf einer strukturierten Oberfläche wurde durch eine Kontaktsimulation berechnet, und die Zunahme der Normalspannung führt zu einer Förderung des Triboschichtbildung. Schließlich zeigten die Wälzlager mit den LST-Strukturen eine dreifache Ermüdungslebensdauer.
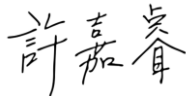
Abstract

Laser surface texturing (LST) is a fast and precise surface engineering method capable of improving the frictional performances of machine elements, thus contributing to an increase in energy efficiency. However, not many studies have carried out research of LST in the boundary lubrication regime, likely due to concerns of higher contact stresses that can occur with the increasing surface roughness. This study aims to improve the fatigue lifetime of rolling bearings in the boundary lubrication condition by LST combined with ZDDP-added lubrication. Firstly, the ZDDP antiwear tribofilm was characterized. The composition of the tribofilm and the difference between the blue- and the brown-colored region was revealed. Moreover, the analyses by high resolution methods indicated a sulfur enrichment at the interface between the tribofilm and the steel substrate. Secondly, the LST patterns were verified to reduce wear due to the capacity of lubricant storage and the enhanced growth of ZDDP tribofilm. The pressure distribution on the textured surface was calculated by a contact simulation, and the increase of normal stress led to a promotion of the tribofilm. Finally, the rolling bearings with the LST patterns demonstrated an increase in fatigue life.

Preface

This presented dissertation is an integration of my doctoral study in the Erasmus Mundus joint doctoral program, DocMASE, from 2015 to 2020. Chair of Functional Materials at Saarland University (Saarbrücken, Germany) hosted the project and made a strong collaboration with RWTH Aachen (Aachen, Germany), TU Wien (Vienna, Austria), and AC2T research GmbH (Wiener Neustadt, Austria).

The results of this dissertation are published in peer-review scientific journals, which are appended at the end.

許嘉睿

Chia-Jui HSU

Vienna, 2021

Included papers and contributions

1. C. Gachot, <u>C.J. Hsu</u>, S. Suárez, P. Grützmacher, A. Rosenkranz, A. Stratmann, G. Jacobs, "*Microstructural and Chemical Characterization of the Tribolayer Formation in Highly Loaded Cylindrical Roller Thrust Bearings*", Lubricants 4 (2016) 1-19

   Carried out the major part in the planning and characterizations, excepts TEM experiments where I participated, and wrote the paper of experiment and result sections.

2. <u>C.J. Hsu</u>, A. Stratmann, A. Rosenkranz, C. Gachot, "*Enhanced Growth of ZDDP-Based Tribofilms on Laser-Interference Patterned Cylinder Roller Bearings*", Lubricants 5 (2017) 39

   Carried out the LST on the bearings and the characterizing measurements, and wrote the paper.

3. <u>C.J. Hsu</u>, J. Barrirero, R. Merz, A. Stratmann, H. Aboulfadl, G. Jacobs, M. Kopnarski, F. Mücklich, C. Gachot, "*Revealing the interface nature of ZDDP tribofilm by X-ray photoelectron spectroscopy and atom probe tomography*", Ind. Lubr. Tribol. Vol. 72 No. 7 (2020) 923-930

   Carried out the major part of planning, and participated in the XPS and APT analyses. Wrote the paper.

4. <u>C.J. Hsu</u>, A. Stratmann, S. Medina, G. Jacobs, C. Gachot, "*Does Laser Surface Texturing Really Have a Negative Impact on the Fatigue Lifetime of Mechanical Components?*", Friction (2021), 1-10

   Carried out the major part of planning, LST production, and characterization. Participated in contact simulation and wrote the paper.

Experiences and Achievements

1. **Teaching:**
   - 2016 Practice of Material Science: *Radiography, CT-Scan, and XRF*
   - 2017 Practice of Material Science: *Radiography, CT-Scan, and XRF*
   - 2020 Guest Lecturer: *Lubrication and Lubricants*
   - 2021 Guest Lecturer: *Lubrication of Bearings and Oil Film Thickness*

2. **Grants & Awards:**
   - 2015-2017 Erasmus joint scholarship by Taiwan education ministry
   - 2016 Travel funding by GradUS of Saarland University
   - 2017 Travel funding by GradUS of Saarland University
   - 2020-2022 OeAD project funding programme Taiwan-Austria

3. **Presentation in International Conferences and Symposiums:**
   - 2016 Nordic Tribology Symposium (NordTrib), Hämeenlinna, Finland
   - 2017 World Tribology Congress (WTC), Peking, China
   - 2017 Gesellschaft für Tribologie Symposium (GfT), Göttingen, Germany
   - 2017 IMR meeting of European School of Materials in Saarbrücken, Germany
   - 2017 ÖTG-Symposium, Wiener Neustadt, Austria
   - 2018 Nordic Tribology Symposium (NordTrib), Uppsala, Sweden
   - 2018 Material Science and Engineering Congress (MSE), Darmstadt, Germany
   - 2018 ÖTG-Symposium, Wiener Neustadt, Austria
   - 2019 Leeds-Lyon Symposium on Tribology, Lyon, France
   - 2019 European Conference on Tribology (EcoTrib), Vienna, Austria

4. **Peer-reviewed Journal Publications:**
   - Gachot, C., Hsu, *et al.* (2016). *Lubricants*, *4*(2), 19.
   - Stratmann, A., Jacobs, G., *et al.* (2017). *Tribo. Inter.*, *113*, 43–49.
   - Hsu, C.-J., Stratmann, A., *et al.* (2017). *Lubricants*, *5*(4), 39.
   - Fang, S., Hsu, C.-J., *et al.* (2018). *Lubricants*, *6*(1), 11.
   - Fang, S., Klein, S., *et al.* (2019). *Int. J. Refract. Hard Met.*, *84*(May), 105034.
   - Hsu, C. J., Barrirero, J., *et al.* (2020). *Ind. Lubr. Tribo.*, *March*.
   - Faruck, A. A. M., Hsu, C.-J., *et al.* (2020). *Tribo. Inter.*, *151*, 106390.
   - Hsu, C.-J., Stratmann, *et al.* (2021). *Friction*, 1–10.

Acknowledgement

This dissertation gathers all the results and achievements in my doctoral journey. However, I wasn't alone on the way. Many people have pushed me forward and forward, and I would like to make the acknowledgement hereby.

Prof. Dr. Frank Mücklich, my scientific supervisor, is the one who provides me the possibility to launch my research career in his institute. It would not be possible to finish the study without his guidance. I sincerely express my greatest gratitude to him. Secondly, I want to thank Prof. Dr. Dirk Bähre as my scientific advisor for having constructive discussions and indicating those thinking blind spots of the scientific works. Furthermore, I'd like to particularly express my gratefulness to Prof. Dr. Carsten Gachot for leading and encouraging me through all the difficulties in my whole PhD life. He has motivated me with his always positive thinking and professional perspectives as a not only good coach but also a great friend.

Many supports for microstructural and chemical analyses were offered by Dr. Christoph Pauly, Dr. Jenifer Barrirero, Dr. Sebastián Suárez, and Dr. Hisham Aboulfadl. The dissertation has been completed along with the participation of Dr. Simon Medina, Dr. Ching-An Cheng, and Dr. Philipp Grützmacher, for the theory build-up and the writing corrections. I truly appreciate their contributions from different specialties, which completes this doctoral work.

Aside from the scientific diligence, I am grateful to the lovely FuWe, which is like my second home in Europe, especially to my office mates Dr. Idriss El Azhari and Sebastian Slawik, and the laser-buddy, Dr. Jiaqi Luo. Special thanks shall be given to Dr. Shiqi Fang for all the cooperation in science and life. In addition, my colleagues and friends in TU Wien and AC2T have supported me in finishing the dissertation in the second half of the journey; particularly, that was a great time working with Hakan Göcerler and Azhaarudeen A. M. Faruck.

Finally, a sincere thank shall be given to my dearest family, Lih-Jong, Mei-Fen, Chia-Lin, Chia-Hsiang, and Aiwen, for the unrequited support, especially in such a tough pandemic time.

Abbreviations and Symbols

2D	Two dimensions
3D	Three dimensions
A_p	Material volume in peak zone
APT	Atom probe tomography
A_v	Void volume in valley zone
AW	Antiwear
BEM	Boundary element method
CCD	Charge-coupled device
CLA	Centerline average
COF	Coefficient of friction
CV	Continuous wave
D	Thermal diffusivity
DLIP	Direct laser interference patterning
EHL	Elasto-hydrodynamic lubrication
EP	Extreme pressure
FEM	Finite element method
FIB	Focus ion beam
G	Dimensionless materials parameter
h_0	Lubricant film thickness
$\mathbf{H_m}$	Dimensionless minimum film thickness
HSAB	Hard and soft acids and bases
I	Intensity
I_0	Initial intensity
l_{th}	Thermal diffusion length
LST	Laser surface texturing
Mr1, Mr2	Material ratio in peak/valley zone
n	Sampling numbers
P	Period of the patterns
PSD	Position sensitive detector
PVD	Physical vapor deposition
R	Radius
RFC	Rolling fatigue c

R_a	Arithmetic average height
R_k	Core roughness depth
R_{pk}	Reduced peak height
R_q, RMS	Root mean square
R_{sk}	Skewness
R_{vk}	Reduced valley depth
SAED	Selected area electron diffraction
SEI	Secondary electron image
SEM	Scanning electron microscopy
TEM	Transmission electron microscopy
TOF	Time of flight
U	Dimensionless speed parameter
W	Dimensionless load parameter
WLI	White light interferometry
XPS	X-ray photo spectrometry
z	Depth
ZDDP	Zinc dialkyldithiophosphate
α	Incident angle
β	Absorption coefficient
σ_1, σ_2	Roughness
λ	Lambda parameter
λ_L	Wavelength of laser
τ	Pulse duration

Table of Contents

1. Motivation

Severe changes in the global climate and the foreseeable shortage of fossil fuels have raised the importance of energy efficiency. If the energy efficiency improves, then greenhouse gas emissions will be reduced, and the process of global warming would slow down. A major source of greenhouse gas emission comes from end-user applications, such as transportation and industry (see Figure 1) [1–3]. From the perspective of tribology, the CO_2 emission issue can be attributed in part to the energy loss caused by wear and friction [4–6]. In other words, improvement of tribological performance can enable efficient energy use.
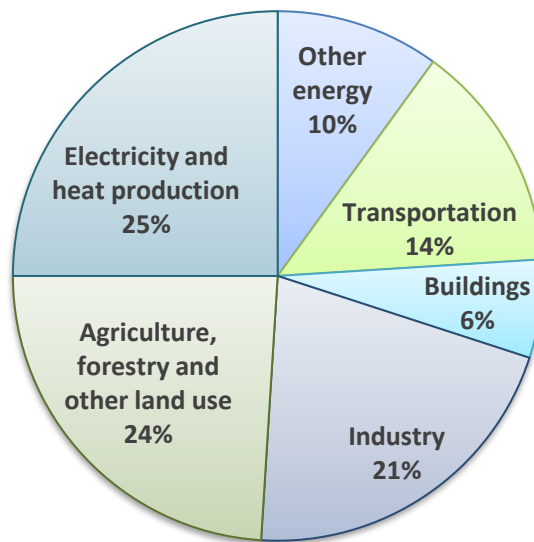

Figure 1: Percentage of global greenhouse gas emission by economy sector according to [2].

The energy costs due to wear and friction are considerable, as wear and friction may lead to damages, material losses, and heat. Take passenger cars as an example, Holmberg and Erdemir [2] show that the energy loss caused by friction is around 16.5%; only 21.5% of the energy generated from fuel was actual for car moving (see Figure 2). On the bright side, the statistical result also indicates that the use of modern tribology technologies could reduce friction losses in passenger cars by 18% in the short term (5-10 years) and by 61% in the long term (15-25 years) [7]. It is clear that novel friction solutions such as new lubricants and protection coatings can improve energy efficiency [8–12].
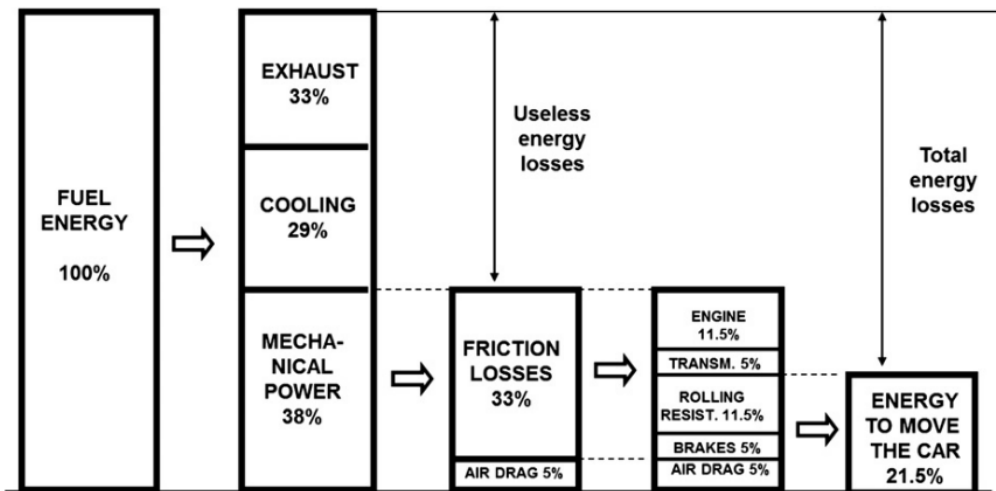

Figure 2: Energy consumption of a passenger car showing categories of losses from fuel to motion [13].

Apart from friction, wear is a major factor that increases energy loss of mechanical components by decreasing components' lifetime [14–16]. Wear damage, which causes material and energy losses, usually occurs when a heavy load is applied with only a little amount of lubricant in between. Such *boundary lubrication* regime is typical in industrial applications like bearings and gears [17–24] and is formally defined, according to the Stribeck curve [25], as a lubricated condition with a small ratio of oil film thickness to mean roughness value, which happens mostly along with a high load and a low sliding speed [26–29].

Although, in principle, wear is unpreventable under boundary lubrication, it is well known that the formation of an antiwear (AW) tribofilm can provide protection to the contacting surfaces [22]. In particular, one of the most popular AW lubricant additive is ZDDP. Due to its excellent antiwear performance and inexpensive price, ZDDP has been widely utilized and studied for more than 70 years. These properties can help to provide protection against damage from wear and to extend the component's lifetime [30–34]. Even though the mechanism of the formation and the detailed reaction paths are still not well understood, the use of ZDDP is still dominant in commerce and industry [35,36]. In Figure 3, the formation of the ZDDP tribofilm by a tribochemical reaction is schematically shown.

Even though great success was established in the market with extraordinary performances, ZDDP produces sulfur, phosphorus oxides, and metal salts that are found harmful to engine exhausts [37–41]. Consequently, the tolerance of P and S has been limited lower than 0.5 and 0.08 wt.-%, respectively [30]. It is a difficult task to find a proper replacement considering the comprehensive performance of ZDDP. At least no research progress has been made to develop high-performance engine oils at a reasonable price until now [34,42–44]. Nevertheless, enhancing the effectiveness of ZDDP via surface engineering can further lower its consumption. Moreover, the continuous researches in the tribology community that investigate ZDDP will eventually approach a solution with low- or zero-ZDDP formulation [30,45–47].
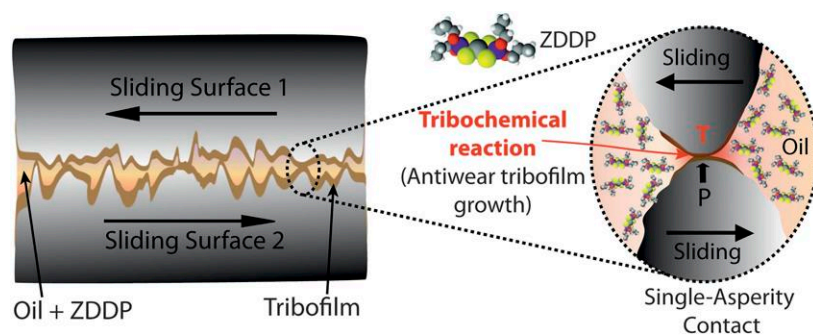

Figure 3: The tribo-chemical reactions of zinc dialkyldithiophosphate (ZDDP) with oil that undergo shear-assisted formation at the single-asperity scale [48].

Novel methods of surface engineering, such as laser surface texturing (LST), have been proven to be beneficial to reducing wear and friction, providing positive contributions in all lubrication conditions from boundary to hydrodynamic regimes [49,50,59–63,51–58]. LST usually creates regular or uniform patterns on the surfaces on a microscale. Some typical patterns produced by LST are shown in Figure 4. The created space can retain lubricants in the contact zone and then provide necessary lubrication to prevent insufficient lubrication; moreover, it can trap the harmful wear debris that causes wear to the contacting surfaces [64]. Laboratory tests have also shown that LST can improve the frictional performances in industrial applications such as roller bearings [50,65], ball bearings [66–68], valves [69,70], and pistons [71,72]. However, befitting texturing design for a specific application is still challenging that, in some cases, the increase of surface roughness is causing more wear [73–76]. Moreover, the combined use of LST and AW additives improves the tribological performances [4,59,62,77,78], which gives LST the potential to reduce wear even under boundary lubrication.
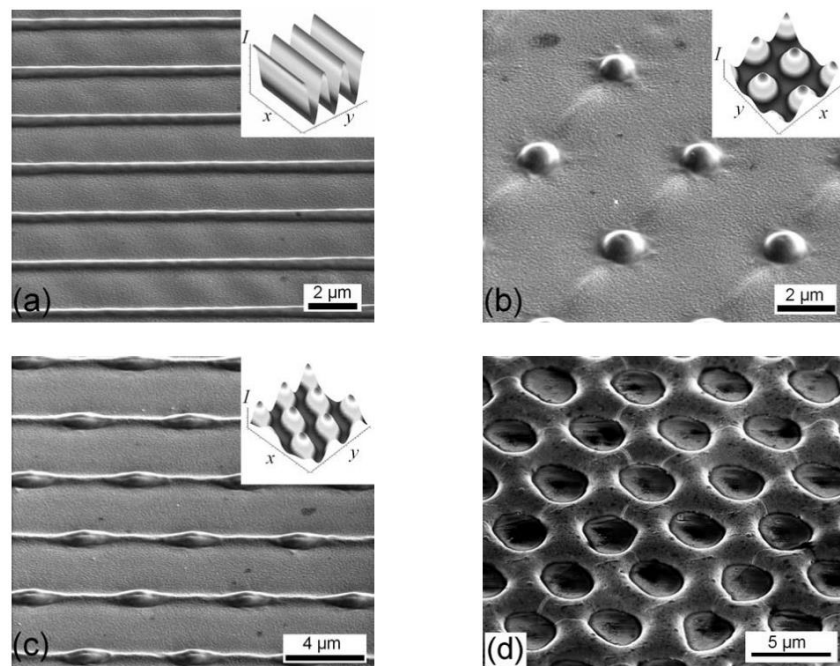

Figure 4: Various surface patterns textured by direct laser interference patterning (DLIP) of laser surface texturing (LST). (a) line-like pattern by 2-beam interference; (b)-(d) dot-like patterns by 3-beam interference with a difference incident angle [79].

Typical cases in the industry that face heavy load and wear are rolling bearings. The rolling bearings are used for supporting a rotating shaft, resisting radial or axial load, and adopt spherical balls or various types of rollers between the stationary and the moving elements. A section view of a thrust cylindrical roller bearing is shown in Figure 5. The life of rolling bearings with rolling/sliding contact is often limited due to the occurrence of pitting failure [80–82]. Pitting failures are initiated by micro-cracks, and the growth of the cracks eventually leads to rolling contact fatigue (RCF). Pitting failure can be categorized by the location of the micro-cracks: either in the sub-surface zone or on the surface of the material. Sub-surface failures have become less frequent due to improvements in steelworks, which has decreased the number of inclusions [80,83,84]. However, surface-initiated pitting, which begins with cracks initiated by defects, wear debris, or asperities on the surface, has caused a rising percentage of failures in modern applications [85]. This is attributed to the lower thickness of oil film that occurs when pursuing efficiency via reducing lubricant viscosity or adopting higher machining power, which makes the machine components operate in the boundary lubrication condition [86–88].

Figure 5: Cylindrical roller thrust bearing type 81212 used for tribological trials.

This study aims to improve the lifetime of rolling bearings by a combined approach using LST and ZDDP. The first half focuses on the chemical and structural characterization of the ZDDP tribofilm, and these high-resolution examinations provide deeper insight into the formation mechanisms of the antiwear tribofilm, by which a sustainable replacement of ZDDP

can be approached. The second half focuses on using LST to improve the frictional performances of the thrust rolling bearings. Four LST patterns will be initially tested for performance in terms of wear, and the best of these designs will be used for the subsequent fatigue tests. The correlated behavior of the ZDDP as an additive to the Laser textured surface will be finally evaluated.

2.   State of the art

This chapter provides the fundamentals and the up-to-date knowledge for understanding the approaches used in this dissertation. Because this study aims to improve the frictional performances of rolling bearings by means of LST, it is essential to introduce the theory of tribology and surface engineering so that the influencing factors to the frictional performances can be described precisely. For instance, roughness parameters calculated on the surface profiles can numerically describe the surface morphology. In addition, the calculation of oil film thickness can determine the classification of different lubrication conditions. Particularly, the common failure mechanisms of rolling bearings will be discussed, and the solution to reduce seizures of surface failure can be provided. Finally, the principle of laser technology and how it reacts with materials will be demonstrated.

2.1. Tribology

2.1.1. Tribosystem

Combining engineering, materials, and chemistry, tribology is the science of friction, wear, and lubrication. The study of tribology is fundamentally about materials, surfaces and lubrication, and the interplay that determines the wear and friction [89]. Tribological investigations are for the purpose of better controlling wear and friction by manipulating mechanical, interface, and material parameters [90,91]. The complicated tribological state can be simplified and described as a tribosystem.
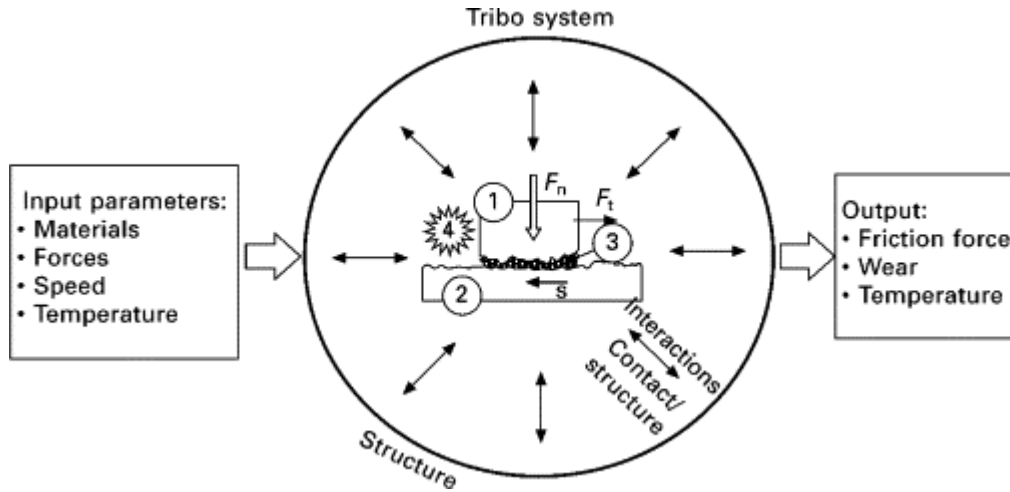
Figure 6: Diagram of a tribosystem consisting of: (1) and (2) material pair; (3) interface; (4) environment [90].

A tribosystem (see Figure 6) consists of four elements, including a pair of contacting materials (substrate and counter-body), the interface between the material pair, and the environment [90,92]. The interface describes the lubrication condition and the third body, of which the major part is the wear debris/particle. The environment consists of temperature, humidity, and operational parameters, such as applied load and deployed motion kinematics. By manipulating the input parameters such as force, speed, working temperature, and material properties, the tribosystem performs different outputs [90,93].

Friction is the force parallel to the contact interface that resists the relative motion of the contacting bodies. The magnitude of the friction force depends on the material characteristics of the two contacting surfaces [94,95]. Depending on the contact mode, the friction can be further classified as sliding friction, rolling friction, static friction and etc. [96]. Moreover, under lubricated conditions, friction is then mainly determined by viscosity. The properties of lubricant affect the surface interaction, and more details about lubrication conditions can be found in section 2.1.3.

2.1.2. Surface Roughness Parameters

Surface roughness is widely used as an index showing product quality, which shows the height of the asperities present on the surface over a length or an area [97,98]. It is also considered as an important factor to the tribological performance of the contacting surfaces, given that a higher roughness usually results in a higher wear rate [99–101]. By using profilometric methods, surface roughness can be calculated quantitatively in terms of *roughness parameters*, which describe the profile of surface topography. Especially for surface engineering, the roughness parameters can determine the quality of processing [102,103].
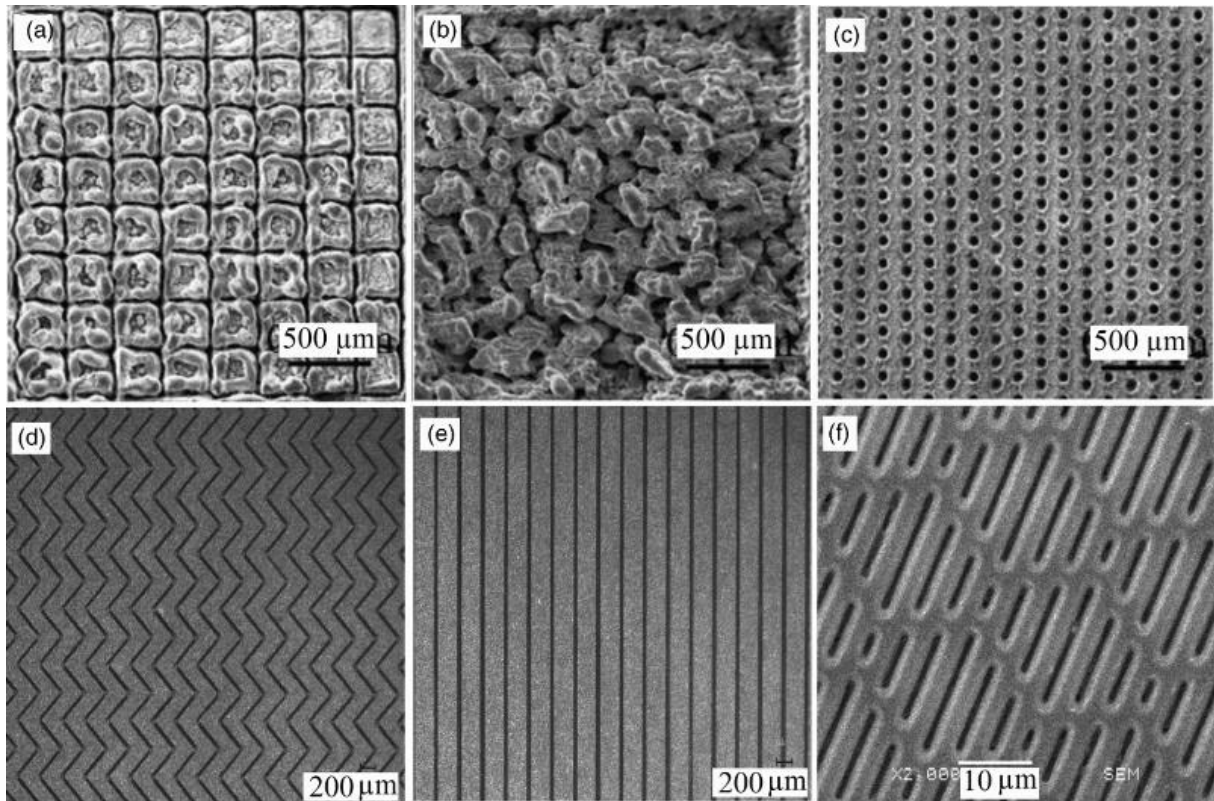

Figure 7: SEM images of LST patterns under different processing scales: (a) grid, (b) chaotic, (c) dimple, (d) wavy groove, (e) linear groove, and (f) riblet [104].

LST creates dimples, lines, and some more complex geometric patterns onto the components' surfaces at different scales from macroscopic to microscopic levels (see Figure 7).

The patterns can be demonstrated using surface profiles obtained by optic microscopy or profilometry; however, only surface profiles cannot quantify and exhibit the details of the patterns. Therefore, the height distribution and spatial profile of surfaces are better described by statistical functions, that the surface morphology can be quantitatively assessed. For example, one of the main characteristics of LST patterns is lubricant storage, which is positively related to the volume of valleys [4]. Roughness parameters such as R_{vk} and A_v are usually used for assessing the capability of lubricant storage [105]. Based on the focus of the present study, the roughness parameters related to the assessment of LST patterns will be introduced. The values of the roughness parameters are obtained and calculated by white light interferometry (WLI).
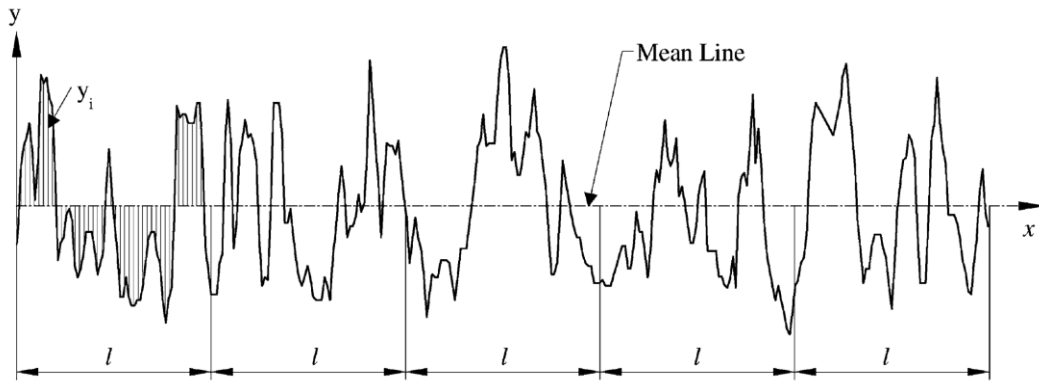

Figure 8: Definition of the arithmetic average height (R_a) [106].

The arithmetic average height (R_a) and root mean square (RMS) are the most common roughness parameters for surface examination. For grinded and LST patterned surfaces, these two parameters indicate the height variation. Firstly, R_a, also known as the centerline average (CLA), is defined as the average absolute deviation of the height difference from the mean line over a sampling length l and sampling numbers n (see Figure 8), which has its limit of less sensitivity to small changes in profile. The mathematical definition is shown as follows:

$$R_a = \frac{1}{n}\sum_{i=1}^{n}|y_i| \qquad (2.1)$$

The root mean square roughness (RMS), which is also called as R_q, the standard deviation of the distribution of surface heights. Both R_a and RMS described surface roughness, but each is calculated differently. R_a is calculated as a value of roughness average, and RMS is calculated as the root mean square. According to the formulars, RMS is more sensitive to the peaks and valleys than R_a. The mathematical definition of this parameter is as follows:

$$RMS = \sqrt{\frac{1}{n}\sum_{i=1}^{n} y_i{}^2} \qquad (2.2)$$

The skewness value is used to determine the symmetry of the profile to the mean line, and it is sensitive to occasional peaks such as high spikes or deep valleys. When the bulk of the material is above the mean line, as shown in Figure 9, the R_{sk} valve is negatively skewed, indicating a plateau-like surface. In contrast, a positive value represents a bearing surface with the main bulk material beneath the mean line.
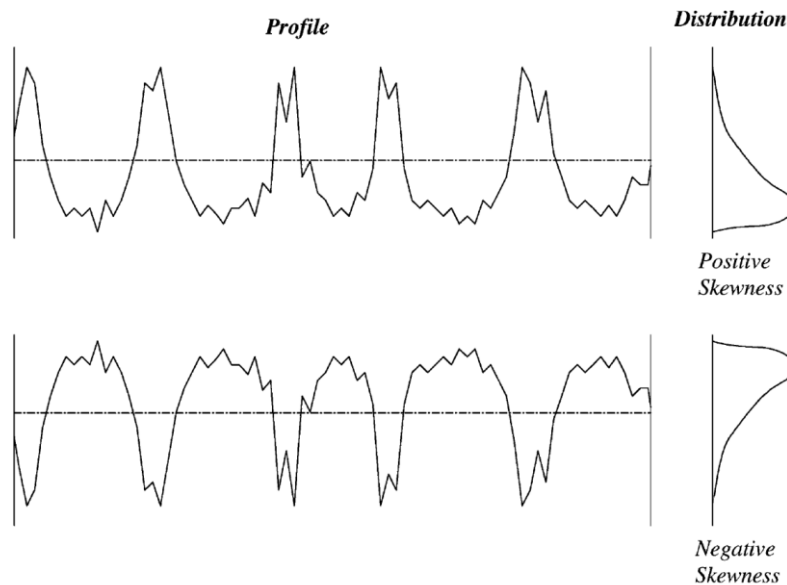

Figure 9: Definition of skewness (R_{sk}) and the amplitude distribution curve. Peaked surfaces (top) having a positive value and bearing surfaces (bottom) with a negative value [106].

The skewness value calculates the third central moment of the profile density function, and its mathematical formula is as follows:

$$R_{sk} = \frac{1}{n(RMS)^3} \sum_{i=1}^{n} y_i{}^3 \tag{2.3}$$

where y_i is the height of the profile at point i, and the number of points is n. Sometimes two different surfaces have a same value of R_a and RMS, and thus R_{sk} can be used to differentiate them. For the use of LST, the capability for lubricant storage can be evaluated by R_{sk}.
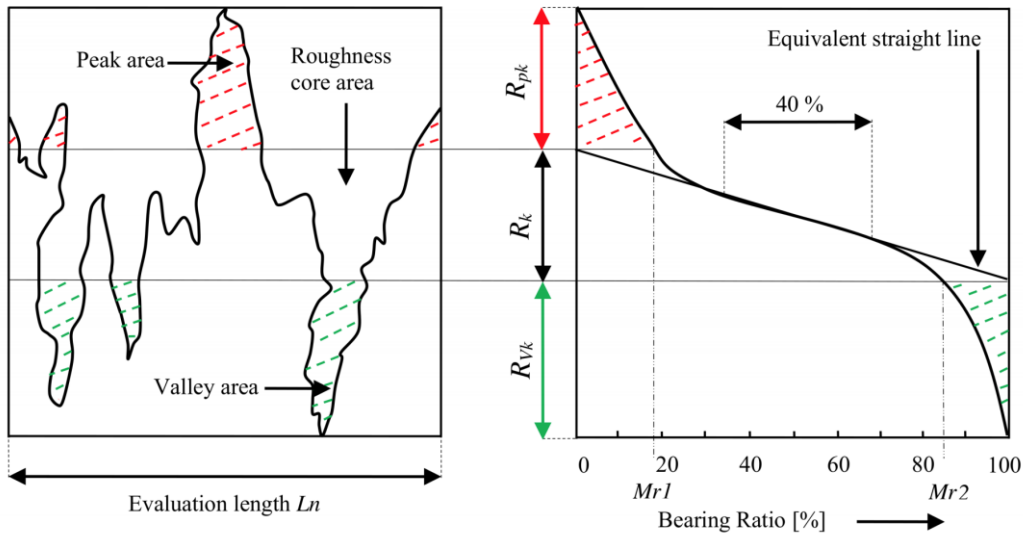

Figure 10: Definition of the bearing area curve (Abbott-Firestone curve) [107].

In addition to height parameters, the bearing capability of surfaces can be drawn as a bearing ratio curve, which is also called the Abbott-Firestone curve (as shown in Figure 10). The horizontal axis represents the bearing area lengths as the percentage of the sampling length of the profile, and the vertical axis represents the heights of the profile. The measured parameters of the curve from top to bottom are: R_{pk}, the reduced peak height; R_k, the core roughness depth; and R_{vk}, the reduced valley depth. Moreover, M_{r1} and M_{r2} of the plot indicate the boundary of peak-to-core and core-to-valley; and the triangle regions shown in red and green color represent the quantity of solid height and valley, which are A_p and A_v, respectively.

For assessing tribological performances, lower R_{pk} represents a smoother surface (fewer asperities), which can usually result in lower friction in the running-in process [108,109]. In addition, greater R_{vk} indicates more portion of valleys, which has been suggested as an index of the ability for lubricant storage [110–112].
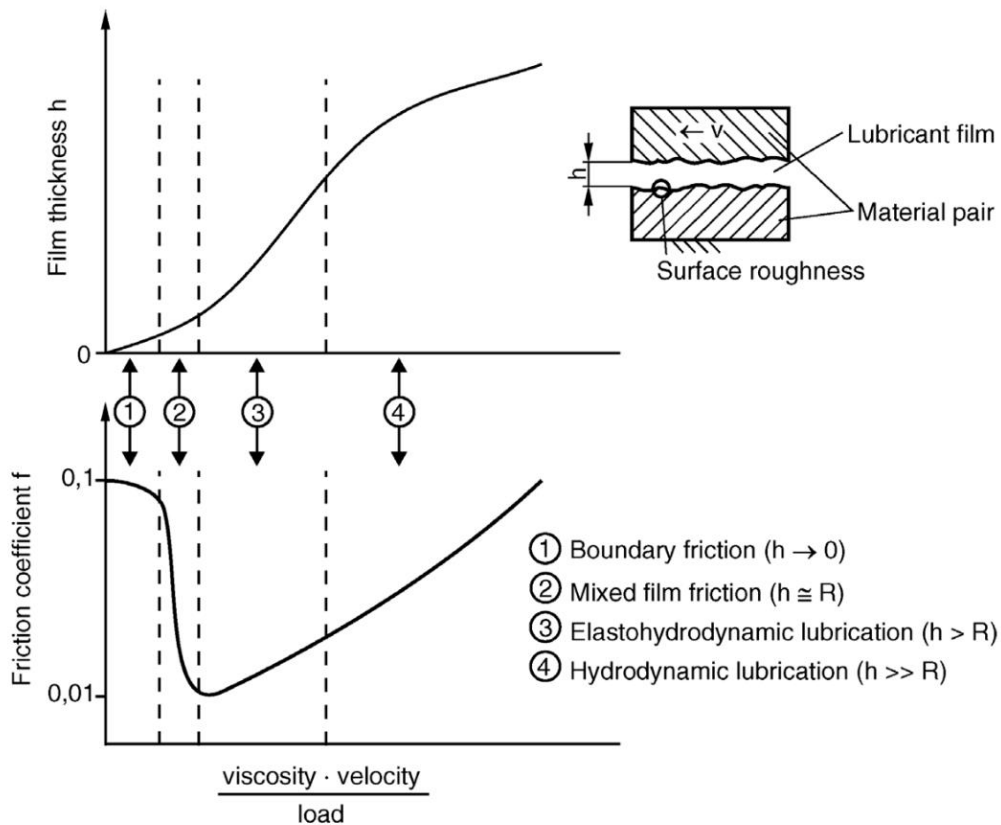
2.1.3. Lubrication Conditions

Figure 11: Stribeck curve showing different lubrication regimes from boundary, mixed, and to hydrodynamic lubrication [96]. (h: lubricant film thickness; R: surface roughness; v: relative speed)

The primary purpose of lubrication is to reduce friction between contacting surfaces in relative motion and carry heat and wear particles away [96,113]. An ideal lubrication condition

is to separate the two surfaces completely with a film of low friction materials such as oil or pumped gases [114–116]. The relationship of the film thickness and asperities of the contact surfaces influences the lubrication condition, which is demonstrated in the Stribeck curve (see Figure 11). The resulting oil film thickness can be controlled by the relative velocity of the surfaces in contact, the applied load, and the viscosity of the lubricant.

The lubrication regime is classified by the lambda ratio, which is oil film thickness divided by the composite surface roughness; and it is called dry contact when no lubricant is involved. With h_{min} and the respective roughness values, the lambda parameter could be calculated, which is used as an indicator of the lubrication condition:

$$\lambda = \frac{h_{min}}{\sqrt{\sigma_1{}^2 + \sigma_2{}^2}} \tag{2.4}$$

From a fully supplied lubrication to an insufficient case, the lubrication regimes of a rolling/sliding tribosystem can be determined as follows: hydrodynamic, EHL, mixed, and boundary lubrication; which is according to Hamrock et al. [117]. Firstly, when a thick film of lubricant is formed ($\lambda > 3$), there is no direct contact between two surfaces; this is called hydrodynamic lubrication (HD). A thick oil film provides positive pressure to separate the surfaces and support the applied normal load. Therefore, the properties of the lubricant such as viscosity and cooling ability are essential in the HD regime [118,119]. In this lubrication regime, the lubrication model can be calculated by Reynold's equation of fluid dynamics.

Boundary lubrication takes place when fluid film can no longer separate the contact surfaces ($1 > \lambda$). Friction and wear rate rise higher than in HD since the fluid film effects are negligible and the asperity contact is predominant [117,120,121]. Furthermore, when the film thickness and the roughness are nearly equal ($3 > \lambda > 1$), a mixed lubrication condition can be found within the contact, where HD lubrication and asperity contacts coexist [122,123].

When two surfaces encountering in a point or a line contact, the contact pressure increases due to a small contact area and thus demonstrates an EHL lubrication ($10 > \lambda > 2$) [96,124]. Concentrated and non-conformal contact leads to a high peak of pressure, and thus hydrodynamic lubrication can no longer support the focused pressure. Lubricant film still forms

and has a comparable thickness to the surface roughness. The high pressure causes elastic flattening of the contacting surfaces and results in a locally conforming contact [87,125]. Moreover, the high pressure also raises the viscosity of the lubricant, benefiting the thickening of the oil film [4].

The value of minimum oil film thickness h_{min} is necessary for assessing the lubrication condition, and can be optically observed by using transparent tools. However, tribosystems are usually non-transparent and even covered by other elements, which makes the contact not able to be observed. In practice, the minimum oil film thickness can be estimated according to the Dowson-Higginson equation [116,125]:

$$\boldsymbol{H_{min}} = 1.6\,\boldsymbol{G}^{0.6}\,\boldsymbol{U}^{0.7}\,\boldsymbol{W}^{-0.13} \tag{2.5}$$

$$h_{min} = \boldsymbol{H_{min}} \times R \tag{2.6}$$

where $\boldsymbol{G}$, $\boldsymbol{U}$ and $\boldsymbol{W}$ are the dimensionless parameters of line contact, which refer to the properties of the materials, sliding speed, and load, respectively. The parameter h_{min} represents the prediction of the minimum oil film thickness at the contact zone, whereas R is the radius of the counter body.

2.1.4. Boundary Lubrication

An ideal form of lubrication would be the HD regime, since it provides low friction and high resistance to wear [117]. However, when the load is heavy and/or the speed is low, the HD pressure may not be sufficient for supporting the load [22]. Boundary lubrication usually occurs in many industrial application, for instance: bearings, gears, cam and tappet interfaces, piston ring and liner interfaces, pumps, and transmission [126–128]. Moreover, in many cases, it is this critical lubrication regime that governs the life of the components [17,129].

Direct contact raises friction and wear, which can lead to starved lubrication due to insufficient oil supply [87,124]. Note that it is more common to find machine elements operating in mixed than boundary lubrication [123]. Only when the applied load is extremely

heavy, or the sliding speed is too low, boundary lubrication can be found. As a consequence, the wear rate can increase up to 3 orders of magnitude compared with the mixed lubrication regime [130]. In order to avoid wear, AW additive is used to generate tribofilm for protecting surfaces.

AW tribofilm can be introduced by adding lubricant additives in the lubricants, which decreases shear force and prevents asperity contact [45,131,132]. The protective tribofilm formed by physical adsorption and tribochemical reaction acts as a barrier to prevent direct contact, thus decreasing the wear rate and friction. Two main classes of boundary lubrication additives are AW and extreme pressure (EP) agents. AW additives are used to protect the surface against wear loss, and EP additives to prevent failures under extreme pressure. The structure of the additives can be described as a functional core and a tail, such as sulfur/phosphor and alkyl chains, respectively [133]. Among all the commercial products, one of the most successful AW additives is called zinc dialkyldithiophosphate (ZDDP).

2.1.5. Zinc Dialkyldithiophosphate (ZDDP)

ZDDP is one of the most successful lubricant additives ever invented and has been employed especially for engine oil for more than 70 years. The triple role as antioxidant, corrosion inhibitor, and antiwear agent makes this AW additive long-lasting in the market [30]. However, for environmental issues and sustainability, the use of ZDDP has been restricted under global consensus. As mentioned in the previous chapter, it is a difficult task, and there is still no other competitive product at a reasonable price still [34,42–44]. Nevertheless, the continuous research in the tribology community that investigates ZDDP will eventually approach a sustainable solution with low- or zero-ZDDP formulation [30,45–47].
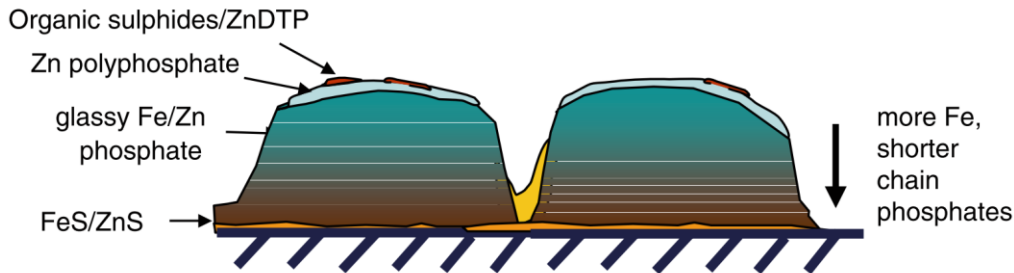
Figure 12: Schematic diagram of ZDDP tribofilm with chemical composition. [30]

The formation of the ZDDP antiwear tribofilm is the hinge for wear-resisting, and the origin of the layer formation is based on the energy input [41] that shear forces and increased temperature can cause the tribo-chemical reaction. On one side, thermal degradation of ZDDP occurs when the temperature is above 50°C and deposits a thermal film by adsorption [134,135]. On the other hand, sliding motion introduces pressure and relative motion, and that leads to tribofilm formation [136–138]. It is suggested that the formation of the tribofilm builds upon thermal film [139]; however, recent works indicate that the tribofilm can be generated without the participant of the thermal film [140]. Moreover, the growth of pressure-induced tribofilm is confirmed to be more efficient [141]. Compared to the thermally induced film, the tribo-generated tribofilm is more stable and has better tribological performances [137].

The presence of the ZDDP tribofilm reduces friction and wear [126,137,142], and thus extends the component's lifetime. ZDDP tribofilm is usually described as blue and brown-colored patchy layers formed in the sliding contact region, which is island-like with a thickness of around 100 nm and width from 0.5 to several micrometers [30,143]. An overview of the chemical composition can be found in Figure 12, which was built upon the theoretical and experimental results [30]. Basically, ZDDP-related elements (Zn, P, and S) can be found mixed with iron compounds. Longer chains of zinc/iron polyphosphates were found at the top of the tribofilm compared to shorter chains at the bottom region [144–146].

The main body (bulk) of the ZDDP tribofilm has been observed to contain a high concentration of oxygen usually. For instance, Martin *et al.* [147] found approximately 40 at.-% of oxygen in the tribofilm and a small amount of sulfur at the top layers. Guo *et al.* [148] also identified an iron oxide layer at the bottom of the tribofilm. Hence, by the cross-section

observation, Miranda-Medina *et al.* [149] indicated that the content of oxygen in the tribofilm can be due to the accumulated wear debris that mainly consists of iron oxide particles.
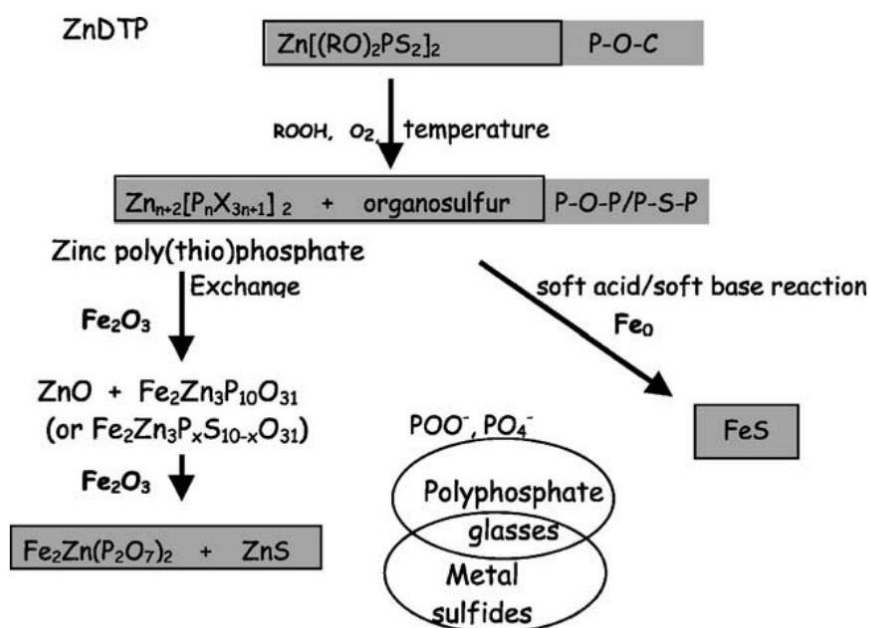

Figure 13: Different phosphates and sulfur species of AW additive by chemical reactions based on the HSAB principle. [150]

Similar to oxygen, sulfur has also been considered as a common element included in the tribofilm; however, the content and the distribution of sulfur compounds are still unclear to the community. Firstly, Martin *et al.* [151] proposed the Hard and Soft Acids and Bases (HSAB) principle to predict the chemical reactions of the formation of AW tribofilm (see Figure 13). Based on the principle, the tribofilm formation was initiated by the chemical reaction between sulfur and nascent steel substrate, which could produce an interlayer enriched of FeS. Correspondingly, Smith and Bell *et al.* [152,153] observed S/O layer in the bottom of the tribofilm. Moreover, Spikes *et al.* [154] indicated that a thin film of S enrichment was found at the initial state of sliding but afterward pushed out from the contact zone and replaced by P- and Zn-riched film. Soltanahmadi *et al.*[155] used transmission electron microscopy/ energy dispersive x-ray spectroscopy (TEM/EDS) to visualize the sulfur interlayer. Moreover, the higher content of sulfur/oxygen at the bottom side of the bulk tribofilm was commonly found

by using X-ray photoelectron spectroscopy (XPS) [128,156]. However, there are still some studies claiming that no sulfur interlayer was identified [147,151,157], which leaves the existence of the S enrichment at the interface still ambiguous. The difficulties of identifying the interface nature of the tribofilm can be attributed to the nano thickness and the complex mixture of oxygen and sulfur.

2.2. Laser Surface Patterning

2.2.1. Laser physics

Laser has been widely used in various applications, such as spectroscopy, manufacturing, profilometry scanning, and even entertaining, due to its unique properties: monochromaticity, directionality, coherence, and high intensity. The word "Laser" is an abbreviation for Light Amplification by Stimulated Emission of Radiation. Einstein predicted the stimulated emission phenomenon in 1916, and Schawlow and Townes originally proposed the development of the technique in 1958 [158]. The phenomenon of stimulated emission is fundamental for establishing a laser system. When an incoming photon of a corresponding frequency strikes an excited electron, it will drop to a lower energy level and emit a stimulated photon at the same time. The stimulated photons are in phase and traveling in the same direction as the stimulating photons [159,160], which can be applied for optical amplification.
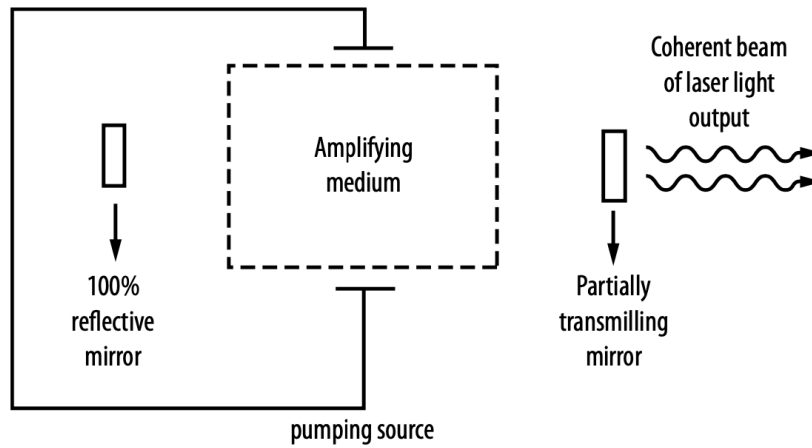
Figure 14: Schematic diagram of typical laser system [160].

A typical laser system is shown in Figure 14. In general, a basic laser set-up requires four essential components in its cavity: gain medium, pumping, high reflector, and partial reflector [160]. The gain medium is the core of the system, which serves as a means to amplify light. The gain medium is activated into an excited state for stimulated emission by an external pumping source. Many materials can be used to show the stimulated emission phenomenon, but only a few have significant power capability. Conventional laser medium can be in any physical state, such as CO_2 (gas), He-Ne (gas), organic dye (liquid), Nd-YAG (solid), excimer (solid), and diode lasers (semiconductor) [161,162]. The gain medium is activated by external pumping, and a typical pumping source can be flash lamps, electromagnetic fields, chemical reactions, or a pump laser. Moreover, the resonator of a laser cavity is composed of two reflectors at both ends: a fully reflective mirror and a partially transmitting mirror. The coherent laser beam is resonated in the cavity, and the output emits through the partially transmitting mirror.

Three interactions occur when electromagnetic radiation hits a surface: reflection, absorption, and transmission. The absorption can be described by the Lambert-Beer's law that the intensity *I* at a specific depth z as:

$$I(z) = I_0 e^{-\beta z} \qquad\qquad (2.7)$$

Dissertation, Chia-Jui HSU

where β is the absorption coefficient based on the material characteristics and the properties of the radiation. I_o is the intensity of the radiation just beneath the surface that excluded the reflection. The interaction between material and laser radiation is due to the absorption [163,164]. Sufficient energy absorption makes the material melt and further causes evaporation and plasma [165]. In addition, also the laser characters affect the absorption rate, such as wavelength, environmental temperature, angle of incidence, and surface roughness. Steel, for example, has an absorption rate to the laser of 527 nm wavelength approximately 10% higher than 1053 nm [166]. In addition, the continuity of laser beams, namely continuous wave (CV) or pulsed laser, causes different reaction mechanisms, which will be further explained in the following section.

2.2.2. Pulsed Laser

A pulsed laser is defined as a laser with beam energy that appears in pulses at specific repetition rates, and an ultrashort pulsed laser is with pulse duration less than 10 ps [167]. The use of short and ultrashort pulsed lasers is an emerging technology in the field of surface engineering [168]. The extreme energy intensities and a shorter exposure timescale influence the laser-material response. In addition, the advantages of using pulsed lasers included the reduction of lateral thermal effects, more precise threshold fluences of ablation, and reduced material redeposition [169,170]. Compared to CV lasers, the use of pulsed lasers reduces lateral thermal damage and lower heat-affected zone [168], since the thermal effect distance is defined by:

$$l_{th} = \sqrt{2D\tau} \qquad (2.8)$$

where D is the thermal diffusivity and τ is the pulse duration. When the pulse duration is sufficiently short, the thermal effect distance l_{th} will be very small. The power density of a pulse will determine the proportion of the energy that will be absorbed to either evaporate or to melt [171,172]. Theoretically, take aluminum substrate for example, the depth of the heat-affected zone is less than 2 μm when interacting with ultrashort pulsed laser [173].
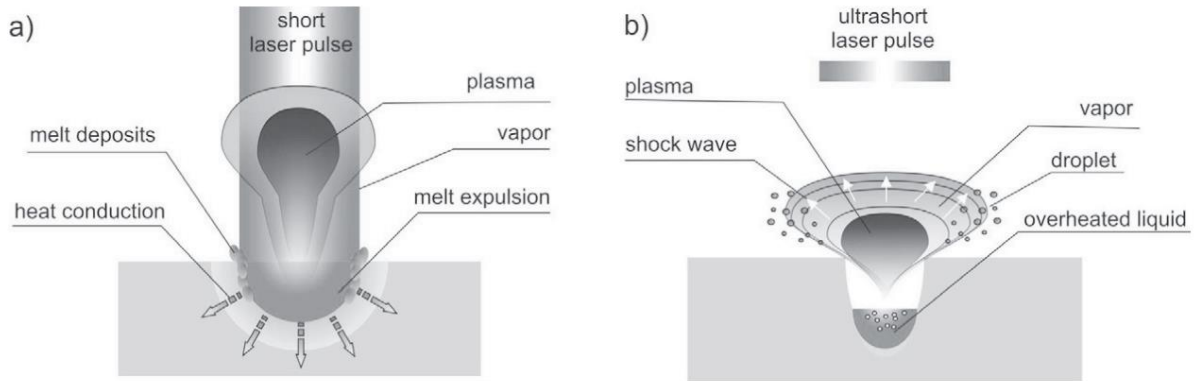
Figure 15: Material-Laser interaction with (a) short; (b) ultrashort pulsed laser. [174]

The laser-to-material interaction differs from a short to an ultrashort pulsed laser, where the latter is defined as equal or less than 10 ps. In Figure 15, the laser-material interactions between different short pulse durations are presented [174]. When a laser beam interacts with a metal, electrons are excited at high temperatures by the absorption of photon energy. Subsequent electron-phonon interactions transfer the absorbed energy to the lattice in a time frame of picoseconds for most materials. Consequently, for ultrashort pulsed laser with a pulse duration shorter than 10 ps, there is insufficient time for the energy transfer to the lattice. Due to the lack of heat transfer, the thermally affected region is minimal, and some materials evaporate directly without melting when the energy is high enough to break the bonds. Because the atoms have too little time to move during the pulses, very high pressures and high temperatures can be attained [168,175]. The difference of the laser-material interaction between short and ultrashort pulsed laser determines machining quality [176]. In a brief summary, materials behave conforming to the classic heat conduction and then melt or evaporate depending on the temperature achieved by micro- or nanosecond pulsed laser (Figure 15a). On the other hand, for the ultra-short pulsed laser such as pico- and femtosecond, materials transform from solid to vapor directly, and those overheated liquid blasts and causes liquid droplets and vapor (Figure 15b).

2.2.3. Laser Surface Texturing (LST)

Surface engineering for tailoring topography/roughness of surface has been proven to effectively reduce friction and wear in the last 70 years [50]. Due to the properties of highly directional, high power density, and precise focusing characteristics, laser has been considered to be a candidate for surface engineering [64,79,177]. The introduction of laser to surface engineering can be traced back to Etsion *et al.*, who started a comprehensive study on the use of laser surface texturing (LST) [178]. Since then, the tribology community has increasingly put attention on laser texturing due to the potential friction and wear reduction by using LST [62,64,179]. The successes from the laboratory tests have also demonstrated tribological improvements in industrial applications such as roller bearings [65], ball bearings [66], valves [69], and pistons [71]. An example of LST on the thrust roller bearing is shown in Figure 16.
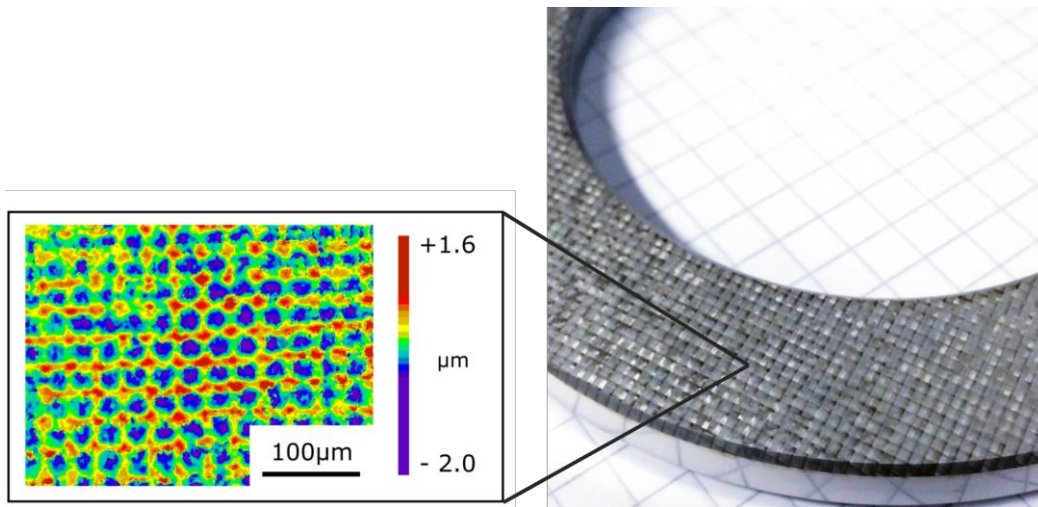

Figure 16: Surface morphology of a laser textured thrust roller bearing (lower washer) with cross-like periodic patterns having periodicity of 30 μm textured by DLIP.

The improvement and the mechanism of wear and friction reduction by surface texturing vary depending on the acting lubrication regime [50]. Under dry contact, LST stores the harmful wear particles, thus reducing severe abrasive wear. The decrease of real contact area reduces the frictional force; however, it also causes higher contact stress, which can increase the wear rate [180–182]. In lubricated conditions, the effect of LST should be discussed under the

aforementioned lubrication regime, namely HD ($\lambda > 3$), mixed ($3 > \lambda > 1$), and boundary ($1 > \lambda$) regimes. In general, the unique topography of the laser patterns can retain lubricants in the contact zone, thus providing necessary lubrication when the external supply is insufficient [50]. In addition, the ability to trap harmful wear debris also reduces wear in the lubricated cases [64] (The definition of the lubrication regimes is shown in Section 2.1.3.). In the HD lubrication regime, surface texturing typically provides an additional hydrodynamic pressure, thus generating a significant contribution to the load-bearing capacity [183–185]. It is suggested that the use of LST improves frictional performance under the HD regime [50], and the underlying mechanisms have been comprehensively studied by experiments and numerical simulations [59,186]. Secondly, in the mixed lubrication regime, the contact pressure is partially loaded on the oil film and the surface asperities. Since the thickness of the supporting oil film is thinner in mixed lubrication, the laser textured patterns acting as micro-reservoirs are more essential to prevent insufficient lubrication. The last lubrication regime, boundary lubrication, is similar to dry contact, in which the solid-solid contact is dominant. The wear occurs unpreventably, and an AW protection layer is required to reduce wear [187,188]. Consequently, the use of LST in the boundary lubrication regime creates a concern that the decrease of contact area could cause more wear and friction [50,51]. However, there are only a few studies that focus on this topic, and thus the influences of LST on the tribological performances will be verified in the present dissertation.
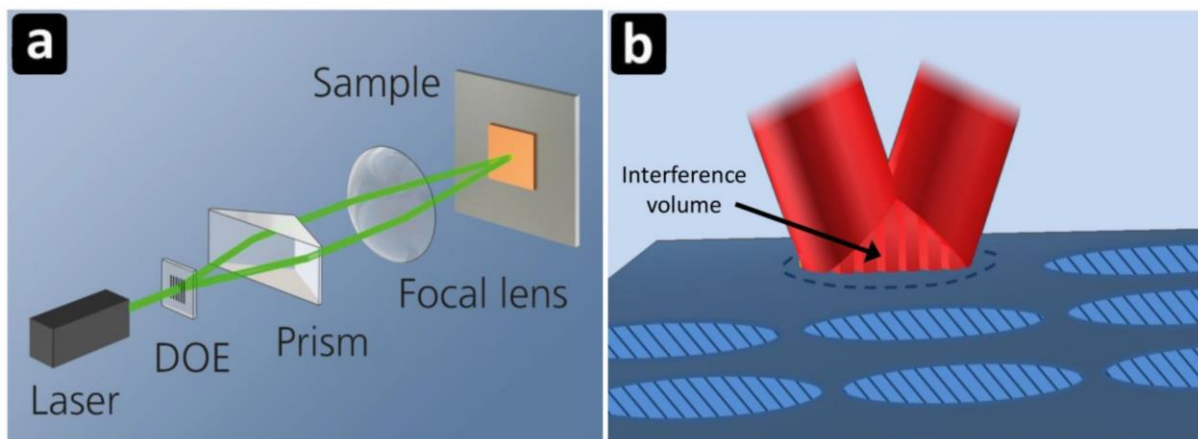

Figure 17: Schematic diagrams of (a) DLIP set-up and (b) two-beams interference [189].

LST has progressed towards using short and ultrashort pulsed lasers, which have a more comprehensive range of material flexibility. Due to different mechanisms of material removal, pulsed laser results in more precise cutting edges and smaller heat-affected zone [59]. However, the general shortcoming of laser texturing in micro-scale with complex geometry is the longer fabrication time. Therefore, Direct Laser Interference Patterning (DLIP) was developed to texture larger area in just a single laser shot, which is shown in Figure 17. DLIP ensures a time-efficient and fast surface texturing by a larger processing area [190,191]. Basically, the DLIP method is established on the principle of interference which applies two or more laser sub-beams for generating periodic patterns. The requirements of the production are that the laser wavelength should be suitable for the absorption of the selected materials, and the laser power should be sufficient for the ablation threshold [60]. When using two coherent sub-beams, DLIP creates line-like patterns, and the period of the patterns (*P*) is given by:

$$P = \frac{\lambda_L}{2 \sin \alpha} \tag{2.9}$$

where α is the incident angle and λ_L is the wavelength of the laser beam. Furthermore, more complex symmetric patterns can be produced by using additional laser beams. Different configurations of incident angle and the number of laser beams result in different geometry of patterns. Therefore, DLIP can provide a faster processing speed for micro-scale microstructure fabrication than the other surface texturing techniques (see Figure 18) [192]. Based on the development in the last two decades, DLIP can produce even nano-scale surface patterns (< 100 nm) at a fast fabrication speed (~1 m^2/min). The applications include tribology, healthcare, photovoltaics, as well as decoration, and the substrate material can be metals, polymers, and ceramics [60].
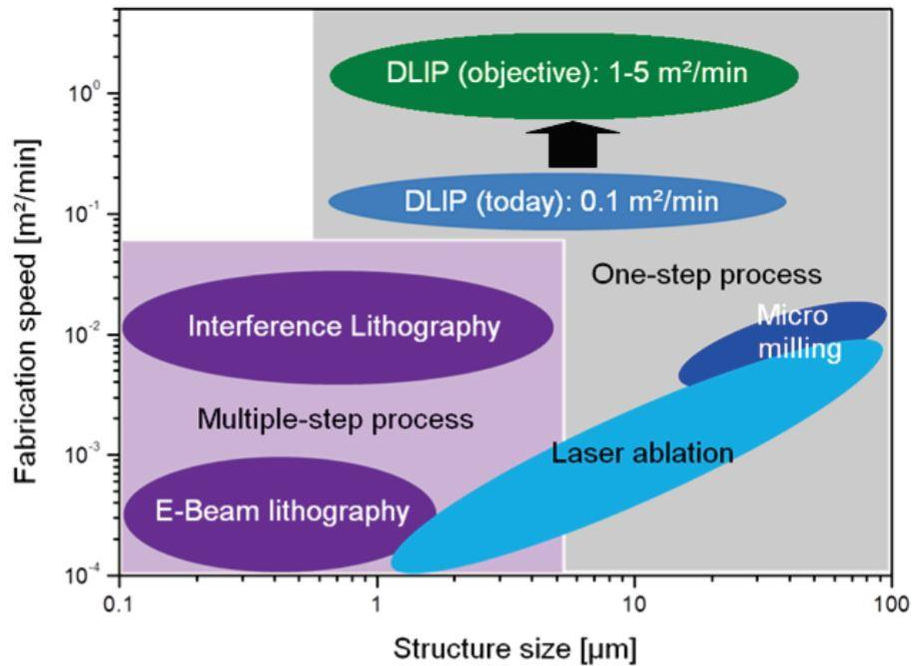
Figure 18: A comparison of different surface texturing techniques/methods by structuring size and fabrication speed. [192]

DLIP has been proven to be beneficial for versatile functions, such as friction and wear reduction [180,193,194], reduction of the electrical contact resistance [195], and modifications of wetting properties [58,196]. For the frictional modification, Rosenkranz *et al.* have presented that dot-like patterns textured by three beams interference on bearings show a wear reduction of 83% over the references [65]. The patterns were able to store wear particles into the topographic valleys and therefore reduce abrasive wear. Even though DLIP would create an additional artificial roughness on the contact surface, which might lead to increased contact pressure, the ability to store wear particles seems to be promising in wear reduction [50,65].

3. Methods

3.1. Materials

Type 81212 cylindrical roller thrust bearings were used in this study, consisting of a pair of washers and a set of cylindrical rollers in between. The bearings are made of AISI 52100 (100Cr6) with a surface roughness of R_a=0.04-0.06 μm, and the hardness is 59-64 HRC. The chemical composition of the material is shown in Table 1. In addition, the cage of PA66 was used with 15 rollers that are with both diameter and length of 11 mm. Moreover, thrust ball bearings (Type 51212) with the same material and diameter were used for fatigue life testing.

Table 1: Composition (wt.-%) of 100Cr6 (AISI 52100) bearing steel.

C	Al	Si	P	S	Cr	Mn	Cu	Mo
0.9-1.05	≤ 0.05	0.15-0.35	≤ 0.03	≤ 0.02	1.35-1.6	0.25-0.45	≤ 0.3	≤ 0.1

3.2. Surface Texturing

Two geometrically different LST patterns, dimple and cross, were tested in this study. Prior to the texturing, the samples were cleaned using a ultrasonic bath with ethanol and then isopropanol. A schematic profile of the LST patterns is shown in Figure 19.
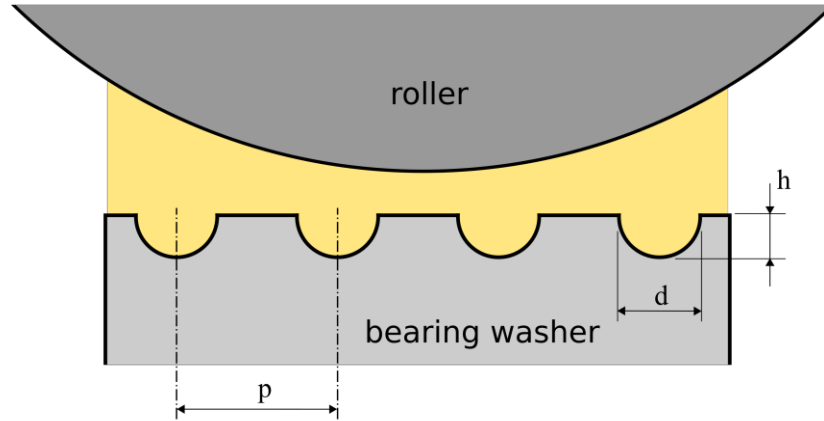
Dissertation, Chia-Jui HSU

Figure 19: Schematic diagram of LST pattern's surface profile in a lubricated condition; h shows the height from the valley to top, d shows the width of the textured area, and p shows the periodic distance [197].

The dimple patterns were created by a femtosecond pulsed laser (Spitfire Pro, Spectra Physics); the patterns' depth and diameter were ≈ 0.9 and 30 µm, respectively. A Ti-sapphire laser was applied with a wavelength of 800 nm and a pulse duration of 150 fs. The energy fluence was controlled at 12.7 J·cm^{-2}, and each dimple was manufactured by only one laser pulse. A stage system was used for the sample positioning, and thus the laser pulse can be shot onto the expected position. The periodic distance between dimples, which is called periodicity, was set as 200 and 500 µm, respectively. The experimental details of the LST patterns can be found in Table 2.

Table 2: Pattern dimension and experimental details of LST.

Samples	Pattern type	Periodicity (µm)	Height (µm)	Peak Energy (J/cm^2)	Pulse Duration
Dimple500	Dimple	500	0.9	12.7	150 fs
Dimple200	Dimple	200	0.9	12.7	150 fs
Cross9	Cross	9	1.1	1.2	10 ns
Cross30	Cross	30	1.1	1.2	10 ns

Dissertation, Chia-Jui HSU

In addition, DLIP was used for producing cross-like patterns. An Nd:YAG nanosecond pulsed laser (Quanta Ray Pro 290, Spectra Physics) was applied with 10 nm pulse duration, 532 nm wavelength, and 10 Hz pulse frequency. The laser beam that came out from the laser system was then introduced into the optic system. The primary beam was firstly split into two sub-beams through a 50/50 beam-splitter. The two sub-beams were introduced using the other mirrors to the sample with an identical incident angle and thus superposed onto the same position on the surface. The superposition caused the interference patterns, which is a line-like structure with specific periodicity depending on the incident angle. Afterward, the same treatment was processed again with a 90° of rotation to create the cross pattern. More details of the DLIP setup can be found in the previous study [190].
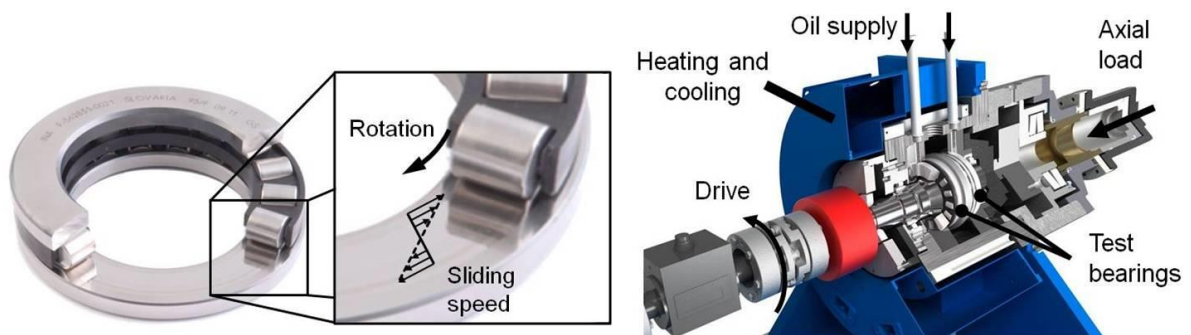
3.3. Tribometry

Figure 20: Cutaway view of the cylindrical roller thrust bearing (Type 81212) and the modified FE8 test rig for tribotesting [143].

A test rig FE8 (see Figure 20), according to DIN51819-3, was used for processing the initial selecting tests and the fatigue lifetime evaluations. A cylindrical thrust roller bearings (Type 81212), composed of two washers and a set of rollers/balls, were installed along the rotational axis. The LST patterns were manufactured onto the surfaces of the bearing washers, and the untextured surface was with a roughness value (R_a) of 0.06 μm. The lubricant was pumped into the test rig, which used base oil ISO VG 100 mixed with ZDDP as an additive of

C3C4-alkyl-chain with 0.05 wt.-%P. The initial selecting tests were operated in 2 hours with 20 rpm of rotational speed, 80kN of applied load, and 60 °C of working temperature. The lubrication condition of the tests was estimated in the boundary lubrication regime since the lambda values were calculated as between 0.04 and 0.12 [126]. The calculation was based on the oil film thickness, according to Dowson *et al.* [116,125]. More experimental details of the preliminary tests can be found in Table 3. After the test, the surface was cleaned by using benzene and isopropanol to remove contaminants, residual oil, and wear debris.

Table 3: Experimental parameters and lubricant properties at working temperature of the initial frictional tests for LST patterns selecting [197].

Experimental parameters			Oil Properties at 60 °C		
Rolling Speed	Max. Pressure	Temp.	Kinematic Viscosity	Density	Pressure-Viscosity Coeff. α
0.04 m/s	1.92 GPa	60 °C	38.3 mm^2/s	869.1 kg/m^3	1.82 x 10^{-8} Pa^{-1}

Initial tests had been processed on cylindrical roller bearings with four different LST patterns, and the best case of these patterns was selected for subsequent fatigue tests by using thrust ball bearings (Type 51212). The same testing set-up was conducted with the same concentration of ZDDP in the lubricant. The testing parameters were 750 rpm, 80 kN, and 90 °C. More information of the fatigue experiments and the used lubricant can be found in Table 4. The tests were stopped when the first surface damage occurred, which was detected by a vibration sensor. Despite the plane surface of roller bearings being more suitable for laser structuring, ball bearings were chosen to avoid wear loss by shearing. Compared to cylindrical rollers, the rolling motion of ball rollers experiences much less sliding, which minimizes abrasive and adhesive wear, and thus the fatigue life would be merely caused by pitting failure.

Table 4: Experimental parameters and lubricant properties at the working temperature of the fatigue tests [197].

Experimental parameters			Oil Properties at 90 °C		
Rolling Speed	Max. Pressure	Temp.	Kinematic Viscosity	Density	Pressure-Viscosity Coeff. α
1.53 m/s	3.5 GPa	90 °C	13.6 mm^2/s	850.8 kg/m^3	1.50 x 10^{-8} Pa^{-1}

3.4. Characterization

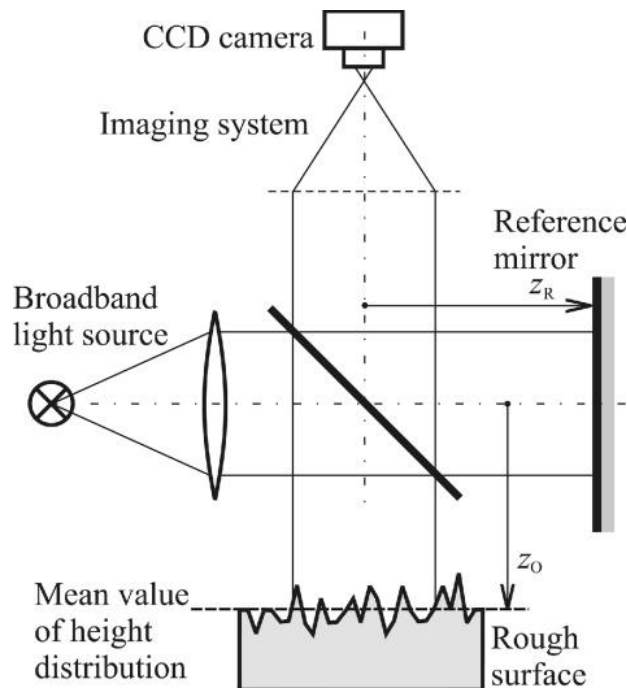## 3.4.1. White Light Interferometry

Figure 21: Schematic of white light interferometry [198].

White light interferometry (WLI), a type of optical profilometry, is a non-contact measurement method. It is generally used for topographical observation due to the quick measurement without leaving damage or contaminant. The principle of interferometry is based on the wave superposition, which combines two waves, the incident and the reflected light, and identifies the difference of the interference patterns, which is caused by the phase difference between the two waves. When the waves are in phase, constructive interference occurs; when waves are out of phase, destructive interference appears. By means of the low coherent property of a white light source, diffraction patterns with less noise, compared to monochromatic light,

Dissertation, Chia-Jui HSU

can be obtained. At the output of the interferometer, usually a CCD camera is used, and the light intensity for each pixel on the camera gives the information about the geometric form of the measured surface/object. A sketch view of a WLI is shown in Figure 21.

A WLI (New View 7300, Zygo) and an optic microscope (VHX-2000, Keyence or BX 60, Olympus) were used for surface observation in this study, which provides information on morphology and geometry profile of the textured and reference surface. The measurement achieves micro-resolution in the lateral direction and nano-resolution in the vertical direction.

3.4.2. Raman Spectroscopy

Raman Spectroscopy is a spectroscopic technique used to determine the vibrational modes of molecules, which has been usually applied in chemistry. The vibration modes of molecules are the features for identification, whereas rotational and other low-frequency modes may also be acquired. By detecting the inelastic scattering of photons, the energy shift provides information about the vibration modes, which is known as Raman scattering.
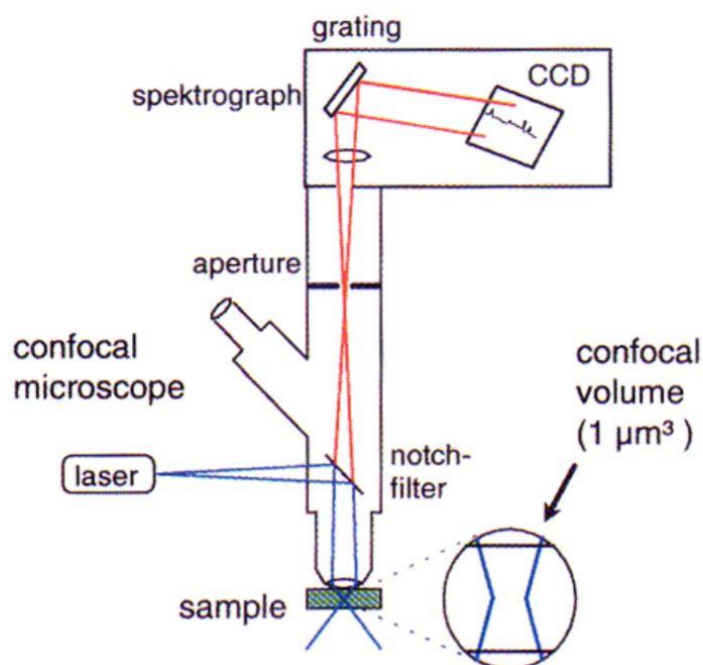

Figure 22: Schematic diagram of a confocal Raman spectroscopy microscope [199].

Chemical examination of the ZDDP tribofilm here was performed by Raman spectroscopy. The grating was selected as 2400 lines mm^{-1} to have a spectral resolution up to 1.2 cm^{-1}. A 532 nm laser was used as a excitation light source with a yielded power of 5 mW. The detected area was examined after each acquisition by optic microscopy to ensure no thermal damage was caused by the laser exposure. Furthermore, the spot size of the laser was nearly 4 μm^2 using a 50x objective lens.

3.4.3. Atom Probe Tomography
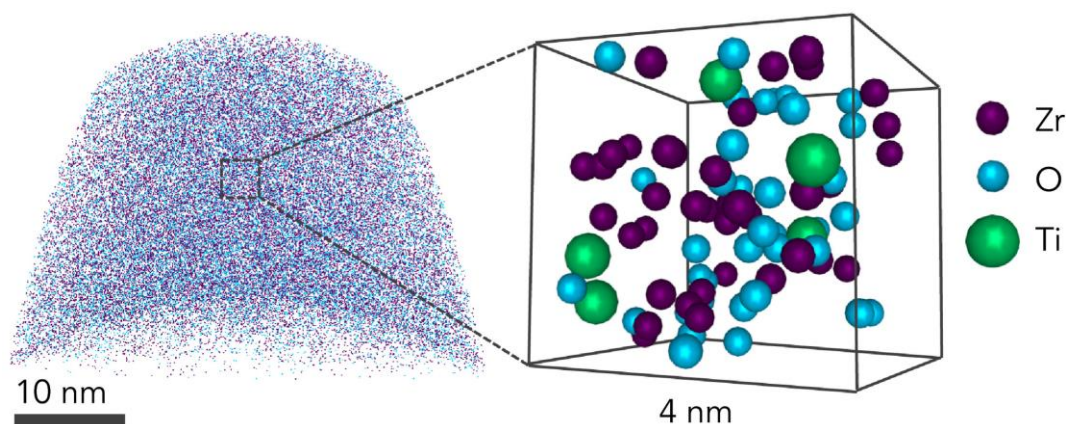
Figure 23: A typical 3D reconstruction by using atom probe tomography (APT) [200].

Atom probe tomography (APT) is an analytical technique for high-resolution chemical and structural investigation, which has the ability to demonstrate the material in three-dimensional (3D) compositional analysis with atomic resolution [201,202]. APT offers great potential to characterize the elemental distribution of the tribofilm in further detail. However, only few studies the AW tribofilm by using APT. For example, Kim *et al.* [203] identified the little content of boron in a tribofilm by APT, which used boron as an additive. Guo *et al.* [148] established a model of tribofilm that shows an iron oxide interlayer with only 10 nm in thickness. Therefore, APT was adopted in this study to reveal and clarify the interface in between the ZDDP tribofilm and the steel substrate.

Atoms or compounds are evaporated from the probe base on field evaporation and induced

by laser pulsing, whereas the sample is prepared in the form of a very sharp tip. The flying time of an individual atom started from laser pulse till the arrival on the detector is obtained and called time-of-flight (TOF), which performs the chemical qualitative. In addition, the position sensitive detector (PSD) captures the ion impact that came from the tip, determining the (X, Y) positional data. By integrating the information collected from the tip, a 3D image of the tip at an atomic scale can be reconstructed.
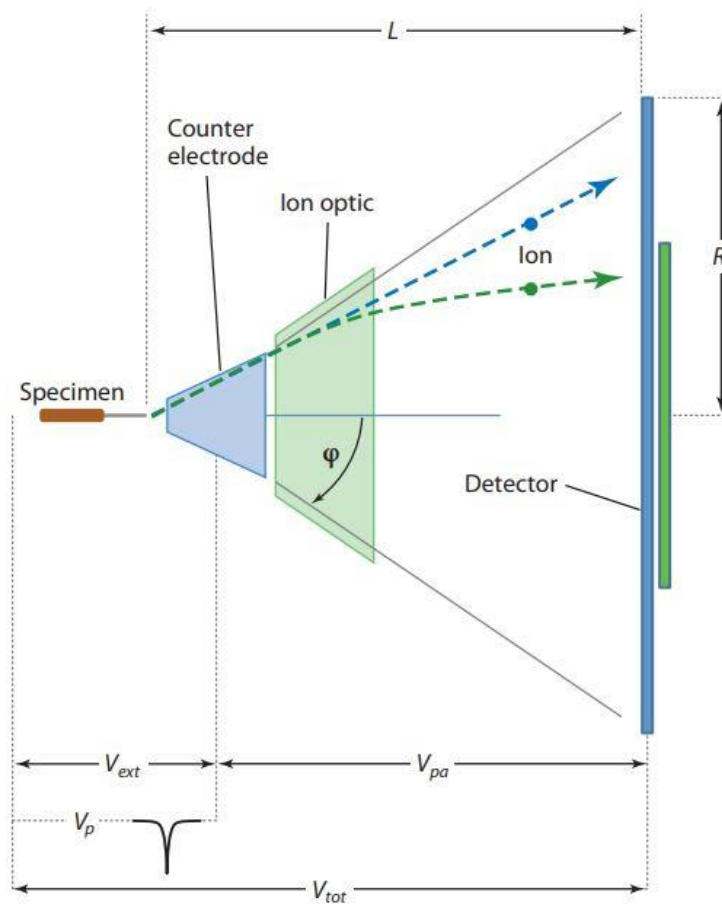
Figure 24: Schematic diagram of an atom probe tomography. V_{tot}: total accelerating voltage; V_p: voltage pulse, V_{ext}: extraction voltage, V_{pa}: postacceleration voltage, R: the radius of the detector; L: the flight path length [204].

In order to perform the APT analysis, precise sample preparation is required, by which samples were shaped to be tips with around 25 nm of diameter. Firstly, above the ZDDP tribofilm, a 200 nm Cr capping layer was deposited by physical vapor deposition (PVD). Then the preparation was processed in a dual-beam scanning electron microscope / focused ion beam workstation (SEM/FIB, Helios Nanolab 600, FEI). The specimens were made by using FIB according to the lift-out technique described in [205]. Finally, the ultimate shape of specimens was completed by low energy milling at 2 kV, which minimizes the Ga-induced damage. The measurements were performed in LEAP™ 3000X HR (CAMECA) laser pulsed APT system with a repetition rate of 100 kHz and a laser pulse energy of 0.7 nJ. The evaporation rate was set to 2 atoms per 1000 pulses. In addition, the specimen temperature was set at about 60 K and the chamber's pressure was lower than 1×10^{-10} Torr (1.33×10^{-8} Pa). Moreover, the obtained datasets were analyzed and reconstructed by IVAS™ 3.6.14 (CAMECA).

3.4.4. Transmission Electron Microscopy

TEM is an electron microscopy used to reveal sub-micrometer to nanometer-scale microstructures. The specimen for measuring has to be shaped as an ultra-thin section less than 100 nm. An electron beam is used, and this focused beam then passes through the specimen. The observed intensity of the transmitted electron performs an image of the specimen [206]. Due to the ability of high-resolution observation, TEM has been widely used in the biology and material science field.

A TEM (Jeol Jem 2010) was used to characterize the microstructure and crystal structure of the antiwear tribofilm. A 200 kV electron beam was applied by LaB6 source. Furthermore, an equipped EDS detector and a selected area electron diffraction (SAED) were used to detect the elemental composition and the microstructural properties.
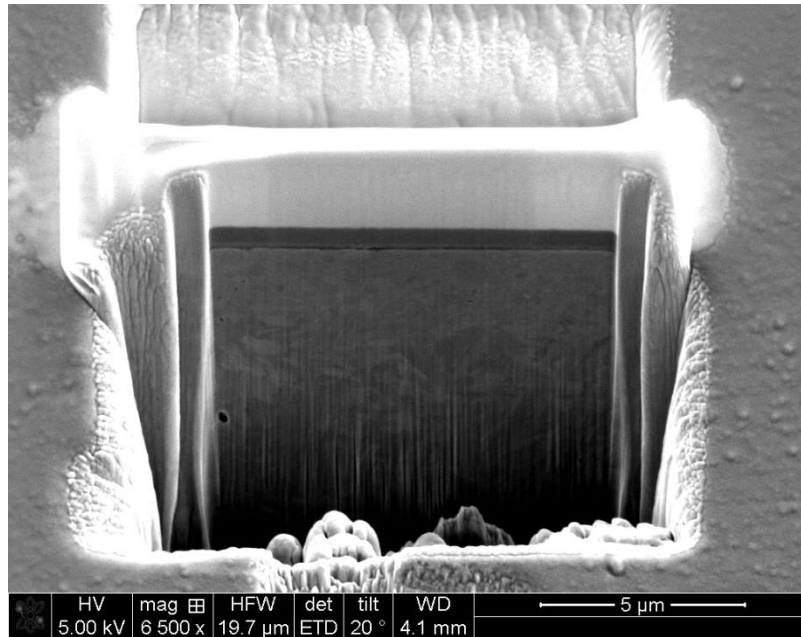
Figure 25: A cross-section observation of a steel specimen in a lamella preparation by SEM/FIB with the stage tilted 20°.

3.4.5. Scanning Electron Microscopy

Scanning electron microscopy (SEM) is a high-resolution technique for surface topography, composition, and surficial distribution. The basic principle is similar to TEM, both using an accelerated electron beam. The beam scans the specimen surface, and the detector observes synchronously the signal scattered from the focus spot. The lateral resolution depends on the size of the electron spot, which can reach a few nanometers. Compared to TEM, SEM performs less resolution due to the different detecting principle between electron transmission and scattering [207].

A scanning electron microscope equipped with a focus ion beam (SEM/FIB), FEI Helios NanoLab600, was used in the present study. The surface morphology can be demonstrated by secondary electron image (SEI), and the chemical composition by the equipped EDS. The in-situ lift-out technique was applied to prepare samples for TEM and APT analyses by using FIB. [208] In addition, SEM/FIB can also provide a quick cross-section observation of the thin film and the sub-surface as shown in Figure 25.

3.5. Contact Simulation

The contacts between the rollers and the textured washers of thrust rolling bearings were modeled by the boundary element method (BEM) to estimate the contact pressures and contact areas for each LST pattern. BEM is a numerical method that approximates governing differential equations into integral equations, which has been used for solving contact mechanics problems since 1981 [209]. When modelling two contacting bodies as shown in Figure 26, BEM divides the contacting surface into small nodes instead of the whole body and performs the calculation of strain and stress on each paired node by using the given boundary conditions. According to the literature [210,211], BEM estimates the calculation of stress more accurately and efficiently than other numerical methods, including the finite element method (FEM).
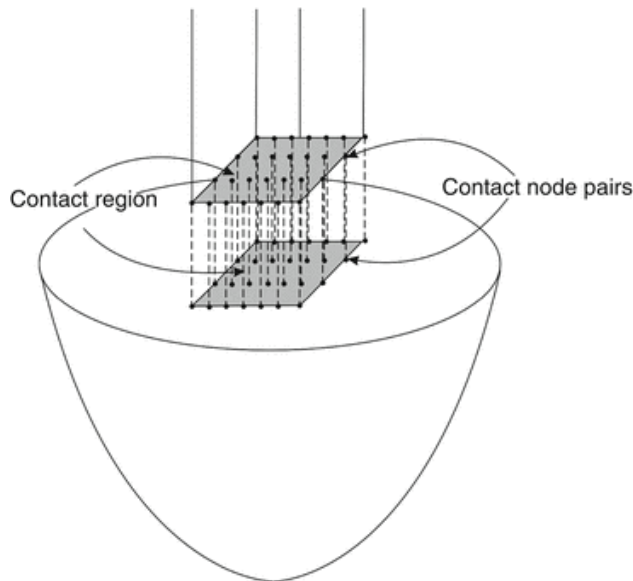
Figure 26 Schematic for contact analysis of two contacting bodies by boundary
element method [212].

In this study, the 3D surface profile of the textured and reference samples was used for BEM modeling, and a smooth cylindrical roller was set as the counter body. Homogeneous half-space was assumed, and an iterative conjugate-gradient method was used to approach a

Dissertation, Chia-Jui HSU

valid contact pressure [213]. 3D surface profiles measured using WLI for analysis were in size 640×480 nodes as 350 x 263 μm, and the measured area was smaller than the full roller-washer contact. Therefore, the modeling surface was expanded by mirroring and tiling the measured surface profile data. This provides sufficient contact area and thus avoids the edge effects. Finally, contact pressures and contact area were subsequently obtained over the as-textured LST pattens. It is noted that only elastic analysis was made in this contact simulation. Although without consideration of plasticity and hardness of the material, the simulation does enable an appropriate comparison of the extent of loading stresses.

4.   Summary of Results

A summary of the results is presented in this chapter. Four peer-reviewed journal papers listed at the end of this dissertation have studied the frictional performances and chemical composition of the ZDDP protective tribofilm formed on the laser-textured and standard surfaces of the thrust rolling bearings. Four types of LST patterns had been examined separately, and the best one was tested for the fatigue lifetime. The test rig FE8 was used for all the tests, operating with ZDDP-mixed lubricants under boundary lubrication (see Figure 20). There are two main targets in this dissertation: the first part is to dedicatedly characterize the ZDDP tribofilm by high-resolution examinations (**Paper I & II**); and the second part is to demonstrate the laser textured surface's frictional performances and the enhanced growth of the ZDDP tribofilm (**Paper III & IV**). The specific contributions to the field are described below:
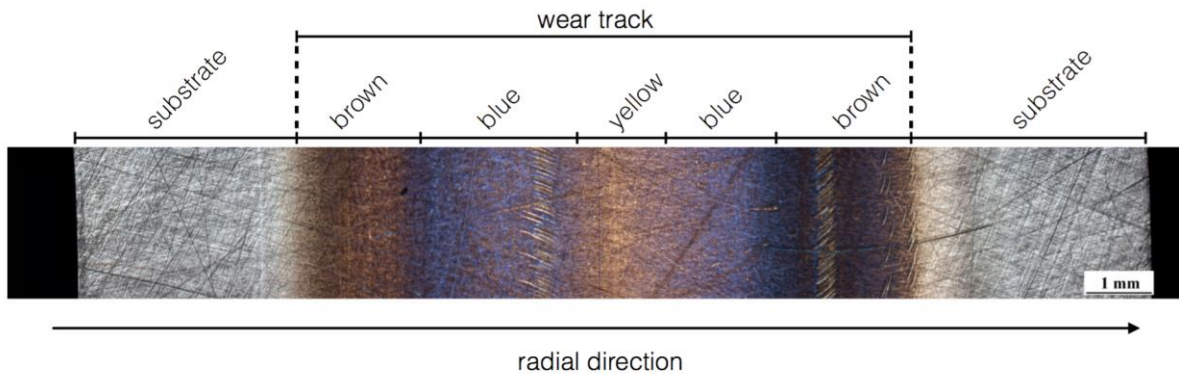

Figure 27: Optical image showing the overview of the wear track on the bearing washer after 2 hours of FE8 tribotest by 80 kN of applied load, 20 rpm of rotational speed, and 60°C of working temperature.

Firstly, the characterization of the antiwear tribofilm formed on the surface of roller bearings under boundary lubrication is presented in **Paper I**. A 0.02 wt.-% of ZDDP was added into the base oil PAO8 as AW agents, which is a relatively low amount compared to the

commercial use (0.05-0.1 wt.-%). The FE8 test rig was operated under contact stress of 1.92 GPa with a rotational speed from 10 to 20 rpm. After 2 hours of testing, the AW tribofilm was observed formed on the surface and functions as a barrier to prevent direct contact between washers and rollers, which decreases wear. An overview of the wear tracks was recorded by optical light microscopy as shown in Figure 27, and the differently colored regions from left to right along the radial direction can be clearly identified for all the tested bearings. However, the role of the typically observed color difference is still not fully understood from lots of chemical investigations over the years [22]. To distinguish the difference among them can reveal the distribution of tribofilm, and thus enable a precise positioning when characterizing. Accordingly, the question regarding the appearance of tribofilms as blue- and brown-colored layers was addressed in this paper.

The tribofilms were preliminary compared by the layer thickness obtained by the cross-sections of SEM/FIB. The thickness values at the different color regions were similar, both around 70 nm, indicating the thickness factor is not making the variation of color. However, an EDS line scanned through the color transition region (see Figure 28) and the blue regions show stronger peaks related to the ZDDP elements (P, S, Zn). It provides a clear comparison that the chemical composition differed between different color appearances. Further chemical examinations of the tribolayer was made by using Raman spectroscopy. The spectra (see Figure 29) in wavelength shift between 200 to 1500 cm^{-1} were taken at the yellow-, brown-, and blue-colored zones. Comparing to the reference surface, both the blue and brown regions display resonances of phosphate and zinc sulfite at around 1000 and 350 cm^{-1}, respectively. Furthermore, the difference in the ratio of the intensities between 351 and 386 cm^{-1} revealed that the blue region has higher content of $(Zn_{0.88}Fe_{0.12})S_{1.00}$. In addition, the spectrum of the yellow region shows Fe_3O_4 at 660 cm^{-1}. The findings clarify the ambiguous description of the tribofilm appearance in the literature [150,187,214], and the color difference of the tribofilm should be attributed to the chemical constitution instead of the layer thickness.
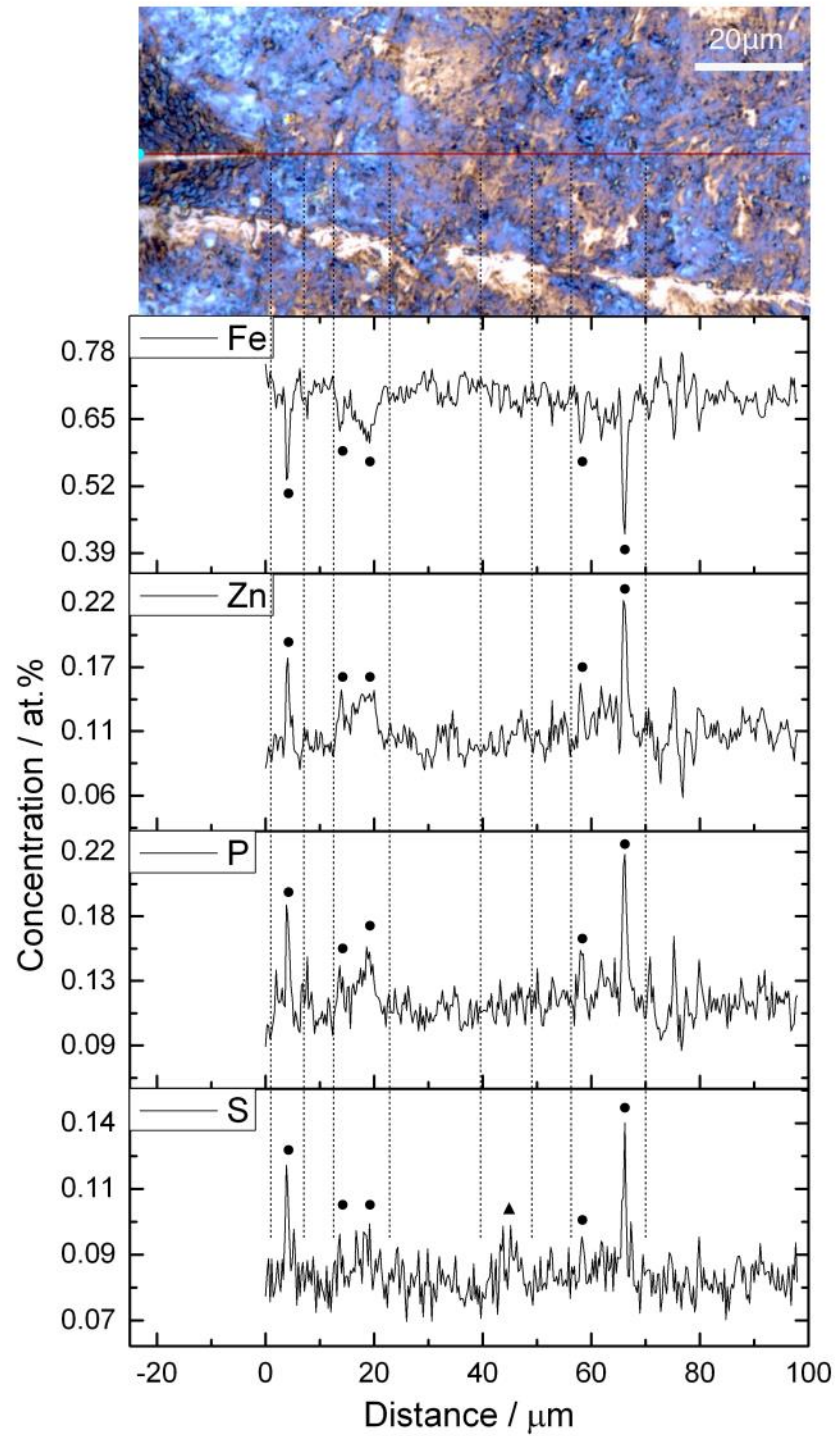
Figure 28: EDS line-scan of the ZDDP tribofilm through blue (dots) and brown (triangle) regions on the bearing washer tribotested by FE8 test rig for 2 hours [143].
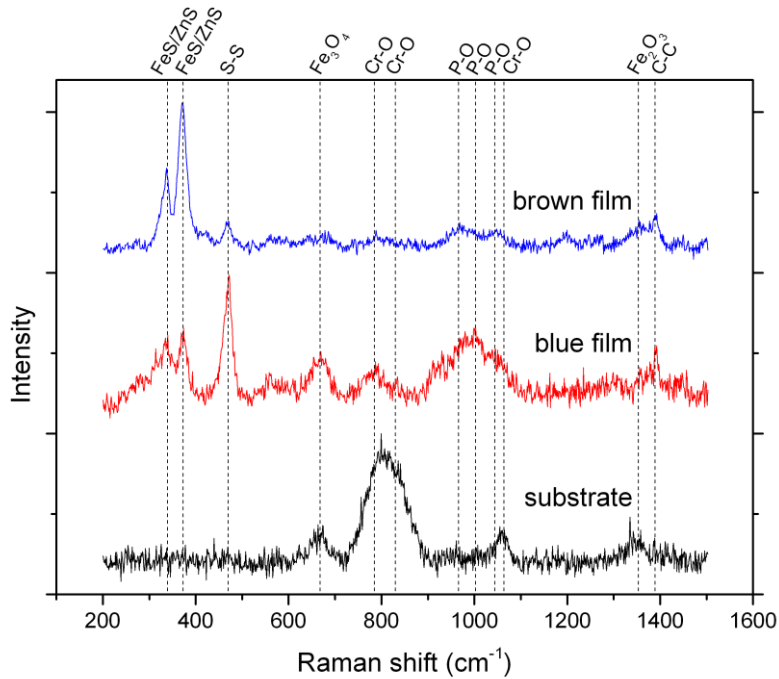
Figure 29: Raman spectra of the antiwear tribofilm at the region of brown/blue on the roller bearing after 2 hours tribotest in the range from 200 to 1500 cm^{-1}.

The blue-colored region can be considered for further microstructural and chemical characterizations according to the findings from the results of Raman and EDS analyses. In Figure 30, the microstructure of the ZDDP antiwear tribofilm was obtained by TEM. The cross-section image shows from the top-right to the bottom-left four regions: Ion-deposited Pt capping layer, electron-deposited Pt protective layer, the ZDDP tribofilm, and the steel substrate. The bright layer in the middle, namely the tribofilm, has a thickness between 70 and 140 nm; the deformed tribomutation region is below and between 250 and 450 nm. The thickness of the tribomutation region is in good agreement to the literature [215]. SAED was performed on the tribofilm and the substrate in Figure 30(b) and (c), respectively. The diffraction pattern shows an amorphous structure of the tribofilm with some unpreventable feature from the substrate due to the aperture size of 180 nm. Moreover, the substrate displays the main six reflections corresponding to ferrite. However, no crystalline structure regarding sulfide and oxide was able to be identified, and thus more dedicated chemical analyses have been done and shown in the following paper.
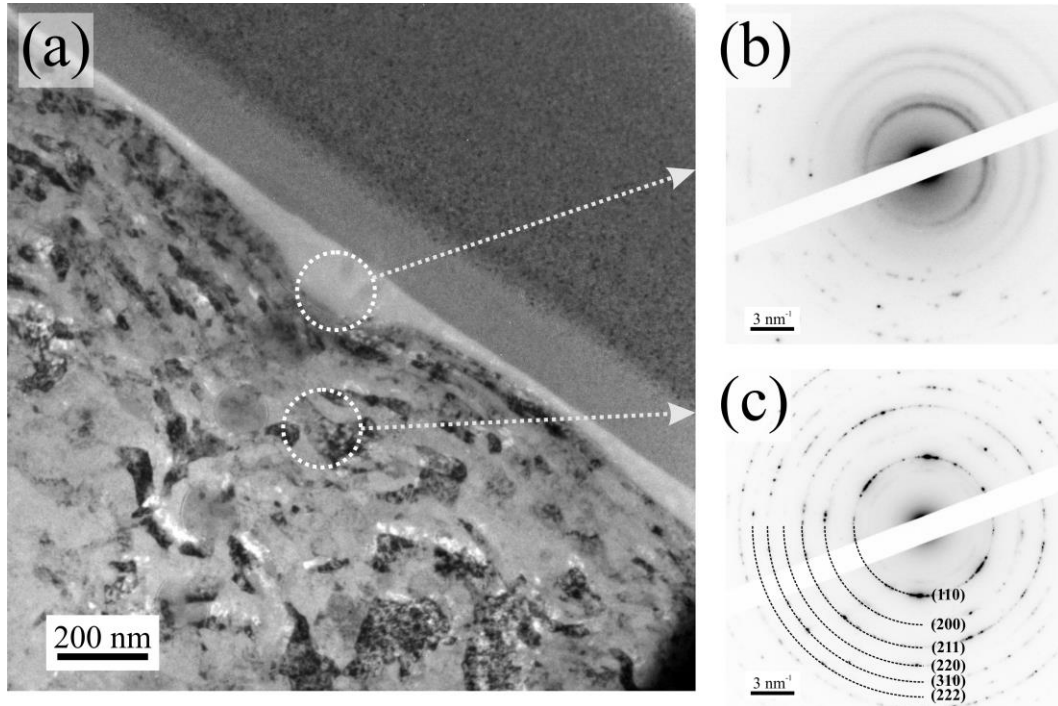
Figure 30: (a) TEM image of the cross-section of the ZDDP tribofilm in the wear track; Selected area electron diffraction pattern of the tribofilm (b) and the substrate (c). [143]

As a conclusion of **Paper I**, the antiwear tribofilm formation on the surface of the cylindrical thrust roller bearings has been tested by the FE8 test rig, and microstructural performance and chemical constitution of the tribofilm were characterized. Furthermore, Raman spectroscopy proved that more ZnS and FeS were found in the blue layers, whereas Fe_3O_4 was found dominant in the brown layers. The remaining question regarding the oxide and sulfide layers at the interface was answered then in the follow-up **Paper II**.
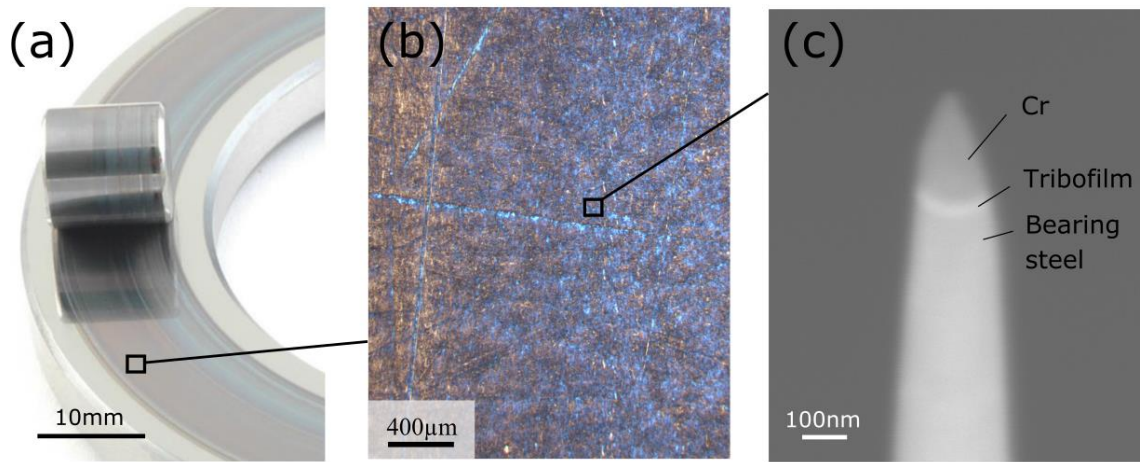
Figure 31: (a) Image presenting the wear track on the surface of thrust ring with a cylindrical roller; (b) the ZDDP tribofilm in the wear track obtained by optic microscopy; (c) the shaped tip specimen of the tribofilm for APT analysis. [216]

The examinations on the ZDDP tribofilm were processed into a nano-scale perspective in **Paper II** where both XPS and APT were used for revealing the nature of the interface. This paper demonstrates the chemical details of the tribofilm and particularly discovered the interface between the tribofilm and the substrate. The depth profile measured by XPS showed that the thickness of the tribofilm was around 40 nm. The content of Zn was found higher in the upper part; in contrast, more Fe could be identified closer to the bottom of the tribofilm. Moreover, APT atom maps demonstrate the spatial distribution of the elements in the specimen, which was prepared in a dual-beam SEM/FIB as shown in Figure 31. APT observed the tribofilm with a spatial resolution of approximately 0.1 nm, which built a delicate 3D-reconstruction of the tribofilm (see Figure 32). From top to bottom, the 3D-reconstruction includes Cr capping layer, ZDDP tribofilm, and steel substrate. Those ZDDP related elements such as Zn and P can be found in the region of the bulk tribofilm, whereas the Fe was located mainly beneath it. FeO can be found in both the tribofilm and the substrate. Particularly, a 5 nm thin oxide interlayer under the bulk tribofilm was identified, and cluster-like sulfur enrichment was found within the interlayer.
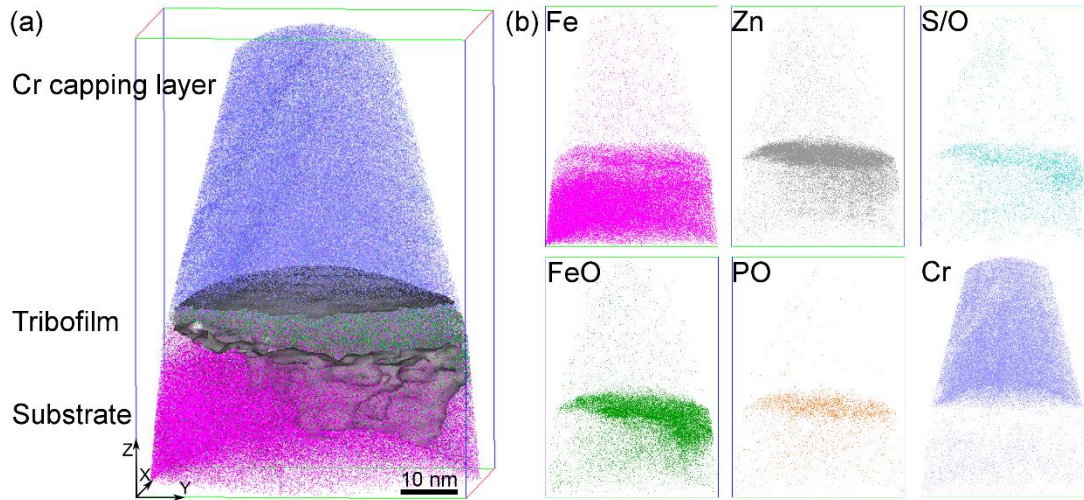
Figure 32: (a) APT 3D-reconstruction of the tribofilm showing from top to bottom Cr capping layer, ZDDP tribofilm and steel substrate. (b) Individual spatial distribution of Fe, Zn, S/O, FeO, PO and Cr [216].

The observation of the oxygen at the interface between the bulk tribofilm and the substrate can be supported by the literature [30,151,156], which has suggested that the shear force of sliding was causing oxidation to both tribofilm and contact surfaces. Hence, wear particles, namely iron oxide, would be captured by tribofilm due to the "digestion" mechanism [30,32,151]. However, it is still not yet a consensus that the sulfur enrichment was found at the interface. Although some aforementioned studies claim no sulfur enrichment, a thin sulfur layer should be able to be observed according to the HSAB principle [151]. Correspondingly, the high-resolution evidence presented in **Paper II** supports the prediction. It is a clear acquisition that builds a 3D reconstruction and clarifies the question of sulfur enrichment.

APT does reveal the tribofilm at the nanometer scale that displays further details of the chemical composition, which would be challenging for the other analytical techniques to obtain. However, the sample preparation is complex and requires high-level cleanliness. Accordingly, the XPS depth profile provides, in this study, a general impression of the chemistry concerning the average depth distribution of the related components. Combining these observations, a highly probable matching position of the inhomogeneous tribofilm for APT analysis could be

selected. Consequently, adequate preliminary examinations are recommended to be made before an investigation of APT analysis, especially for locally varied specimens.
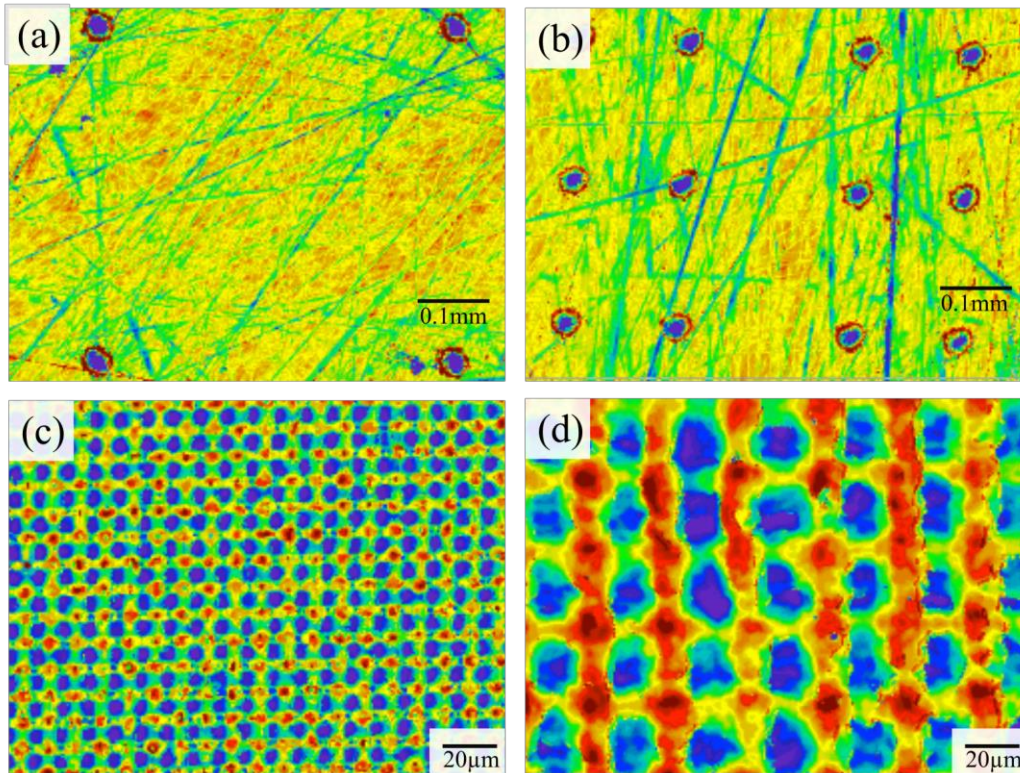

Figure 33: Topographical profiles of the LST patterns on the surface of bearing washers. The dimples were produced by femtosecond laser with a periodicity of (a) 500 μm and (b) 200 μm; The cross patterns were created by DLIP with a periodicity of (c) 9 μm and (d) 30 μm [197].

The second part of this study aims to improve the lifetime of rolling bearings by a combined approach using LST and ZDDP. Moreover, the question about the reliability of using LST for machine components operating under boundary lubrication will be answered in **Paper III** and **IV**. To examine how LST can improve the frictional performances, the concentration of the additive was changed from 0.05 to 0.02 wt.-%P compared to the previous tests. Since the aim of this study is to decrease the usage of ZDDP, the additive concentration was selected to

be decreased. According to a related work by Stratmann *et al.* [217], the phosphor concentration of 0.02 wt.-% is not sufficient to generate ZDDP tribofilm for surface protection. However, in **Paper III**, a fully formed ZDDP tribofilm was identified on the LST patterns, indicating the introduction of periodic micro-patterns enhanced the growth of the antiwear layer. The benefits of the LST treatments have been proved in these studies, and the scientific details are described as follows.

Table 5 Surface roughness and parameters of the bearing ratio curve of the LST patterns as textured [197]*.

	S_q	S_a	S_{pk}	S_k	S_{vk}	A_p	A_v
Reference	0.08	0.06	0.12	0.18	0.11	0.003	0.006
Dimple200	0.25	0.15	0.46	0.24	0.45	0.015	0.013
Dimple500	0.16	0.09	0.33	0.13	0.30	0.008	0.009
Cross9	0.39	0.32	0.28	1.04	0.20	0.008	0.008
Cross30	0.33	0.27	0.27	0.68	0.18	0.007	0.007

*All values are shown in μm.

The study was designed to examine four styles of LST patterns, cross- and dimple-like, respectively, with two different structural periodicities (in Figure 33) produced on the surfaces of roller bearings. The roughness details shown in Table 5 were obtained from WLI measurements. The increase of R_a and R_q indicates that the surface roughness was increased in all LST patterns, and a greater roughness can be found with shorter periodic distance. Moreover, the dimple patterns show the surface roughness similar to the reference, whereas the cross patterns modified the surface more significantly.

In order to assess the capacity of lubricant storage, the values from the bearing ratio curve (see Chapter 2.1.2.) were obtained. It has been suggested that the S_{vk} value extracted from a bearing ratio curve is a suitable index of the ability for lubricant storage [105]. When taking only S_{vk} values for comparison, the dimple patterns can store more lubricant than the cross patterns. However, considering the overall topography differs between the two pattern types, the assessment of storage capability should involve both S_k and S_{vk}. Therefore, the possible storage space within the main body of the profile, represented as core height S_k, was also

included. As a result, cross patterns can provide larger space that acts as reservoir. In addition, the values of peak and valley area (A_v and A_p) present a similar trend to the S_{pk} and S_{vk} values.
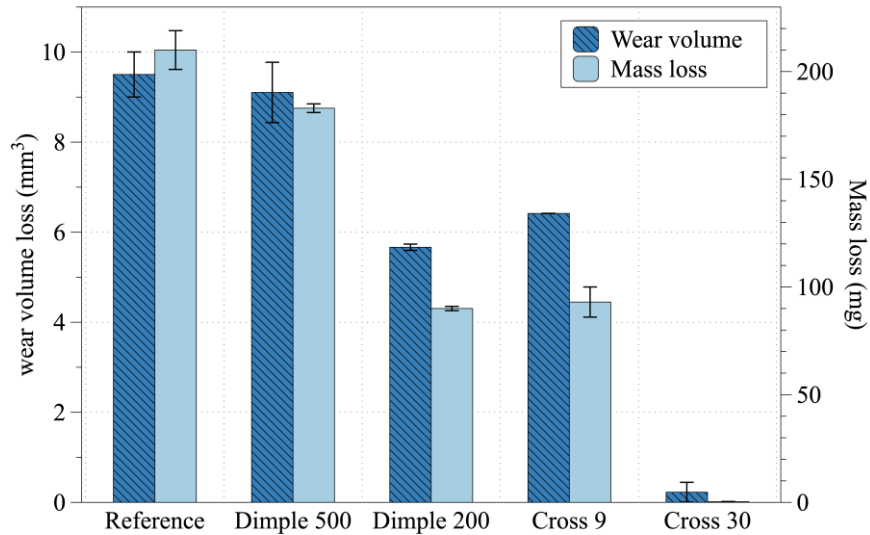

Figure 34: Wear and mass loss of the laser textured roller bearings tested by FE8 test rig with 80 kN load, 20 rpm, and 60°C for 2 hours [197].

After 2 hours of testing, LST patterns performed a distinct reduction of wear, measured and shown in Figure 34. Compared to the untextured bearings, all the laser patterns were found with less wear loss. The results conform to the assessment of lubricant storage capacity that prevents insufficient lubrication. Moreover, Cross30 performs a wear reduction of 99% compared to the reference samples, indicating a significant ability for surface protection. The reasons for this have been investigated in **Paper III**.

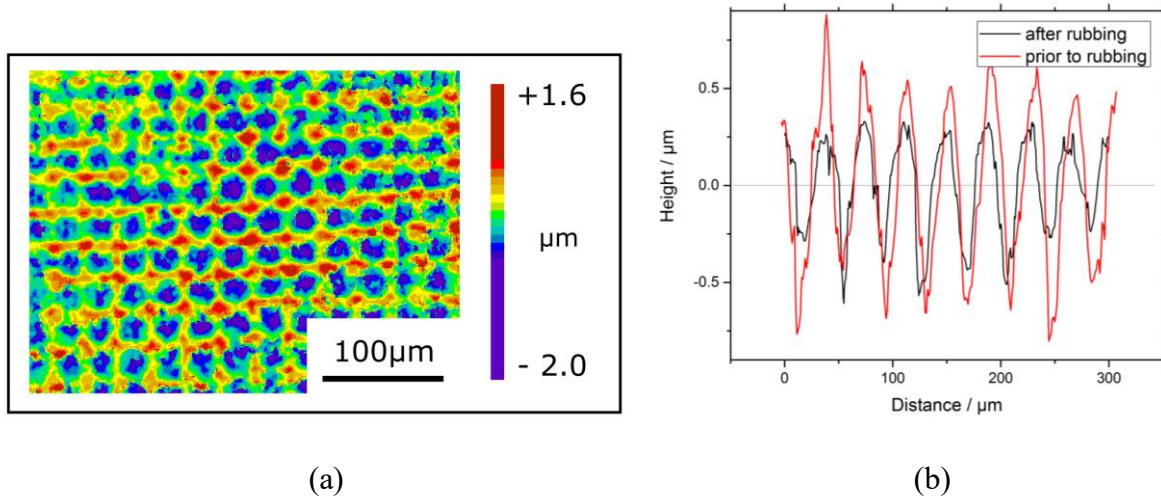<div align="center">(a)   (b)</div>

Figure 35: Surface morphology after tribotesting (a) and a comparison of the cross-section profiles prior/after tribotesting (b) of the Cross30 measured by WLI [218].

In **Paper III**, the wear behavior and the surface analyses of the Cross30 were studied by profilometry and Raman spectroscopy. After 2 hours of rubbing, the cross patterns still remained on the surface of the bearings (Figure 35(a)). Compared to the patterns before tribotesting, the worn-off depth is approximately 40 %, which can be seen in Figure 35(b). Moreover, the average coefficient of friction (COF) of the reference sample is 0.14, whereas the value for Cross30 is about 0.1, which represents a 30% reduction. As mentioned, the wear damage of Cross30 can be barely seen, performing a reduction of wear loss by two orders of magnitude. This implies that the use of LST protects the surface from severe wear that was due to the direct contact of the contacting surfaces. Cross30 was able to prevent insufficient lubrication and could trap those debris particles in the valleys. Moreover, the formation of the ZDDP antiwear tribofilm avoids direct contact of metal-to-metal, thus decreasing the damage from wear significantly.
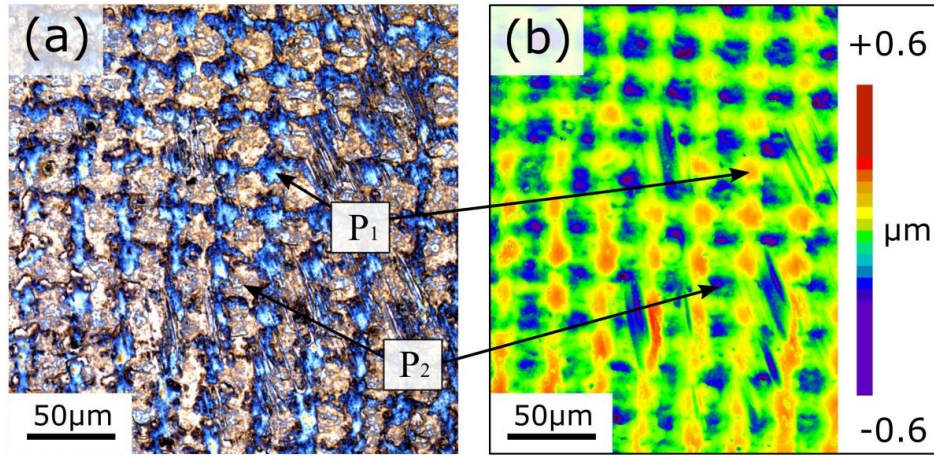
Figure 36: Surface topography of Cross30 after tribological test observed by (a) optical microscopy and (b) laser scanning microscopy. P_1 points to a blue-colored region at the top of the patterns, whereas P_2 presents a region without blue color in the valleys [218].
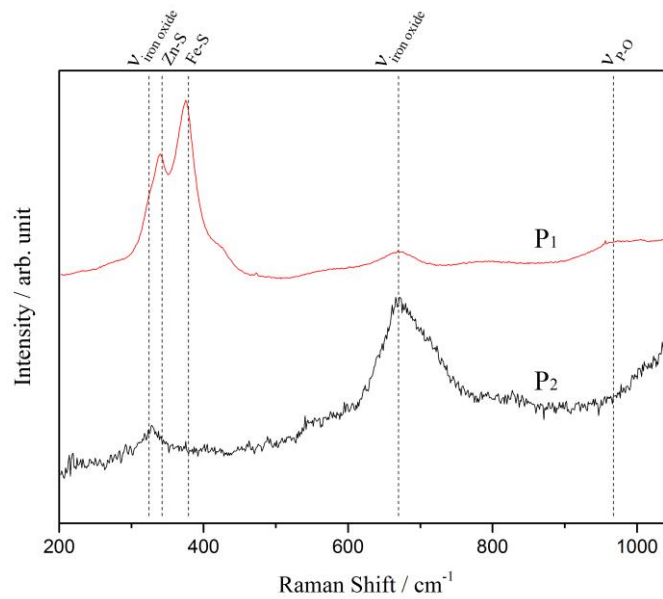

Figure 37: Raman spectra of the tribofilm on Cross30: P_1 examines a blue-colored region on the topographical maximum of the patterns, and P_2 is in valley area of the patterns without blue color [218].

In Figure 36, the same area on the bearing surface after rubbing was imaged by both optical microscopy and profilometry. By comparing both figures (a) and (b), the correlation between color appearance and surface topography can be demonstrated. The blue regions, marked as P_1, connect each other as a net were found on the top of the cross patterns; whereas the spots with light-brown color were found in the valleys, which are marked as P_2. The comparison indicates that a tribofilm could form at the regions of topographical maximum. Therefore, those two points (P_1 and P_2) were examined by Raman spectroscopy to analyze the surface chemistry. In Figure 37, Raman spectroscopy was used to determine the tribofilm at the corresponding regions. The spectrum of P_1 shows peaks related to Zn-S, Fe-S, and P-O at 351, 386, and 965 cm^{-1} [219–221], respectively; the spectrum of P_2 reveals peaks related to iron oxides at 320 and 670 cm^{-1} [222]. This confirms that the ZDDP tribofilm was formed on top of the pattern, and the formation was induced by the contact pressure. Contacts occur at the topographical maxima, whereas the area of valleys retains lubricants and supply oil when encountering insufficient. According to the literature [136,137], the pressure-induced ZDDP tribofilm grows faster than the thermally induced one and exhibits better tribological performance. In **Paper III**, it is proven that the ZDDP tribofilm appears only on top of the LST patterns, which reduces the wear loss significantly.

To better understand the reason why particular LST patterns enhance the tribofilm formation, a contact simulation based on the BEM model was made in **Paper IV** to analyze the pressure distribution. It is suggested by Gosvami et al. [140], according to in-situ experiments of AFM, that the growth rate of tribofilm formation increases five times when contact pressure increases from 3 to 5 GPa; the growth rate becomes saturated when the stress rises above 6.5 GPa. Consequently, the contact simulation in this study also targets the same pressure range. Each node of the surfaces from the simulation results has been classified based on the pressure value. When the pressure is between 3 and 7 GPa, the contacting area would be expected to be overload for the formation.
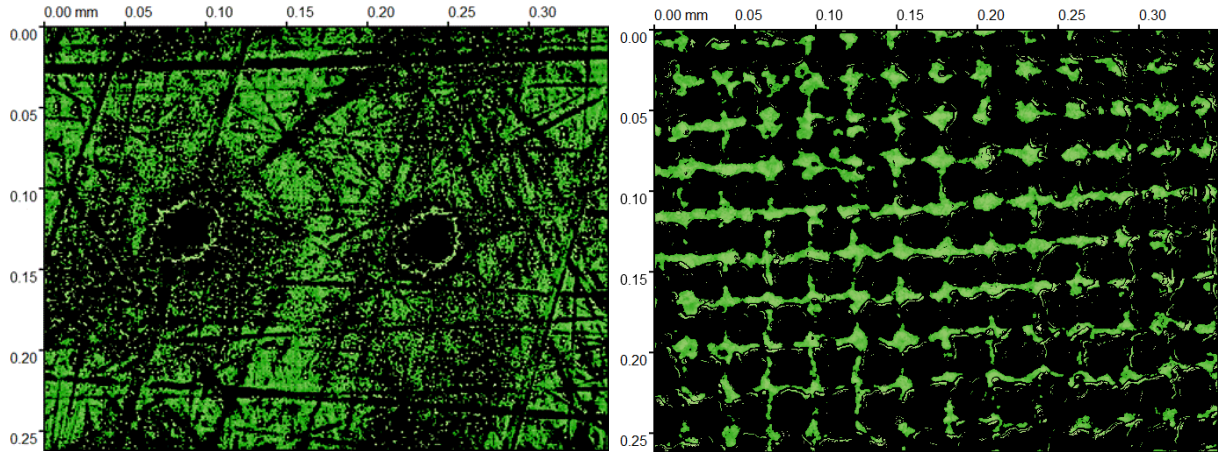
Figure 38: Contact area of the LST patterns from the results of contact simulations of (a) Dimple200 and (b) the Cross30. The contact area is present in green. [197].

The contact area of the LST patterns by the BEM simulation is shown in Figure 38, and the overall area coverage of contact is shown in Figure 39(a). Moreover, the pressure value on each node in the surface was calculated, and the numbers of the nodes that experienced certain ranges of pressure have been summarized in Figure 39(b) as histogram charts. Based on the simulation results, the dimple patterns perform a similar pressure distribution compared to the reference, but higher stress can be found surrounding the dimples. This is attributed to the spikes observed around the dimples, which were caused by the texturing. Moreover, the total contact area decreases 20% when the periodicity decreases from 500 to 200 μm. The increase of pressure on the dimple patterns leads to the right-shift of the histogram chart in Figure 39(b). On the other hand, the cross patterns present more amount of higher-pressure regions due to the overall smaller contact area, by which the shape of the histogram chart was again biased to the right. It is obvious that the cross patterns changed the pressure distribution more than the dimples with respect to the untextured reference since the geometry of LST patterns affected the surface roughness more dominantly.
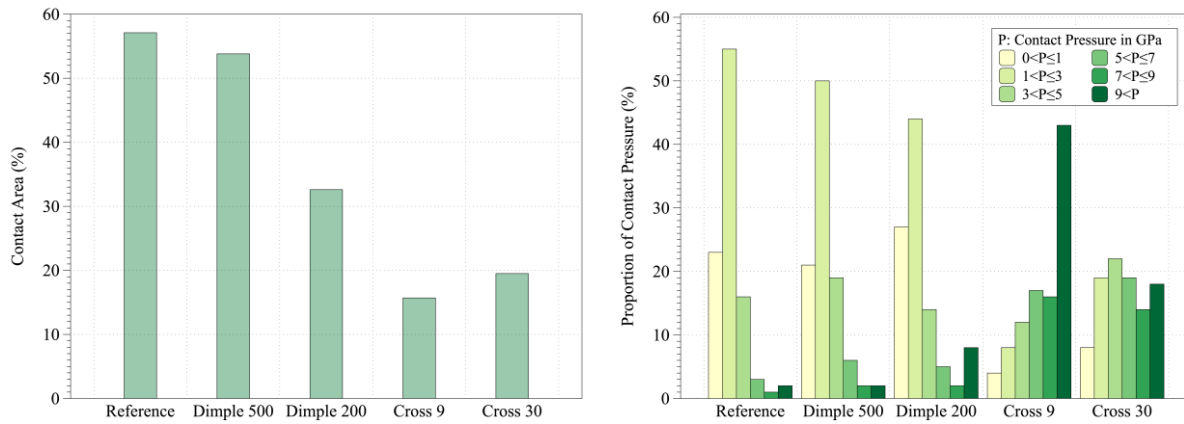
Figure 39: Pressure distribution from the contact simulation results showing (a) the coverage of the contact area on the LST surfaces and (b) the proportion of the contact pressure in different value ranges. (P: contact pressure in GPa) [197].

Compared to the dimples, the cross patterns generally show a smaller contact area and a trend of larger contact pressure. Both of the patterns, Cross9 and Cross30, have a greater proportion in the range between 3 to 7 GPa, which has been suggested to be beneficial for the formation of tribofilm [140]. However, although the growth rate increases with greater pressure, excessively high contact stress can also cause more wear. The significant peak of Cross9 in Figure 39(b) shows that a high percentage of the contact stress was greater than 9 GPa, which was probably beyond the optimum pressure range for tribofilm formation. Therefore, instead of being beneficial, Cross9 can lead to a higher wear rate. In contrast, the Cross30 pattern results in a sufficient increase of pressure for ZDDP promotion but less excessive stress that would further cause a higher wear rate.

After the preliminary experiments of wear evaluation, the best-performed LST pattern style, Cross30, was selected for the following fatigue lifetime experiments. From the Weibull distribution plot shown in Figure 40, the fatigue life of Cross30 increased triple compared with the standard bearings. The difference of the Weibull fitting slopes between Cross30 and the reference is small, indicating the damage mechanisms for both patterns are identical. Although friction can also cause the occurrence of RCF, there was no notable difference among them. Moreover, the wear tracks show no macroscopic abrasive or adhesive wear but only pitting cracks as the failure of fatigue testing. Therefore, the increase of RCF life can be exclusively

attributed to the enhanced growth of the ZDDP antiwear tribofilm and the lubricant storage capacity of the LST patterns.
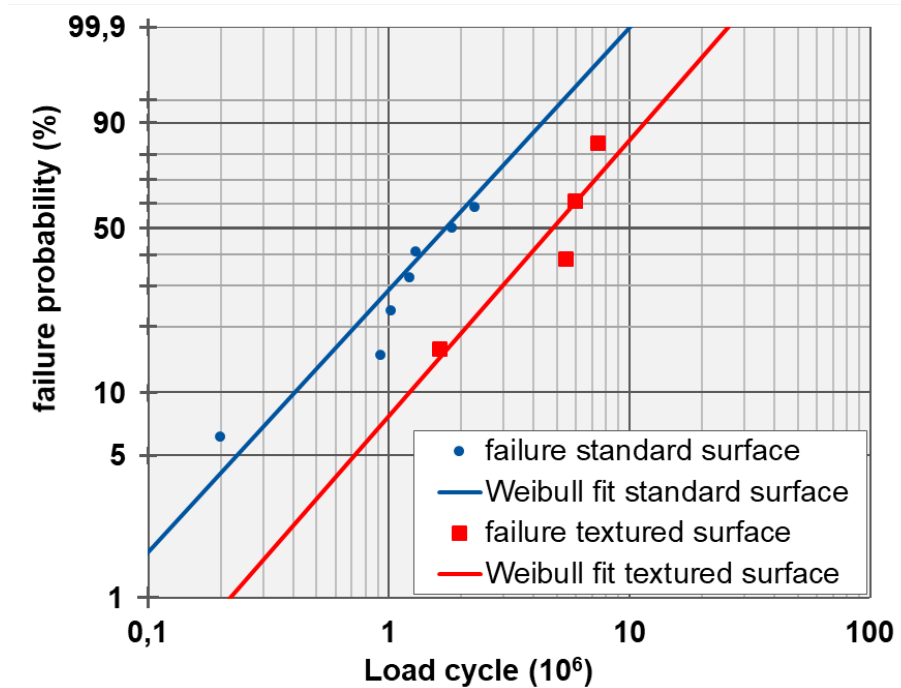

Figure 40: Weibull distribution of the fatigue lifetime tests showing the failure probability of Cross30 and the reference thrust ball bearings [197].

Due to the concern that the increase of contact pressure can cause a detrimental effect, the use of LST to machine components operating in the boundary lubrication regime is still rare. However, the experimental results from the present study show no negative effect on the RCF life testing. The LST surfaces provide better wear protection by the evidence of significantly longer fatigue life, which can be attributed to the growth of ZDDP antiwear tribofilm and the lubricant storage capacity. Therefore, the use of LST in the boundary lubrication regime should be possible for application with further research under different texturing geometry, contact modes, and operating conditions.

5.   Conclusions and Future Works

This doctoral research shows a successful use of LST on thrust rolling bearings in the boundary lubrication regime with enhanced growth of antiwear tribofilm by ZDDP. The experimental results show that the laser textured surfaces have less wear and prevent occurrences of RCF. This conclusion follows from the designed experiments: Firstly, the ZDDP antiwear tribofilm was generated on the surface of rolling bearings without LST patterns, and its chemical composition and phase state were obtained. The tribofilm was characterized by high-resolution analyzing methods to understand the color appearance and the nature of the interface between the tribofilm and the substrate. Secondly, the frictional performance of the laser textured roller bearings was evaluated under lubricated conditions with the addition of ZDDP. Four different geometric designs of the laser patterns were tested for wear evaluations, and the LST pattern with the best tribological performance was selected for the subsequent fatigue tests. Finally, the rolling bearing with suitable LST patterns was examined by fatigue lifetime tests, and the contact distribution affected by surface modification was analyzed by contact simulations. The main findings are summarized as follows:

1. The question about the color appearance of ZDDP tribofilm is answered: The experimental results indicate that it is the chemical constitution, but not only the thickness of the tribofilm affects the color difference. The thickness was found in the same range; however, the chemical analyses of Raman and EDS reveal differences. The blue tribofilm has a higher amount of ZnS and FeS, whereas the brown layers are enriched with more Fe_3O_4.

2. Analyses from both the high-resolution methods, XPS and APT, determined the chemical composition of the ZDDP tribofilm. A sulfur enrichment was found distributed heterogeneously in a range of 5 nm between the tribofilm and the steel substrate. Since ZDDP consists of sulfur, it is natural to detect sulfur in its post product, namely the tribofilm; however, the examining difficulties make it still unclear whether there is an enrichment at the interface. Eventually, the existence of the sulfur enrichment proven by APT supports the predictions according to the HSAB principle.

Dissertation, Chia-Jui HSU

3. The frictional results show that LST is beneficial for application in the boundary lubrication regime, which can be influenced by the pattern geometry and area density. The increase of area density leads to higher surface roughness, and more valley areas provide a larger capacity of lubricant storage. In the present work, since the geometry of the LST patterns between the dimple and the cross is different, both S_k and S_{vk} of the Abbott-Firestone curve (rather than S_{vk} alone) should be involved for assessing the lubricant storage capacity.

4. The laser textured thrust rolling bearing (Cross30) demonstrated a three-fold increase in fatigue lifetime. The improvement is due to the ability of lubricant storage and the enhanced growth of tribofilm. The lubricant retained within the contact prevents lubricant insufficient under boundary lubrication, and the antiwear tribofilm prevents direct contact between surfaces.

5. The contact simulation demonstrates the pressure distribution on the surfaces, which indicates that the textured patterns introduce higher stress to the contact. An increase of contact pressures on the laser textured patterns was found to enhance the formation of ZDDP tribofilm on the cross patterns as LST changes the area of contact. However, the high area density of LST would also lead to excessively high contact stress at the textured peaks, causing a higher wear rate than beneficial effects.

The frictional examinations clearly show the positive effects of the combined use of ZDDP additive and LST. The formation of tribofilm can be enhanced by altering the geometry of the LST patterns. Moreover, even in insufficiently lubricated conditions, LST reduces wear and thus prolongs the lifetime of the thrust rolling bearings. Nevertheless, some foreseeable extension works can be further studied in the future. First of all, a more comprehensive study on the combined use of LST and AW additive is necessary to promote this method to application. Based on the outcome of this dissertation, changes in LST parameters such as height and periodic distance, contact mode, and pattern geometry can alter the performances. A systematic experimental matrix will optimize the design of the LST patterns for various machine elements. Secondly, since this study has solved the concern of the use of LST in boundary lubrication, new approaches and attempts can be introduced into this lubrication regime. Furthermore, contact simulation or in-situ tribotest with optical observation can estimate and determine the pressure and its distribution while for tribofilm formation.

6.   References

[1]   International Energy Agency (IEA). CO2 emisions from fuel combustion. 2019.

[2]   Holmberg K, Erdemir A. Influence of tribology on global energy consumption, costs and emissions. Friction 2017;5:263–84. https://doi.org/10.1007/s40544-017-0183-5.

[3]   Holmberg K, Kivikytö-Reponen P, Härkisaari P, Valtonen K, Erdemir A. Global energy consumption due to friction and wear in the mining industry. Tribol Int 2017. https://doi.org/10.1016/j.triboint.2017.05.010.

[4]   Rosenkranz A, Grützmacher PG, Murzyn K, Mathieu C, Mücklich F. Multi-scale surface patterning to tune friction under mixed lubricated conditions. Appl Nanosci 2019. https://doi.org/10.1007/s13204-019-01055-9.

[5]   Ali MKA, Xianjun H, Abdelkareem MAA, Gulzar M, Elsheikh AH. Novel approach of the graphene nanolubricant for energy saving via anti-friction/wear in automobile engines. Tribol Int 2018. https://doi.org/10.1016/j.triboint.2018.04.004.

[6]   Luo J, Zhou X. Superlubricitive engineering—Future industry nearly getting rid of wear and frictional energy consumption. Friction 2020. https://doi.org/10.1007/s40544-020-0393-0.

[7]   Holmberg K, Erdemir A. The impact of tribology on energy use and CO2 emission globally and in combustion engine and electric cars. Tribol Int 2019. https://doi.org/10.1016/j.triboint.2019.03.024.

[8]   Bahari A, Lewis R, Slatter T. Friction and Wear Phenomena of Vegetable Oil–Based Lubricants with Additives at Severe Sliding Wear Conditions. Tribol Trans 2018. https://doi.org/10.1080/10402004.2017.1290858.

[9]   Shafi WK, Raina A, Ul Haq MI. Friction and wear characteristics of vegetable oils using nanoparticles for sustainable lubrication. Tribol - Mater Surfaces Interfaces 2018. https://doi.org/10.1080/17515831.2018.1435343.

[10]   Kohlhauser B, Ripoll MR, Riedl H, Koller CM, Koutna N, Amsüss A, et al. How to get noWear? – A new take on the design of in-situ formed high performing low-friction tribofilms. Mater Des 2020;190:108519. https://doi.org/10.1016/j.matdes.2020.108519.

[11]   Makowski S, Schaller F, Weihnacht V, Englberger G, Becker M. Tribochemical induced wear and ultra-

6. References

low friction of superhard ta-C coatings. Wear 2017. https://doi.org/10.1016/j.wear.2017.08.015.

[12]   Su, Y. L.; Lin, Y. F.; Yao, S. H.; Hsu CJ, Su YL, Lin YF, Yao SH, Hsu CJ. Effects of tungsten addition on mechanical and tribological properties of carbon nitride prepared by DC magnetron sputtering. Key Eng. Mater., vol. 642, 2015, p. 24–9. https://doi.org/10.4028/www.scientific.net/KEM.642.24.

[13]   Holmberg K, Andersson P, Erdemir A. Global energy consumption due to friction in passenger cars. Tribol Int 2012;47:221–34. https://doi.org/10.1016/j.triboint.2011.11.022.

[14]   Grützmacher PG, Rosenkranz A, Rammacher S, Gachot C, Mücklich F. The influence of centrifugal forces on friction and wear in rotational sliding. Tribol Int 2017. https://doi.org/10.1016/j.triboint.2017.07.021.

[15]   Malevich N, Müller CH, Dreier J, Kansteiner M, Biermann D, De Pinho Ferreira M, et al. Experimental and statistical analysis of the wear of diamond impregnated tools. Wear 2021. https://doi.org/10.1016/j.wear.2020.203574.

[16]   Ma K, Choi UM, Blaabjerg F. Prediction and Validation of Wear-Out Reliability Metrics for Power Semiconductor Devices with Mission Profiles in Motor Drive Application. IEEE Trans Power Electron 2018. https://doi.org/10.1109/TPEL.2018.2798585.

[17]   Hsu SM, Gates RS. Boundary lubricating films: Formation and lubrication mechanism. Tribol Int 2005;38:305–12. https://doi.org/10.1016/j.triboint.2004.08.021.

[18]   Evans HP, Snidle RW, Sharif KJ, Bryant MJ. Predictive modelling of fatigue failure in concentrated lubricated contacts. Faraday Discuss 2012. https://doi.org/10.1039/c2fd00116k.

[19]   Šamánek O, Zimmerman M, Svoboda P, Křupka I, Vrbka M. Influence of Surface Texturing on Lubricant Film Formation and Surface Fatigue. Eng Mech 2010;17:27–36.

[20]   Hammami M, Rodrigues N, Fernandes C, Martins R, Seabra J, Abbes MS, et al. Axle gear oils: Friction, wear and tribofilm generation under boundary lubrication regime. Tribol Int 2017. https://doi.org/10.1016/j.triboint.2017.04.018.

[21]   Pasaribu HR, Lugt PM. The Composition of Reaction Layers on Rolling Bearings Lubricated with Gear Oils and Its Correlation with Rolling Bearing Performance. Tribol Trans 2012. https://doi.org/10.1080/10402004.2011.629403.

[22]   Hsu SM. Boundary lubrication: Current understanding. Tribol Lett 1997;3:1–11. https://doi.org/10.1023/A:1019152331970.

[23]   Faruck AAM, Hsu C-JJ, Doerr N, Weigand M, Gachot C, Mohamed Faruck AA, et al. How lubricant formulations and properties influence the performance of rotorcraft transmissions under loss of

6. References

lubrication conditions. Tribol Int 2020;151:106390. https://doi.org/10.1016/j.triboint.2020.106390.

[24] Evans RD, Doll GL, Hager CH, Howe JY. Influence of steel type on the propensity for tribochemical wear in boundary lubrication with a wind turbine gear oil. Tribol Lett 2010. https://doi.org/10.1007/s11249-009-9565-9.

[25] Johnson KL, Keer LM. Contact Mechanics. J Tribol 1986;108:659. https://doi.org/10.1115/1.3261297.

[26] Richard Booser E. Tribology Data Handbook. 2010. https://doi.org/10.1201/9781420050479.

[27] Xianjun H. Mini Review on the Significance Nano-Lubricants in Boundary Lubrication Regime. Int J Biosens Bioelectron 2017. https://doi.org/10.15406/ijbsbe.2017.02.00014.

[28] Lee B, Yu Y, Cho DS, Cho Y. Role of additive concentration in slow-speed sliding contact under boundary lubrication conditions. J Mech Sci Technol 2019. https://doi.org/10.1007/s12206-019-1029-z.

[29] Tan Y, Ma L. Analytic Calculation and Experimental Study on the Wear of the Slide Guide of Machine Tool Considering Boundary Lubrication. J Tribol 2020. https://doi.org/10.1115/1.4046288.

[30] Spikes H. The history and mechanisms of ZDDP. Tribol Lett 2004;17:469–89. https://doi.org/10.1023/B:TRIL.0000044495.26882.b5.

[31] Gauvin M, Minfray C, Belin M, Aquilanti G, Martin JM, Dassenoy F. Pressure-induced amorphization of zinc orthophosphate-Insight in the zinc coordination by XAS. Tribol Int 2013;67:222–8. https://doi.org/10.1016/j.triboint.2013.07.011.

[32] Minfray C, Le Mogne T, Lubrecht a. a., Martin JM. Experimental simulation of chemical reactions between ZDDP tribofilms and steel surfaces during friction processes. Tribol Lett 2006;21:65–76. https://doi.org/10.1007/s11249-005-9012-5.

[33] Landauer AK, Barnhill WC, Qu J. Correlating mechanical properties and anti-wear performance of tribofilms formed by ionic liquids, ZDDP and their combinations. Wear 2016;354–355:78–82. https://doi.org/10.1016/j.wear.2016.03.003.

[34] Nicholls MA, Do T, Norton PR, Kasrai M, Bancroft GM. Review of the lubrication of metallic surfaces by zinc dialkyl-dithiophosphates. Tribol Int 2005;38:15–39. https://doi.org/10.1016/j.triboint.2004.05.009.

[35] Huynh KK, Tieu KA, Pham ST. Synergistic and Competitive Effects between Zinc Dialkyldithiophosphates and Modern Generation of Additives in Engine Oil. Lubricants 2021.

6. References

https://doi.org/10.3390/lubricants9040035.

[36]   Adebogun A, Hudson R, Breakspear A, Warrens C, Gholinia A, Matthews A, et al. Industrial Gear Oils: Tribological Performance and Subsurface Changes. Tribol Lett 2018. https://doi.org/10.1007/s11249-018-1013-2.

[37]   Minfray C, Martin JM, Esnouf C, Le Mogne T, Kersting R, Hagenhoff B. A multi-technique approach of tribofilm characterisation. Thin Solid Films 2004;447–448:272–7. https://doi.org/10.1016/S0040-6090(03)01064-2.

[38]   Onodera T, Martin JM, Minfray C, Dassenoy F, Miyamoto A. Antiwear chemistry of ZDDP: Coupling classical MD and tight-binding quantum chemical MD methods (TB-QCMD). Tribol Lett 2013;50:31–9. https://doi.org/10.1007/s11249-012-0063-0.

[39]   Minfray C, Martin JM, De Barros MI, Le Mogne T, Kersting R, Hagenhoff B. Chemistry of ZDDP tribofilm by ToF-SIMS. Tribol Lett 2004;17:351–7. https://doi.org/10.1023/B:TRIL.0000044483.68571.49.

[40]   Canning GW, Suominen Fuller ML, Bancroft GM, Kasrai M, Cutler JN, De Stasio G, et al. Spectromicroscopy of tribological films from engine oil additives. Part I. Films from ZDDP's. Tribol Lett 1999;6:159–69. https://doi.org/10.1023/A:1019176110473.

[41]   Martin JM, Onodera T, Minfray C, Dassenoy F, Miyamoto A. The origin of anti-wear chemistry of ZDDP. Faraday Discuss 2012;156:311. https://doi.org/10.1039/c2fd00126h.

[42]   Canter N. ZDDP's uncertain future. Tribol Lubr Technol 2019.

[43]   Dawczyk J, Morgan N, Russo J, Spikes H. Film Thickness and Friction of ZDDP Tribofilms. Tribol Lett 2019;67:34. https://doi.org/10.1007/s11249-019-1148-9.

[44]   Ye J, Araki S, Kano M, Yasuda Y. Nanometer-scale mechanical/structural properties of molybdenum dithiocarbamate and zinc dialkylsithiophosphate tribofilms and friction reduction mechanism. Japanese J Appl Physics, Part 1 Regul Pap Short Notes Rev Pap 2005;44:5358–61. https://doi.org/10.1143/JJAP.44.5358.

[45]   Parsaeian P, Ghanbarzadeh A, Van Eijk MCP, Nedelcu I, Neville A, Morina A. A new insight into the interfacial mechanisms of the tribofilm formed by zinc dialkyl dithiophosphate. Appl Surf Sci 2017;403:472–86. https://doi.org/10.1016/j.apsusc.2017.01.178.

[46]   Greenall A, Neville A, Morina A, Sutton M. Investigation of the interactions between an ovel, organic anti-wear additive, ZDDP and overbased calcium sulphonate. Tribol Int 2012;46:52–61. https://doi.org/10.1016/j.triboint.2011.06.016.

6. References

[47] Ratoi M, Niste VB, Zekonyte J. WS2 nanoparticles – potential replacement for ZDDP and friction modifier additives. RSC Adv 2014;4:21238. https://doi.org/10.1039/c4ra01795a.

[48] Jacobs TDB, Greiner C, Wahl KJ, Carpick RW. Insights into tribology from in situ nanoscale experiments. MRS Bull 2019;44:478–86. https://doi.org/10.1557/mrs.2019.122.

[49] Kovalchenko A, Ajayi O, Erdemir A, Fenske G, Etsion I. The effect of laser surface texturing on transitions in lubrication regimes during unidirectional sliding contact. Tribol Int 2005;38:219–25. https://doi.org/10.1016/j.triboint.2004.08.004.

[50] Rosenkranz A, Grützmacher PG, Gachot C, Costa HL. Surface Texturing in Machine Elements – A Critical Discussion for Rolling and Sliding Contacts. Adv Eng Mater 2019;21:1900194. https://doi.org/10.1002/adem.201900194.

[51] Erdemir A. Review of engineered tribological interfaces for improved boundary lubrication. Tribol Int 2005;38:249–56. https://doi.org/10.1016/j.triboint.2004.08.008.

[52] Kromer R, Costil S, Verdy C, Gojon S, Liao H. Laser surface texturing to enhance adhesion bond strength of spray coatings – Cold spraying, wire-arc spraying, and atmospheric plasma spraying. Surf Coatings Technol 2018;352:642–53. https://doi.org/10.1016/j.surfcoat.2017.05.007.

[53] Gachot C. Laser interference metallurgy of metallic surfaces for tribological applications. Univ Des Saarlandes 2012.

[54] Raillard B, Rémond J, Ramos-Moore E, Souza N, Gachot C, Mücklich F. Wetting properties of steel surfaces modified by laser interference metallurgy. Adv Eng Mater 2013;15:341–6. https://doi.org/10.1002/adem.201200247.

[55] Wang X, Kato K, Adachi K, Aizawa K. The effect of laser texturing of SiC surface on the critical load for the transition of water lubrication mode from hydrodynamic to mixed. Tribol Int 2001;34:703–11. https://doi.org/10.1016/S0301-679X(01)00063-9.

[56] Kovalchenko A, Ajayi O, Erdemir A, Fenske G. Friction and wear behavior of laser textured surface under lubricated initial point contact. Wear 2011;271:1719–25. https://doi.org/10.1016/j.wear.2010.12.049.

[57] Rosenkranz A, Reinert L, Gachot C, Mücklich F. Alignment and wear debris effects between laser-patterned steel surfaces under dry sliding conditions. Wear 2014;318:49–61. https://doi.org/10.1016/j.wear.2014.06.016.

[58] Grützmacher PG, Rosenkranz A, Gachot C. How to guide lubricants - Tailored laser surface patterns on stainless steel. Appl Surf Sci 2016;370:59–66. https://doi.org/10.1016/j.apsusc.2016.02.115.

6. References

[59]   Gachot C, Rosenkranz A, Hsu SM, Costa HL. A critical assessment of surface texturing for friction and wear improvement. Wear 2017;372–373:21–41. https://doi.org/10.1016/j.wear.2016.11.020.

[60]   Lasagni AF, Gachot C, Trinh KE, Hans M, Rosenkranz A, Roch T, et al. Direct laser interference patterning, 20 years of development: from the basics to industrial applications. Laser-Based Micro-Nanoprocessing XI 2017;10092:1009211. https://doi.org/10.1117/12.2252595.

[61]   Catrin R, Gries T, Raillard B, Mücklich F, Migot S, Horwat D. Influence of laser interference patterning on microstructure and friction behavior of gold/yttria-stabilized zirconia nanocomposite thin films. J Mater Res 2012;27:879–85. https://doi.org/10.1557/jmr.2011.443.

[62]   Etsion I, Halperin G, Brizmer V, Kligerman Y. Experimental investigation of laser surface textured parallel thrust bearings. Tribol Lett 2004;17:295–300. https://doi.org/10.1023/B:TRIL.0000032467.88800.59.

[63]   Kovalchenko A, Ajayi O, Erdemir A, Fenske G, Etsion I. The Effect of Laser Texturing of Steel Surfaces and Speed-Load Parameters on the Transition of Lubrication Regime from Boundary to Hydrodynamic. Tribol Trans 2004;47:299–307. https://doi.org/10.1080/05698190490440902.

[64]   Etsion I. State of the Art in Laser Surface Texturing. J Tribol Trans ASME 2005;127:248. https://doi.org/10.1115/1.1828070.

[65]   Rosenkranz A, Stratmann A, Gachot C, Burghardt G, Jacobs G, Mücklich F, et al. Improved wear behavior of cylindrical roller thrust bearings by three-beam laser interference. Adv Eng Mater 2016;18:854–62. https://doi.org/10.1002/adem.201500320.

[66]   Rosenkranz A, Martin B, Bettscheider S, Gachot C, Kliem H, Mücklich F. Correlation between solid-solid contact ratios and lubrication regimes measured by a refined electrical resistivity circuit. Wear 2014;320:51–61. https://doi.org/10.1016/j.wear.2014.08.018.

[67]   Pandey RK, Kalyanasundaram D, Ch VIDYASAGAR KE. An exploration of frictional and vibrational behaviors of textured deep groove ball bearing in the vicinity of requisite minimum load Development of energy efficient rolling bearings with enhanced life View project Deformation behaviour of bulk nanostructured materials View project An exploration of frictional and vibrational behaviors of textured deep groove ball bearing in the vicinity of requisite minimum load. ResearchgateNet n.d. https://doi.org/10.1007/s40544-021-0495-3.

[68]   Bhardwaj V, Pandey RK, Agarwal VK. Performance studies of textured race ball bearing. Ind Lubr Tribol 2019;71:1116–23. https://doi.org/10.1108/ILT-12-2018-0445.

[69]   Wang Z, Gu L, Li L. Experimental studies on the overall efficiency performance of axial piston motor

with a laser surface textured valve plate. Proc Inst Mech Eng Part B J Eng Manuf 2013;227:1049–56. https://doi.org/10.1177/0954405413481516.

[70] Zhang J, Chen Y, Xu B, Chao Q, Zhu Y, Huang X. Effect of surface texture on wear reduction of the tilting cylinder and the valve plate for a high-speed electro-hydrostatic actuator pump. Wear 2018;414–415:68–78. https://doi.org/10.1016/j.wear.2018.08.003.

[71] Ryk G, Kligerman Y, Rings P, Texturing S. Experimental investigation of laser surface texturing for reciprocating automotive components. Tribol Trans 2002;45:444–9. https://doi.org/10.1080/10402000208982572.

[72] Liang X, Wang X, Liu Y, Wang X, Shu G, Zhang Z. Simulation and Experimental Investigation on Friction Reduction by Partial Laser Surface Texturing on Piston Ring. Tribol Trans 2020;63:371–81. https://doi.org/10.1080/10402004.2019.1696433.

[73] Liang G, Schmauder S, Lyu M, Schneider Y, Zhang C, Han Y. An investigation of the influence of initial roughness on the friction and Wear behavior of ground surfaces. Materials (Basel) 2018;11:237. https://doi.org/10.3390/ma11020237.

[74] Shi R, Wang B, Yan Z, Wang Z, Dong L. Effect of surface topography parameters on friction and wear of random rough surface. Materials (Basel) 2019;12:2762. https://doi.org/10.3390/ma12172762.

[75] Meng Y. Is laser surface texturing good or bad for rolling element bearings?-Comments on: "Does laser surface texturing really have a negative impact on the fatigue lifetime of mechanical components?" by Hsu et al. and "An exploration of frictional and vibrationa. Friction 2021;9:1784–6. https://doi.org/10.1007/s40544-021-0519-z.

[76] Kumar V, Verma R, Kango S, Sharma VS. Recent progresses and applications in laser-based surface texturing systems. Mater Today Commun 2021;26:101736. https://doi.org/10.1016/j.mtcomm.2020.101736.

[77] Vlădescu SC, Olver A V., Pegg IG, Reddyhoff T. Combined friction and wear reduction in a reciprocating contact through laser surface texturing. Wear 2016;358–359:51–61. https://doi.org/10.1016/j.wear.2016.03.035.

[78] He D, Zheng S, Pu J, Zhang G, Hu L. Improving tribological properties of titanium alloys by combining laser surface texturing and diamond-like carbon film. Tribol Int 2015;82:20–7. https://doi.org/10.1016/j.triboint.2014.09.017.

[79] Mücklich F, Lasagni A, Daniel C. Laser interference metallurgy - Using interference as a tool for micro/nano structuring. Int J Mater Res 2006;97:1337–44. https://doi.org/10.3139/146.101375.

6. References

[80]   Rycerz P, Olver A, Kadiric A. Propagation of surface initiated rolling contact fatigue cracks in bearing steel. Int J Fatigue 2017;97:29–38. https://doi.org/10.1016/j.ijfatigue.2016.12.004.

[81]   Manieri F, Stadler K, Morales-Espejel GE, Kadiric A. The origins of white etching cracks and their significance to rolling bearing failures. Int J Fatigue 2019;120:107–33. https://doi.org/10.1016/j.ijfatigue.2018.10.023.

[82]   Lorenz SJ, Sadeghi F, Trivedi HK, Rosado L, Kirsch MS, Wang C. An approach for predicting failure mechanism in rough surface rolling contact fatigue. Tribol Int 2021;158. https://doi.org/10.1016/j.triboint.2021.106923.

[83]   Li SX, Su YS, Shu XD, Chen JJ. Microstructural evolution in bearing steel under rolling contact fatigue. Wear 2017;380–381:146–53. https://doi.org/10.1016/j.wear.2017.03.018.

[84]   Maya-Johnson S, Felipe Santa J, Toro A. Dry and lubricated wear of rail steel under rolling contact fatigue - Wear mechanisms and crack growth. Wear 2017;380–381:240–50. https://doi.org/10.1016/j.wear.2017.03.025.

[85]   Sadeghi F, Jalalahmadi B, Slack TS, Raje N, Arakere NK. A review of rolling contact fatigue. J Tribol 2009. https://doi.org/10.1115/1.3209132.

[86]   Borgaonkar A V., Syed I. Effect of coatings on rolling contact fatigue and tribological parameters of rolling/sliding contacts under dry/lubricated conditions: a review. Sadhana - Acad Proc Eng Sci 2020;45:1–16. https://doi.org/10.1007/s12046-020-1266-y.

[87]   Kolivand Li Q Zhang AS. Modeling on contact fatigue under starved lubrication condition. Meccanica n.d.;56. https://doi.org/10.1007/s11012-020-01284-1.

[88]   Qu S, Hu X, Lu F, Lai F, Liu H, Zhang Y, et al. Rolling contact fatigue properties of ultrasonic surface rolling treated 25CrNi2MoV steel under different lubricant viscosities. Int J Fatigue 2021;142:105970. https://doi.org/10.1016/j.ijfatigue.2020.105970.

[89]   Adams DR. Tribological considerations in internal combustion engines. Tribol. Dyn. Engine Powertrain Fundam. Appl. Futur. Trends, Elsevier Ltd.; 2010, p. 251–83. https://doi.org/10.1533/9781845699932.2.251.

[90]   Kapsa P. Environmental effects in fretting. Tribocorrosion Passiv. Met. Coatings, Elsevier; 2011, p. 100–17. https://doi.org/10.1533/9780857093738.1.100.

[91]   Sannino AP, Rack HJ. Dry sliding wear of discontinuously reinforced aluminum composites: review and discussion. Wear 1995;189:1–19. https://doi.org/10.1016/0043-1648(95)06657-8.

[92]   Mang T, Bobzin K, Bartels T. Industrial tribology: Tribosystems, friction, wear and surface

engineering, lubrication. 2011.

[93]   Blau PJ. Friction Measurement. Encycl. Tribol., Springer, Boston, MA; 2013, p. 1343–7. https://doi.org/10.1007/978-0-387-92897-5_171.

[94]   Placzek JD, Boyce DA. Orthopaedic Physical Therapy Secrets. 2006. https://doi.org/10.1016/B978-1-56053-708-3.X5001-6.

[95]   Narayan R. Encyclopedia of biomedical engineering. vol. 1–3. 2019.

[96]   Mang T, Dresel W. Lubricants and Lubrication. 2007. https://doi.org/10.1002/9783527610341.

[97]   Benardos PG, Vosniakos GC. Predicting surface roughness in machining: a review. Int J Mach Tools Manuf 2003;43:833–44. https://doi.org/10.1016/S0890-6955(03)00059-2.

[98]   Ulker O. Surface Roughness of Composite Panels as a Quality Control Tool. Mater 2018, Vol 11, Page 407 2018;11:407. https://doi.org/10.3390/MA11030407.

[99]   Harlin P, Carlsson P, Bexell U, Olsson M. Influence of surface roughness of PVD coatings on tribological performance in sliding contacts. Surf Coatings Technol 2006;201:4253–9. https://doi.org/10.1016/J.SURFCOAT.2006.08.103.

[100] Ghosh G, Sidpara A, Bandyopadhyay PP. Understanding the role of surface roughness on the tribological performance and corrosion resistance of WC-Co coating. Surf Coatings Technol 2019;378:125080. https://doi.org/10.1016/J.SURFCOAT.2019.125080.

[101] Suh AY, Polycarpou AA, Conry TF. Detailed surface roughness characterization of engineering surfaces undergoing tribological testing leading to scuffing. Wear 2003;255:556–68. https://doi.org/10.1016/S0043-1648(03)00224-2.

[102] Puertas Arbizu I, Luis Pérez CJ. Surface roughness prediction by factorial design of experiments in turning processes. J Mater Process Technol 2003;143–144:390–6. https://doi.org/10.1016/S0924-0136(03)00407-2.

[103] Jiang Z, Gao D, Lu Y, Liu X. Optimization of Cutting Parameters for Trade-off Among Carbon Emissions, Surface Roughness, and Processing Time. Chinese J Mech Eng 2019 321 2019;32:1–18. https://doi.org/10.1186/S10033-019-0408-9.

[104] Wahab JA, Ghazali MJ, Yusoff WMW, Sajuri Z. Enhancing material performance through laser surface texturing: a review. Trans Inst Met Finish 2016;94:193–8. https://doi.org/10.1080/00202967.2016.1191141.

[105] Petropoulos GP, Torrance AA, Pandazaras CN. Abbott curves characteristics of turned surfaces. Int J Mach Tools Manuf 2003;43:237–43. https://doi.org/10.1016/S0890-6955(02)00240-7.

6. References

[106] Gadelmawla ES, Koura MM, Maksoud TMA, Elewa IM, Soliman HH. Roughness parameters. J Mater Process Technol 2002;123:133–45. https://doi.org/10.1016/S0924-0136(02)00060-2.

[107] Hamdi A, Merghache SM, Aliouane T. Effect of cutting variables on bearing area curve parameters (BAC-P) during hard turning process. Arch Mech Eng 2020;67:73–95. https://doi.org/10.24425/ame.2020.131684.

[108] Keller J, Fridrici V, Kapsa P, Huard JF. Surface topography and tribology of cast iron in boundary lubrication. Tribol Int 2009;42:1011–8. https://doi.org/10.1016/J.TRIBOINT.2009.02.008.

[109] Blau PJ. On the nature of running-in. Tribol Int 2005;38:1007–12. https://doi.org/10.1016/j.triboint.2005.07.020.

[110] Hu S, Huang W, Brunetiere N, Song Z, Liu X, Wang Y. Stratified effect of continuous bi-Gaussian rough surface on lubrication and asperity contact. Tribol Int 2016;104:328–41. https://doi.org/10.1016/j.triboint.2016.09.009.

[111] Rodrigues TA, Arencibia R V., Costa HL, Da Silva WM. Roughness analysis of electrochemically textured surfaces: Effects on friction and wear of lubricated contacts. Surf Topogr Metrol Prop 2020;8:24011. https://doi.org/10.1088/2051-672X/ab96da.

[112] Ma S, Liu Y, Wang Z, Wang Z, Huang R, Xu J. The effect of honing angle and roughness height on the tribological performance of CuNiCr iron liner. Metals (Basel) 2019;9. https://doi.org/10.3390/met9050487.

[113] Straffelini G. Lubrication and lubricants. Springer Tracts Mech. Eng., vol. 11, 2015, p. 61–84. https://doi.org/10.1007/978-3-319-05894-8_3.

[114] Chu Z, Feng Y, Seeger S. Oil/water separation with selective superantiwetting/superwetting surface materials. Angew Chemie - Int Ed 2015;54:2328–38. https://doi.org/10.1002/anie.201405785.

[115] Persson BNJ, Scaraggi M. On the transition from boundary lubrication to hydrodynamic lubrication insoft contacts. J Phys Condens Matter 2009;21. https://doi.org/10.1088/0953-8984/21/18/185002.

[116] Lubrecht AA, Venner CH, Colin F. Film thickness calculation in elasto-hydrodynamic lubricated line and elliptical contacts: The Dowson, Higginson, Hamrock contribution. Proc Inst Mech Eng Part J J Eng Tribol 2009;223:511–5. https://doi.org/10.1243/13506501JET508.

[117] Hamrock BJ, Schmid SR, Jacobson BO. Fundamentals of Fluid Film Lubrication. 2004. https://doi.org/10.1201/9780203021187.

[118] Frêne J, Nicolas D, Degueurce B, Berthe D, Godet M. Hydrodynamic lubrication: Bearings and thrust

Dissertation, Chia-Jui HSU

bearings. vol. 33. 1997.

[119] Taylor RI. Engine friction: The influence of lubricant rheology. Proc Inst Mech Eng Part J J Eng Tribol 1997;211:235–46. https://doi.org/10.1177/135065019721100306.

[120] Komvopoulos K, Saka N, Suh NP. The Mechanism of Friction in Boundary Lubrication. J Tribol 1985;107:452–62. https://doi.org/10.1115/1.3261108.

[121] Luengo G, Israelachvili J, Granick S. Generalized effects in confined fluids: New friction map for boundary lubrication. Wear 1996;200:328–35. https://doi.org/10.1016/S0043-1648(96)07248-1.

[122] Wang WZ, Chen H, Hu YZ, Wang H. Effect of surface roughness parameters on mixed lubrication characteristics. Tribol Int 2006;39:522–7. https://doi.org/10.1016/J.TRIBOINT.2005.03.018.

[123] Spikes HAH. Mixed lubrication — an overview. Lubr Sci 1997;00:221–53. https://doi.org/10.1002/ls.3010090302.

[124] Faraon IC, Schipper DJ. Stribeck Curve for Starved Line Contacts. J Tribol 2007;129:181. https://doi.org/10.1115/1.2404964.

[125] Dowson D, Higginson GR, Whitaker a V. Elasto-hydrodynamic Lubrication: a Survey of Isothermal Solutions. J Mech Eng Sci 1962;4:121–6. https://doi.org/10.1243/JMES_JOUR_1962_004_018_02.

[126] Stratmann A, Jacobs G, Hsu CJ, Gachot C, Burghardt G. Antiwear tribofilm growth in rolling bearings under boundary lubrication conditions. Tribol Int 2017;113:43–9. https://doi.org/10.1016/j.triboint.2017.03.030.

[127] Spikes HA. Boundary Lubrication and Boundary Films. Tribol Ser 1993;25:331–46. https://doi.org/10.1016/S0167-8922(08)70389-4.

[128] Heuberger R, Rossi A, Spencer ND. XPS study of the influence of temperature on ZnDTP tribofilm composition. Tribol Lett 2007;25:185–96. https://doi.org/10.1007/s11249-006-9166-9.

[129] Persson BNJ. Theory of friction and boundary lubrication. Phys Rev B 1993;48:18140–58. https://doi.org/10.1103/PhysRevB.48.18140.

[130] Kato K. Wear in boundary or mixed lubrication regimes. Tribol Ser 2002;40:3–17. https://doi.org/10.1016/S0167-8922(02)80003-7.

[131] Varlot K, Kasrai M, Martin JM, Vacher B, Bancroft GM, Yamaguchi ES (Chevron), et al. Antiwear film formation of neutral and basic ZDDP : influence of the reaction temperature and of the concentration. Tribol Lett 2000;8:9–16.

[132] Unnikrishnan R, Jain MC, Harinarayan a. K, Mehta a. K. Additive-additive interaction: An XPS study of the effect of ZDDP on the AW/EP characteristic of molybdenum based additives. Wear

2002;252:240–9. https://doi.org/10.1016/S0043-1648(01)00865-1.

[133] Suarez AN. The behaviour of antiwear additives in lubricated rolling-sliding contacts. Lule{\aa} tekniska universitet, 2011. https://doi.org/978-91-7439-212-8.

[134] Fujita H, Spikes HA. Study of zinc dialkyldithiophosphate antiwear film formation and removal processes, part II: Kinetic model. Tribol Trans 2005;48:567–75. https://doi.org/10.1080/05698190500385187.

[135] Fujita H, Glovnea RP, Spikes HA. Study of zinc dialkydithiophosphate antiwear film formation and removal processes, part I: Experimental. Tribol Trans 2005;48:558–66. https://doi.org/10.1080/05698190500385211.

[136] Fujita H, Spikes H a. The formation of zinc dithiophosphate antiwear films. Proc Inst Mech Eng Part J J Eng Tribol 2004;218:265–78. https://doi.org/10.1243/1350650041762677.

[137] Bancroft GM, Kasrai M, Fuller M, Yin Z, Fyfe K, Tan KH. Mechanisms of tribochemical film formation: Stability of tribo- and thermally-generated ZDDP films. Tribol Lett 1997;3:47–51. https://doi.org/10.1023/A:1019179610589.

[138] Fuller M, Yin Z, Kasrai M, Bancroft GM, Yamaguchi ES, Ryason PR, et al. Chemical characterization of tribochemical and thermal films generated from neutral and basic ZDDPs using X-ray absorption spectroscopy. Tribol Int 1997;30:305–15. https://doi.org/10.1016/S0301-679X(96)00059-X.

[139] Fuller MLS, Kasrai M, Bancroft GM, Fyfe K, Tan KH. Solution decomposition of zinc dialkyl dithiophosphate and its effect on antiwear and thermal film formation studied by X-ray absorption spectroscopy. Tribol Int 1998;31:627–44. https://doi.org/10.1016/S0301-679X(98)00084-X.

[140] Gosvami NN, Bares JA, Mangolini F, Konicek AR, Yablon DG, Carpick RW. Mechanisms of antiwear tribofilm growth revealed in situ by single-asperity sliding contacts. Science (80-) 2015;348:102–6. https://doi.org/10.1126/science.1258788.

[141] Mosey NJ, Woo TK, Kasrai M, Norton PR, Bancroft GM, Müser MH. Interpretation of experiments on ZDDP anti-wear films through pressure-induced cross-linking. Tribol Lett 2006;24:105–14. https://doi.org/10.1007/s11249-006-9040-9.

[142] Zhang Z, Yamaguchi ES, Kasrai M, Bancroft GM. Tribofilms generated from ZDDP and DDP on steel surfaces: Part 1, growth, wear and morphology. Tribol Lett 2005;19:211–20. https://doi.org/10.1007/s11249-005-6148-2.

[143] Gachot C, Hsu C, Suárez S, Grützmacher P, Rosenkranz A, Stratmann A, et al. Microstructural and Chemical Characterization of the Tribolayer Formation in Highly Loaded Cylindrical Roller Thrust

6. References

Bearings. Lubricants 2016;4:1–11. https://doi.org/10.3390/lubricants4020019.

[144] Martin JM, Onodera T, De Barros Bouchet MI, Hatakeyama N, Miyamoto A. Anti-wear chemistry of ZDDP and calcium borate nano-additive. Coupling experiments, chemical hardness predictions, and MD calculations. Tribol Lett 2013;50:95–104. https://doi.org/10.1007/s11249-013-0108-z.

[145] Martin JM, Grossiord C, Le Mogne T, Igarashi J. Transfer films and friction under boundary lubrication. Wear 2000;245:107–15. https://doi.org/10.1016/S0043-1648(00)00471-3.

[146] Njiwa P, Minfray C, Le Mogne T, Vacher B, Martin JM, Matsui S, et al. Zinc dialkyl phosphate (ZP) as an anti-wear additive: Comparison with ZDDP. Tribol Lett 2011;44:19–30. https://doi.org/10.1007/s11249-011-9822-6.

[147] Martin JM, Grossiord C, Le Mogne T, Bec S, Tonck A. The two-layer structure of Zndtp tribofilms, Part I: AES, XPS and XANES analyses. Tribol Int 2001;34:523–30. https://doi.org/10.1016/S0301-679X(01)00029-9.

[148] Guo W, Zhou Y, Sang X, Leonard DN, Qu J, Poplawsky JD. Atom Probe Tomography Unveils Formation Mechanisms of Wear-Protective Tribofilms by ZDDP, Ionic Liquid, and Their Combination. ACS Appl Mater Interfaces 2017;9:23152–63. https://doi.org/10.1021/acsami.7b04719.

[149] Miranda-Medina M de L, Tomastik C, Truglas T, Groiss H, Jech M. Effect of engine oil additives reduction on the tribofilm structure of a cylinder liner model surface. Ind Lubr Tribol 2019;ahead-of-p. https://doi.org/10.1108/ilt-05-2019-0193.

[150] De Barros MII, Bouchet J, Raoult I, Le Mogne T, Martin JMM, Kasrai M, et al. Friction reduction by metal sulfides in boundary lubrication studied by XPS and XANES analyses. Wear 2003;254:863–70. https://doi.org/10.1016/S0043-1648(03)00237-0.

[151] Martin JM. Antiwear mechanisms of zinc dithiophosphate: a chemical hardness approach. Tribol Lett 1999;6:1–8. https://doi.org/10.1023/A:1019191019134.

[152] Smith GC, Bell JC. Multi-technique surface analytical studies of automotive anti-wear films. Appl Surf Sci 1999;144–145:222–7. https://doi.org/10.1016/S0169-4332(98)00801-0.

[153] Bell JC, Delargy KM, Seeney AM. The Removal of Substrate Material through Thick Zinc Dithiophosphate Anti-Wear Films. Tribol Ser 1992;21:387–96. https://doi.org/10.1016/S0167-8922(08)70546-7.

[154] Shimizu Y, Spikes HA. The Tribofilm Formation of ZDDP Under Reciprocating Pure Sliding Conditions. Tribol Lett 2016;64:1–11. https://doi.org/10.1007/s11249-016-0776-6.

[155] Soltanahmadi S, Morina A, van Eijk MCP, Nedelcu I, Neville A. Experimental observation of zinc

dialkyl dithiophosphate (ZDDP)-induced iron sulphide formation. Appl Surf Sci 2017;414:41–51. https://doi.org/10.1016/j.apsusc.2017.04.023.

[156] Dorgham A, Azam A, Morina A, Neville A. On the Transient Decomposition and Reaction Kinetics of Zinc Dialkyldithiophosphate. ACS Appl Mater Interfaces 2018;10:44803–14. https://doi.org/10.1021/acsami.8b08293.

[157] Zhou Y, Leonard DN, Guo W, Qu J. Understanding Tribofilm Formation Mechanisms in Ionic Liquid Lubrication. Sci Rep 2017;7:1–8. https://doi.org/10.1038/s41598-017-09029-z.

[158] Schawlow AL, Townes CH. Infrared and optical masers. Phys Rev 1958. https://doi.org/10.1103/PhysRev.112.1940.

[159] Hecht E. Optics. Pearson; 2017.

[160] Steen WM, Mazumder J. Laser material processing: Fourth edition. 2010. https://doi.org/10.1007/978-1-84996-062-5.

[161] Martens LC. Laser physics and a review of laser applications in dentistry for children. Eur Arch Paediatr Dent 2011;12:61–7. https://doi.org/10.1007/BF03262781.

[162] Fernandes Andrade D, Pereira-Filho ER, Amarasiriwardena D. Current trends in laser-induced breakdown spectroscopy: a tutorial review. Appl Spectrosc Rev 2021;56:98–114. https://doi.org/10.1080/05704928.2020.1739063.

[163] Sinko JE, Oh BI. The Bouguer-Lambert-Beer absorption law and non-planar geometries. AIP Conf. Proc., vol. 1402, 2011, p. 245–57. https://doi.org/10.1063/1.3657031.

[164] Eisfeld E, Roth J. Atomistic simulations of ultra-short pulse laser ablation of aluminum: Validity of the Lambert-Beer law. Adv Opt Technol 2018;7:189–96. https://doi.org/10.1515/aot-2018-0005.

[165] Gamaly EG, Rode A V., Luther-Davies B, Tikhonchuk VT. Ablation of solids by femtosecond lasers: Ablation mechanism and ablation thresholds for metals and dielectrics. Phys Plasmas 2002;9:949. https://doi.org/10.1063/1.1447555.

[166] Bergström D, Powell J, Kaplan AFH. The absorptance of steels to Nd:YLF and Nd:YAG laser light at room temperature. Appl Surf Sci 2007. https://doi.org/10.1016/j.apsusc.2006.11.018.

[167] Russbueldt P, Mans T, Hoffmann D, Schippel S. Ultrashort Pulse Laser Technology. vol. 195. Springer; 2016.

[168] Shirk MD, Molian PA. A review of ultrashort pulsed laser ablation of materials. J Laser Appl 1998;10:18–28. https://doi.org/10.2351/1.521827.

[169] Lanzafame RJ, Naim JO, Rogers DW, Hinshaw JR. Comparison of continuous-wave, chop-wave, and

Dissertation, Chia-Jui HSU

6. References

super pulse laser wounds. Lasers Surg Med 1988;8:119–24. https://doi.org/10.1002/lsm.1900080205.

[170] Demir AG, Colombo P, Previtali B. From pulsed to continuous wave emission in SLM with contemporary fiber laser sources: effect of temporal and spatial pulse overlap in part quality. Int J Adv Manuf Technol 2017;91:2701–14. https://doi.org/10.1007/s00170-016-9948-7.

[171] Simonds BJ, Meadows HJ, Misra S, Ferekides C, Dale PJ, Scarpulla MA. Laser processing for thin film chalcogenide photovoltaics: a review and prospectus. J Photonics Energy 2015. https://doi.org/10.1117/1.jpe.5.050999.

[172] Wellershoff SS, Hohlfeld J, Güdde J, Matthias E. The role of electron-phonon coupling in femtosecond laser damage of metals. Appl Phys A Mater Sci Process 1999;69:99–107. https://doi.org/10.1007/s003390051362.

[173] Le Harzic R, Huot N, Audouard E, Jonin C, Laporte P, Valette S, et al. Comparison of heat-affected zones due to nanosecond and femtosecond laser pulses using transmission electronic microscopy. Appl Phys Lett 2002;80:3886–8. https://doi.org/10.1063/1.1481195.

[174] Leitz KH, Redlingshöer B, Reg Y, Otto A, Schmidt M. Metal ablation with short and ultrashort laser pulses. Phys Procedia 2011;12:230–8. https://doi.org/10.1016/j.phpro.2011.03.128.

[175] Gecys P, Markauskas E, Gedvilas M, Raciukaitis G, Repins I, Beall C. Ultrashort pulsed laser induced material lift-off processing of CZTSe thin-film solar cells. Sol Energy 2014;102:82–90. https://doi.org/10.1016/j.solener.2014.01.013.

[176] Shugaev M V., Wu C, Armbruster O, Naghilou A, Brouwer N, Ivanov DS, et al. Fundamentals of ultrafast laser-material interaction. MRS Bull 2016;41:960–8. https://doi.org/10.1557/mrs.2016.274.

[177] Dubey AK, Yadava V. Laser beam machining—A review. Int J Mach Tools Manuf 2008;48:609–28. https://doi.org/10.1016/J.IJMACHTOOLS.2007.10.017.

[178] Etsion I, Kligerman Y, Halperin G. Analytical and experimental investigation of laser-textured mechanical seal faces. Tribol Trans 1999. https://doi.org/10.1080/10402009908982248.

[179] Li X, Bhushan B. Micromechanical and tribological characterization of hard amorphous carbon coatings as thin as 5 nm for magnetic recording heads. Wear 1998;220:51–8. https://doi.org/10.1016/S0043-1648(98)00242-7.

[180] Gachot C, Rosenkranz A, Reinert L, Ramos-Moore E, Souza N, Müser MH, et al. Dry friction between laser-patterned surfaces: Role of alignment, structural wavelength and surface chemistry. Tribol Lett 2013;49:193–202. https://doi.org/10.1007/s11249-012-0057-y.

6. References

[181] Ripoll MR, Podgornik B, Vižintin J. Finite element analysis of textured surfaces under reciprocating sliding. Wear 2011;271:952–9. https://doi.org/10.1016/j.wear.2011.04.003.

[182] Joshi GS, Putignano C, Gaudiuso C, Stark T, Kiedrowski T, Ancona A, et al. Effects of the micro surface texturing in lubricated non-conformal point contacts. Tribol Int 2018;127:296–301. https://doi.org/10.1016/j.triboint.2018.06.021.

[183] Costa HL, Hutchings IM. Hydrodynamic lubrication of textured steel surfaces under reciprocating sliding conditions. Tribol Int 2007;40:1227–38. https://doi.org/10.1016/j.triboint.2007.01.014.

[184] Fowell M, Olver A V., Gosman AD, Spikes HA, Pegg I. Entrainment and inlet suction: Two mechanisms of hydrodynamic lubrication in textured bearings. J Tribol 2007;129:336–47. https://doi.org/10.1115/1.2540089.

[185] Fowell MT, Medina S, Olver A V., Spikes HA, Pegg IG. Parametric study of texturing in convergent bearings. Tribol Int 2012;52:7–16. https://doi.org/10.1016/j.triboint.2012.02.013.

[186] Gropper D, Wang L, Harvey TJ, Meck KD, Gviniashvili V. Influence of surface texturing on the performance of tilting pad thrust bearings. Soc. Tribol. Lubr. Eng. Annu. Meet. Exhib. 2016, 2016.

[187] Hsu SM. Boundary Lubrication of Materials. MRS Bull 1991;16:54–8. https://doi.org/10.1557/S0883769400055846.

[188] Georges JM, Martin JM, Mathia T, Kapsa P, Meille G, Montes H. Mechanism of boundary lubrication with zinc dithiophosphate. Wear 1979;53:9–34. https://doi.org/10.1016/0043-1648(79)90212-6.

[189] Alamri S, Fraggelakis F, Kunze T, Krupop B, Mincuzzi G, Kling R, et al. On the interplay of DLIP and LIPSS upon ultra-short laser pulse irradiation. Materials (Basel) 2019;12:1018. https://doi.org/10.3390/ma12071018.

[190] Lasagni A, Holzapfel C, Weirich T, Mu F, Mücklich F. Laser interference metallurgy: A new method for periodic surface microstructure design on multilayered metallic thin films. Appl Surf Sci 2007;253:8070–4. https://doi.org/10.1016/j.apsusc.2007.02.092.

[191] Mücklich F, Lasagni   a., Daniel C. Laser interference metallurgy - Periodic surface patterning and formation of intermetallics. Intermetallics 2005;13:437–42. https://doi.org/10.1016/j.intermet.2004.07.005.

[192] Lasagni A, Benke D, Kunze T, Bieda M, Eckhardt S, Roch T, et al. Bringing the direct laser interference patterning method to industry: A one tool-complete solution for surface functionalization. J Laser Micro Nanoeng 2015. https://doi.org/10.2961/jlmn.2015.03.0019.

[193] Duarte M, Lasagni A, Giovanelli R, Narciso J, Louis E, Mücklich F. Increasing lubricant film lifetime by

grooving periodical patterns using laser interference metallurgy. Adv Eng Mater 2008;10:554–8. https://doi.org/10.1002/adem.200700321.

[194] Rosenkranz A, Jaeger S, Gachot C, Vogel S, Mücklich F. Wear Behavior of Laser-Patterned Piston Rings in Squeeze Film Dampers. Adv Eng Mater 2015:n/a-n/a. https://doi.org/10.1002/adem.201400481.

[195] Trinh KE, Tsipenyuk A, Varenberg M, Rosenkranz A, Souza N, Mücklich F, et al. Wear debris and electrical resistance in textured Sn-coated Cu contacts subjected to fretting. Wear 2015;344–345:86–98. https://doi.org/10.1016/j.wear.2015.10.010.

[196] Hans M, Müller F, Grandthyll S, Hüfner S, Mücklich F. Anisotropic wetting of copper alloys induced by one-step laser micro-patterning. Appl Surf Sci 2012;263:416–22. https://doi.org/10.1016/j.apsusc.2012.09.071.

[197] Hsu C-J, Stratmann A, Medina S, Jacobs G, Mücklich F, Gachot C. Does laser surface texturing really have a negative impact on the fatigue lifetime of mechanical components? Friction 2021:1–10.

[198] Pavliček P, Hýbl O. White-light interferometry on rough surfaces - Measurement uncertainty caused by surface roughness. Appl Opt 2008. https://doi.org/10.1364/AO.47.002941.

[199] Breitenbach J, Schrof W, Neumann J. Confocal raman-spectroscopy: Analytical approach to solid dispersions and mapping of drugs. Pharm Res 1999;16:1109–13. https://doi.org/10.1023/A:1018956304595.

[200] Reddy SM, Saxey DW, Rickard WDA, Fougerouse D, Montalvo SD, Verberne R, et al. Atom Probe Tomography: Development and Application to the Geosciences. Geostand Geoanalytical Res 2020. https://doi.org/10.1111/ggr.12313.

[201] Miller MK, Forbes RG. Atom probe tomography. Mater Charact 2009. https://doi.org/10.1016/j.matchar.2009.02.007.

[202] Kelly TF, Miller MK. Invited review article: Atom probe tomography. Rev Sci Instrum 2007;78. https://doi.org/10.1063/1.2709758.

[203] Kim YJ, Baik S Il, Bertolucci-Coelho L, Mazzaferro L, Ramirez G, Erdermir A, et al. Atom-probe tomography of tribological boundary films resulting from boron-based oil additives. Scr Mater 2016;111:64–7. https://doi.org/10.1016/j.scriptamat.2015.08.015.

[204] Kelly TF, Larson DJ. Atom probe tomography 2012. Annu Rev Mater Res 2012;42:1–31. https://doi.org/10.1146/annurev-matsci-070511-155007.

[205] Kelly TF, Larson DJ, Thompson K, Alvis RL, Bunton JH, Olson JD, et al. Atom Probe Tomography of Electronic Materials. Annu Rev Mater Res 2007;37:681–727.

6. References

https://doi.org/10.1146/annurev.matsci.37.052506.084239.

[206] Egerton RF. Physical principles of electron microscopy. Springer; 2005.

[207] Sina Ebnesajjad. 2 Surface Tension and Its Measurement. Surf Treat Mater Adhes Bond 2006:9–28.

[208] Langford RM, Rogers M. In situ lift-out: Steps to improve yield and a comparison with other FIB TEM sample preparation techniques. Micron 2008. https://doi.org/10.1016/j.micron.2008.02.006.

[209] Andersson T. The Boundary Element Method applied to Two-Dimensional Contact Problems with Friction. Bound Elem Methods 1981:239–58. https://doi.org/10.1007/978-3-662-11270-0_16.

[210] Xu Y, Jackson RL. Boundary element method (BEM) applied to the rough surface contact vs. BEM in computational mechanics. Frict 2018 74 2018;7:359–71. https://doi.org/10.1007/S40544-018-0229-3.

[211] Katsikadelis JT. Boundary Elements: Theory and Applications. Bound. Elem. Theory Appl., 2002, p. 143–200.

[212] Kuo C-H. Boundary Element Methods for Contact Analysis. Encycl Tribol 2013:255–8. https://doi.org/10.1007/978-0-387-92897-5_517.

[213] Polonsky IA, Keer LM. A numerical method for solving rough contact problems based on the multi-level multi-summation and conjugate gradient techniques. Wear 1999;231:206–19. https://doi.org/10.1016/S0043-1648(99)00113-1.

[214] Kubiak KJ, Mathia TG, Bigerelle M. Influence of roughness on ZDDP tribofilm formation in boundary lubricated fretting. Tribol - Mater Surfaces Interfaces 2012;6:182–8. https://doi.org/10.1179/1751584X12Y.0000000020.

[215] Schmaltz G. Technische Oberflächenkunde. Berlin, Heidelberg: Springer Berlin Heidelberg; 1936. https://doi.org/10.1007/978-3-642-51820-1.

[216] Hsu CJ, Barrirero J, Merz R, Stratmann A, Aboulfadl H, Jacobs G, et al. Revealing the interface nature of ZDDP tribofilm by X-ray photoelectron spectroscopy and atom probe tomography. Ind Lubr Tribol 2020;72:923–30. https://doi.org/10.1108/ILT-01-2020-0035.

[217] Stratmann A, Burghardt G, Jacobs G. Influence of Operating Conditions and Additive Concentra- tion on the Formation of Anti-wear Layers in Roller Bearings n.d.

[218] Hsu C-J, Stratmann A, Rosenkranz A, Gachot C. Enhanced Growth of ZDDP-Based Tribofilms on Laser-Interference Patterned Cylinder Roller Bearings. Lubricants 2017;5:39. https://doi.org/10.3390/lubricants5040039.

[219] Brafman O, Mitra SS. Raman effect in wurtzite- and zinc-blende-type ZnS single crystals. Phys Rev

6. References

1968;171:931–4. https://doi.org/10.1103/PhysRev.171.931.

[220] Ushioda S. Raman scattering from phonons in iron pyrite (FeS2). Solid State Commun 1972;10:307–10. https://doi.org/10.1016/0038-1098(72)90013-0.

[221] Berkani S, Dassenoy F, Minfray C, Martin JM, Cardon H, Montagnac G, et al. Structural changes in tribo-stressed zinc polyphosphates. Tribol Lett 2013;51:489–98. https://doi.org/10.1007/s11249-013-0188-9.

[222] de Faria DLA, Venâncio Silva S, de Oliveira MT. Raman microspectroscopy of some iron oxides and oxyhydroxides. J Raman Spectrosc 2002;28:873–8. https://doi.org/10.1002/(sici)1097-4555(199711)28:11<873::aid-jrs177>3.3.co;2-2.

7. Figures

7. Figures

7. Figures

8. Tables

Dissertation, Chia-Jui HSU

8. Tables

Dissertation, Chia-Jui HSU

9. PAPER I

Authors:

Carsten Gachot[1,*], Chia-Jui Hsu[1], Sebastián Suárez[1], Philipp Grützmacher[1], Andreas Rosenkranz[1,2], Andreas Stratmann[3], Georg Jacobs[3]

[1] Department of Material Science and Engineering, Saarland University, Saarbrücken 66123, Germany

[2] Department of Physics, Pontifical Catholic University of Chile, Santiago de Chile 7820436, Chile

[3] Institute for Machine Elements and Machine Design, RWTH Aachen, 52062 Aachen, Germany

Dissertation, Chia-Jui HSU

Microstructural and Chemical Characterization of the Tribolayer Formation in Highly Loaded Cylindrical Roller Thrust Bearings

Carsten Gachot [1],*, ChiaJui Hsu [1], Sebastián Suárez [1], Philipp Grützmacher [1], Andreas Rosenkranz [1,2], Andreas Stratmann [3] and Georg Jacobs [3]

[1] Department of Material Science and Engineering, Saarland University, Saarbrücken 66123, Germany; chiajui.hsu@uni-saarland.de (C.H.); s.suarez@mx.uni-saarland.de (S.S.); philipp.gruetzmacher@uni-saarland.de (P.G.); a.rosenkranz@mx.uni-saarland.de (A.R.)

[2] Department of Physics, Pontifical Catholic University of Chile, Santiago de Chile 7820436, Chile

[3] Institute for Machine Elements and Machine Design, RWTH Aachen, 52062 Aachen, Germany; stratmann@ime.rwth-aachen.de (A.S.); jacobs@ime.rwth-aachen.de (G.J.)

* Correspondence: c.gachot@mx.uni-saarland.de; Tel.: +49-0681-302-70554; Fax: +49-0681-302-70502

Abstract: Zinc dithiophosphates (ZDDP) have been widely applied in automobile industry for over 70 years as a lubricant additive for wear protection. Tribolayers have been described as blue- and brown-colored layers on surfaces observed by microscopical observation or even bare eye presumably as a consequence of layer thickness or chemical composition. However, the reaction pathways of ZDDP tribolayers are still not yet fully understood. In the present study, the difference between the blue- and brown-colored tribolayers has been revealed by high resolution methods in cylindrical roller thrust bearings at relatively high contact pressures of around 1.92 GPa. After running a FE8 standard bearing test with a normal load of 80 kN and a temperature of 60 °C, said tribolayers could be identified on the bearing surfaces. By using Raman spectroscopy, it could be shown that the blue-colored layers are enriched by FeS and ZnS whereas the brown-colored layers show a significant amount of Fe_3O_4. This is an interesting finding as it clearly shows a correlation between the color appearance of the films and the chemical composition besides potential film thickness variations. Finally, transmission electron microscopy verified the amorphous nature of the formed tribolayer which is in a good agreement with literature.

Keywords: Lubrication; additives; ZDDP; tribolayer; bearings; microstructure

1. Introduction

Nowadays, there is pushing demand in fuel economy for passenger vehicles in order to fulfill legislative requirements for CO_2 emissions. This in turn leads to the introduction of ultra-low viscosity lubricants which could be one efficient way for lubricants to contribute to the fuel economy performance of passenger cars by reducing shear forces. However, a decrease in lubricant viscosity will result in thinner oil films and thus it will be more difficult for the oil to keep the loaded contacts efficiently apart from each other. This may imply a transition from full film to mixed lubrication with potentially accelerated wear rates and locally increased friction [1]. In order to avoid detrimental impacts on the engine and all its components it is necessary to add for example extreme pressure (EP) or anti wear (AW) additives which have the ability to form friction and wear reducing tribolayers [1]. However, the prediction of the forming tribolayers is highly complicated by operating conditions such as load, speed, and temperature. For that reason, additives are used in high concentrations to guarantee the formation and durability [2]. In this context, zinc dithiophosphates (ZDDPs) are widely

used as lubricant additives. The triumphal procession of ZDDP in the automotive industry already started more than 70 years ago [3]. ZDDP acts as an anti-wear agent, antioxidant, and corrosion inhibitor by decomposing peroxide and effectively destroying peroxy radicals. Interestingly, also the reaction products of ZDDP with peroxide and the respective radicals are again strongly efficient in corrosion inhibition [3]. The friction reducing properties of ZDDP are mainly attributed to an increased load support, beneficial mechanical properties by preferential shearing, removal of Fe_2O_3 particles, and finally the surface protection against corrosion. The growth and removal rate of the tribolayers is a highly dynamic process [4].

Apart from the abovementioned positive effects of ZDDP as a lubricant additive, it is well known that sulphur and phosphorous oxides as well as ash may negatively affect the effective life of exhaust catalysts [1]. Additionally, due to phosphorous and sulphur limits in engine oil specifications, it is considered to progressively reduce the usage of ZDDP or even to replace it [5]. A successful reduction or replacement certainly needs a thorough understanding of the governing mechanisms. It is well known that effective tribolayers can be realized by thermal or tribomechanical activation in loaded contacts [6]. Fujita and Spikes studied the morphology of the tribolayers for different temperatures and contact pressures up to 950 MPa [6]. They could show that pronounced tribolayers under thermal activation are only possible at temperatures higher than 150 °C, whereas loaded conditions already yield in an efficient tribolayer at room temperature. Although quite similar regarding their composition, Bancroft *et al.* proved that the tribomechanically induced reaction layers are more wear resistant than the thermally activated layers [7].

A closer look at the layer morphology shows some important aspects. According to the well-established model by Schmaltz, the boundary layer system typically consists of an inner and outer boundary layer [8]. The inner layer (tribomutation layer) is a fine-crystalline zone resulting from finishing processes or surface deformations with a thickness around 400 nm up to 5 µm (depending on operating conditions). In contrast to that, the outer boundary layer is composed of an oxide layer (<100 nm) followed by a reaction- or tribolayer (<150 nm thickness) and finally an adsorption layer on top [8]. The reaction layer is particularly interesting as it is responsible for the friction and wear reduction. Usually, this reaction layer is rough and patchy mainly composed of pyro- and orthophosphate glasses on the bulk level with an additional nanoscale layer of zinc polyphosphates and a sulphur-rich layer of typically 20 nm close to the metal surface [9]. Over the years, lots of microstructural studies and investigations related to the chemical nature of the reaction layers were done. In particular, Martin *et al.* applied analytical techniques such as electron energy loss spectroscopy (EELS), X-ray adsorption fine structure analysis (EXAFS) or X-ray absorption near-edge spectroscopy (XANES) to reveal the chemical composition and structure of said layers [10–13]. Despite the use of high resolution and sophisticated analytical methods, there is still a controversial issue concerning the specific reaction pathways and kinetics of the ZDDP layer formation [1]. Some recent progress was made by using, for example, classical molecular dynamics simulations (MD simulations) coupled with tight binding quantum chemical MD [14]. Mosey *et al.* explained the positive effects of ZDDP by a cross-linking of phosphates under sufficiently high contact pressure [15]. Gauvin *et al.* and Berkani *et al.* could experimentally verify the simulations by spectroscopic methods under contact pressures of up to 7 GPa [16,17]. However, studies referring to the transfer of these findings to highly loaded cylindrical roller thrust bearings are scarce in literature. Moreover, the role and origin of typically observed blue- and brown-colored films on the contacting surfaces are still not fully understood. According to Hsu, the different colors of the layers (e.g., blue or brown films) are due to thickness differences [18].

In this research contribution, we would like to study those brown- and blue-colored films in highly loaded cylindrical roller thrust bearings in more detail by various advanced and high resolution techniques such as Raman spectroscopy and transmission electron microscopy (TEM). For a given load of 80 kN and an operating temperature of 60 °C in a roller bearing lubricant test rig (FE8 test according to DIN 51819-3 [19]), the speed, as one decisive factor for the film formation, was varied between 10, 15, and 20 rpm. Below 10 rpm, at the given load and temperature, no protective tribolayer can be

detected [20]. With increasing speed, there is a shift in the amount of blue- and brown-colored regions. As the appearance of blue and brown regions on the loaded surfaces usually indicates the successful formation of the wear protective tribolayer and is also most pronounced for the highest applied speed at 20 rpm, a stronger emphasis is put on analyzing said colored regions for this particular speed within this research work.

2. Experimental Section

2.1. Materials and FE8 Testing

In the present study, tribofilms were formed at the interface of cylindrical thrust roller bearings (Type 81212), made of a 100Cr6 bearing steel (52100) with the nominal chemical composition provided by the supplier (see Table 1, by applying a modified FE8 test corresponding to DIN 51819-3 [19]. A mineral oil of class ISO VG 100 is used as base oil and mixed with ZDDP additive. During the test, abundant lubricant was delivered to the area of contact by a circulation pump. In this study, rotational speed was adjusted at 10, 15, and 20 rpm with 10 rpm as a lower limit below which no tribolayer was induced at the given testing conditions. The test was run at 60 °C with an axial load of 80 kN, which corresponds to a Hertzian pressure of 1.92 GPa. The total testing time was 2 h. After the test, the surface was cleaned by using benzene and isopropanol to remove the residual lubricant, abrasives, and contaminants.

Table 1. Chemical composition (in wt %) of 100Cr6 (52100) bearing steel provided by the supplier.

Cr	C	Mn	Si	P_{max}	S_{max}	Cu_{max}	Mo_{max}	Al_{max}
1.35–1.6	0.9–1.05	0.25–0.45	0.15–0.35	0.025	0.015	0.3	0.1	0.05

2.2. Chemical Analysis

Chemical properties have been examined by Raman spectroscopy equipped with a grating of 2400 lines·mm^{-1} and a spectral resolution up to 1.2 cm^{-1}. 532 nm excitation wavelength laser source was provided with a power of 50 mW, and set as 10% of energy to prevent thermal effect to the tribolayer. The spectrum between 200 and 1500 cm^{-1} Raman shift has been obtained within 20 s acquisition time. After Raman acquisition, the spot focus had been examined by optical microscopy in order to check that there is no damage due to the laser beam exposure. The laser beam was focused on the surface by a 50× object lens with a final spot size of nearly 4 μm^2 for the subsequent analysis of the different colored regions of the worn ring surface. Moreover, energy dispersive X-ray spectroscopy (EDS) was used to examine the chemical composition in blue- and brown-colored regions. For that purpose, EDS line scans were performed at 20 kV and 100 kV (TEM-EDS) electron voltage and a dwell time of 2400 ms. By marking the respective positions, the resulting EDS line scans were compared with light microscopic images.

2.3. Topography and Microstructural Analysis

The overall morphology and topography were obtained by using light microscopy (Olympus BX 60, location) and white light interferometry (WLI, Zygo NewView 7300, location).

Scanning electron and focused ion beam microscopy (SEM/FIB, Dual Beam workstation Helios NanoLab FEI, location) were applied to observe the morphological properties on the surface and to prepare thin foils for subsequent analysis by TEM. A JEOL 2010F TEM was used for investigating the tribofilm morphology in more detail and diffraction images were collected to prove the amorphous/crystalline nature of the tribofilm.

3. Results and Discussion

Systematic studies on the tribofilm formation using ZDDP as an additive are rather scarce for highly loaded contacts *i.e.*, contact pressure higher than 1 GPa. For that reason, the tribolayer formation

on the surface of highly loaded cylinder roller thrust bearing rings at 1.92 GPa has been examined in the present study by high resolution and complementary characterization techniques. The tribological behavior of the used mineral oil of class ISO VG 100 mixed with ZDDP was tested in a modified FE8 test rig (DIN 51819-3). Here, the test rig is modified in terms of torque measurement and axial load supply which is done hydraulically [20]. Two cylindrical roller thrust bearings of type 81212 are used for the classification test due to the high percentage of slippage between washer and roller. The bearing and the quantitative run of the sliding speed curve as well as the FE8 test rig setup are shown in Figure 1. The axial load can be applied dynamically and under different operating conditions during one test. More details about the test rig and the experimental procedure can be found in [20].
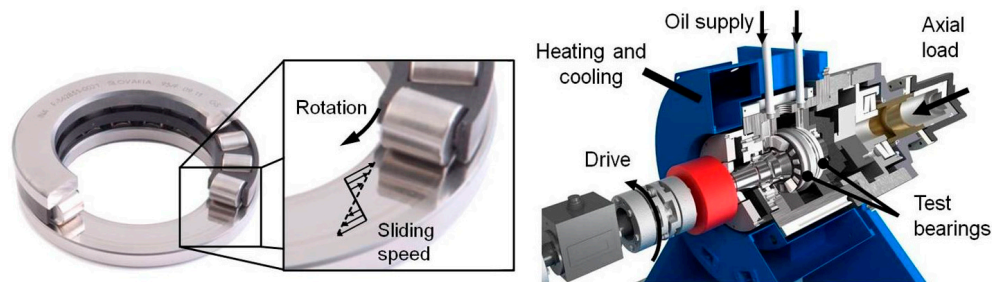
Figure 1. Cylindrical roller thrust bearing 81212 and modified FE8 test rig.

Figure 2 shows an overview of typical wear tracks recorded by optical light microscopy after having run the modified FE8 test for bearings for two hours and different rotational speeds (10, 15, and 20 rpm). Here, 10 rpm represents a lower limit for the tribolayer formation. At the given experimental conditions *i.e.*, load, temperature and additive concentration, no tribolayer will be built up below 10 rpm [20]. In the figure, the radial direction is from left to right (from inner to outer diameter). The differently colored regions (grey-for the substrate-brown-blue-yellow-blue-brown and grey again) can be clearly indentified along the radial direction for all tested rotational speeds.
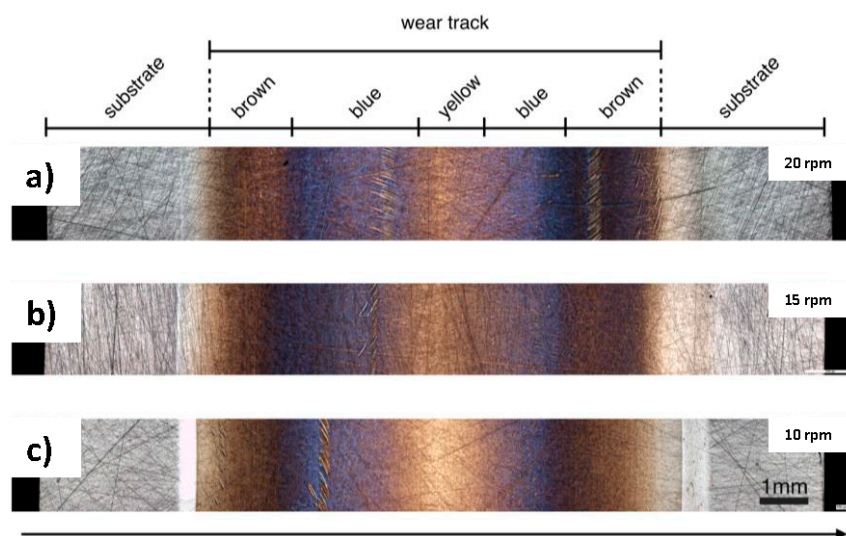
Figure 2. Overview of the wear track on the surface of the thrust ring, after FE8 test by applying a rotational speed of 20 rpm (**a**); 15 rpm (**b**) and finally 10 rpm (**c**) with an axial pressure load of 80 kN and working temperature of 60 °C.

Except the grey regions, which are considered substrate without wear, the other three colored regions which had intensive contact to the cylindrical rollers during the test are completely located in the wear track. The emerging bright bands at lower speeds are wear tracks with abrasive and adhesive

wear. Due to the highest sliding speeds at the sides of the wear track, this area is highly critical with respect to wear. The inner track is even more critical as the smallest rolling speed and consequently the highest ratio of solid body contact can be found in this part. Because of that, the wear track at the inner part is more pronounced (Figure 2c). The width of the roller (11 mm) exceeds the one of the wear track (~9 mm). The contact width between roller and washer is about 10–10.5 mm and includes the area of wear in Figure 2c.

The transition zones between different regions are quite diffuse and partially overlapping to some extent. With increasing rotational speed, the amounts of blue- and brown- colored regions are changed narrowing the yellow central part of the ring. For 20 rpm, the blue zone is more intense compared to lower rotational speeds. For that reason, the analysis of the layers in the following will be focused on that particular speed. By using a higher magnification (see Figure 3), the blue-film region appears more patchy like "islands" and not as a homogeneous layer. Additional topographical parameters such as root mean square roughness (rms) and peak to valley (PV) distance of the blue and brown films were obtained by white light interferometry from the inner and outer segments (see Table 2). The pristine arithmetic surface roughness of the steel substrate is R_a, steel ~0.2 µm. The roughness decreases with the formation of the tribolayers, partially covering the visible grinding marks of the substrate (see Figure 2). However, there is neither a tendency for the rms value nor the PV distance for the differently colored regions as a function of rotational speed as can be seen in Table 2. However, roughness generally plays an important role for the tribolayer formation in boundary lubricated contacts. Tribolayers usually form faster and require less energy input to be formed for a rough surface compared to a smooth surface [4].

Table 2. Parameters of FE8 test and root mean square roughness (rms) and peak to valley (PV) distance for the tribolayers. The arithmetic roughness R_a of the steel substrate is around 0.2 µm.

| Rotational Speed (rpm) | Load (kN) | Working Temp. (°C) | Blue-Film | | | | Brown-Film | | | |
| | | | Inner | | Outer | | Inner | | Outer | |
			Rms (nm)	PV (µm)	Rms (nm)	PV (µm)	Rms (nm)	PV (µm)	Rms (nm)	PV (µm)
10	80	60	31 ± 2.5	1.6 ± 1.0	30 ± 1.4	0.8 ± 0.2	66 ± 2.5	2.6 ± 0.2	47 ± 1.2	3.3 ± 0.7
15	80	60	40 ± 3.6	0.7 ± 0.1	47 ± 7.8	1.1 ± 0.6	42 ± 4.7	0.6 ± 0.1	42 ± 0.6	1.1 ± 0.9
20	80	60	41 ± 2.0	1.5 ± 0.8	42 ± 6.8	2.0 ± 0.8	58 ± 2.1	2.0 ± 0.2	53 ± 4.4	2.1 ± 0.2

Lubricant mineral oil mixed with ZDDP additive, C3C4-alkyl-chain with 0.05% P, 2 h sliding test.

Figure 3 displays the results of an EDS line-scan, which shows the distribution of typically occurring elements such as Zn, S, or P. In the figure, dots and triangles are used to represent the position of blue- and brown-colored regions. Along the scan-line, blue and brown film regions are mixed up thus complicating the analysis. Here, the content of Zn, P, and S rise while scanning through the blue-film region. On the other hand, in the brown-film region, only sulphur shows a slightly higher content.

Deeper information regarding the chemical bonding within the tribolayer was acquired with the help of Raman spectroscopy. In Figure 4, Raman spectra taken between 200 and 1500 cm^{-1} show the resonance peaks present at the yellow-, blue- and brown-colored regions, as well as the substrate. As a reference, the spectrum of the substrate showed the typical peaks to Cr-O and Fe-O, without revealing neither phosphates nor sulphides. In the yellow region, the spectrum mainly shows iron oxide (Fe_3O_4) at around 680 cm^{-1} and some sulphides. The Cr-O peaks (native oxide of the steel) of the substrate were not observed, presumably either due to the covering of this phase with other or a higher Raman activity of Fe_3O_4. Compared to the substrate, the blue and brown film regions display pronounced P-O, Fe-S, and Zn-S resonance peaks. The broad band at 1000 cm^{-1} is related to polyphosphates including three sub-peaks at 965, 1007, and 1045 cm^{-1} [17]. Additionally, the band at 386 cm^{-1} corresponds to FeS [21], whereas the peak at 351 cm^{-1} corresponds to ZnS [22]. Since Raman spectroscopy is a volume-sensitive technique, the analysis must be performed by comparing intensity

ratios. In this sense, a comparison of the blue and brown films is carried out by relating the intensities of the $(Zn_{0.88}Fe_{0.12})S_{1.00}$ band (351 cm^{-1}) [23] and the FeS band at 386 cm^{-1} (Figure 5). By comparing the intensity ratio of the aforementioned bands for both regions, it can be stated that this intensity ratio is higher for the blue film, indicating a higher $(Zn_{0.88}Fe_{0.12})S_{1.00}$ relative content. Furthermore, higher relative peak intensity for Fe_3O_4 is noticed for the brown-colored region, whereas no evident difference in the polyphosphate signal can be detected in the Raman spectra for both regions. This is a significant finding between the different colored regions, emphasizing that the color difference could be strongly attributed to the chemical composition instead of the layer thickness, as previously assumed in the literature [18].
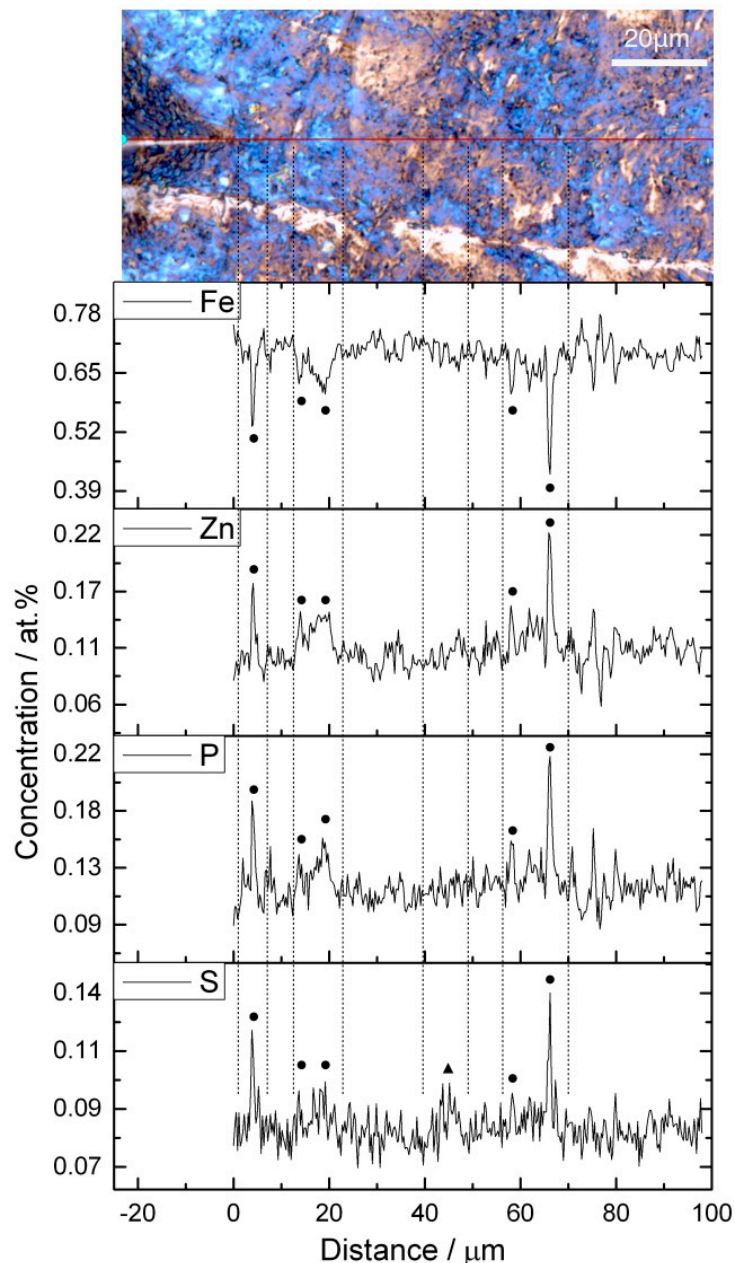
Figure 3. EDS line-scan through blue (dots) and brown film (triangle) regions at a rotational speed of 20 rpm.
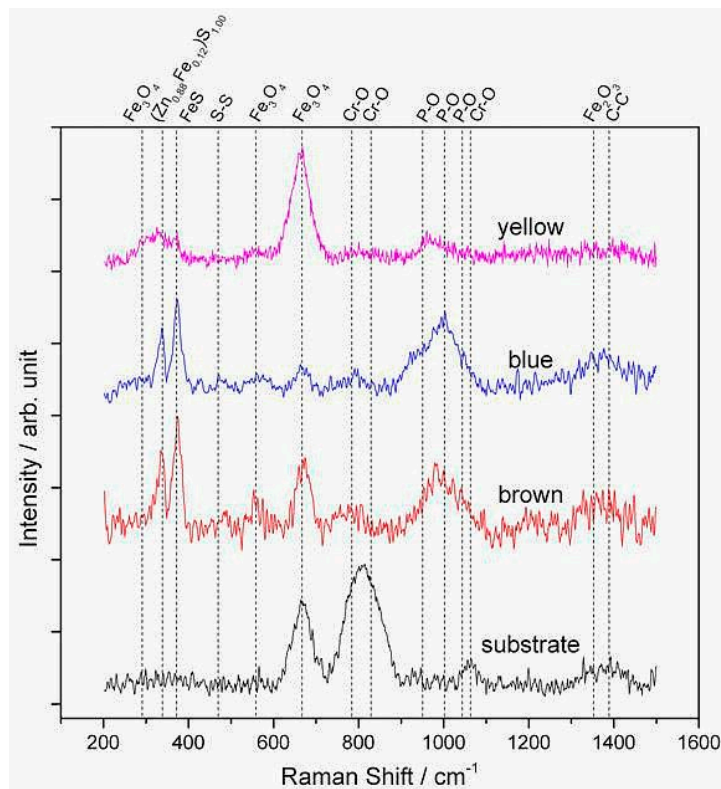
Figure 4. Raman spectra of anti-wear film at a fixed rotational speed of 20 rpm in the Raman shift range from 200 to 1500 cm^{-1}.
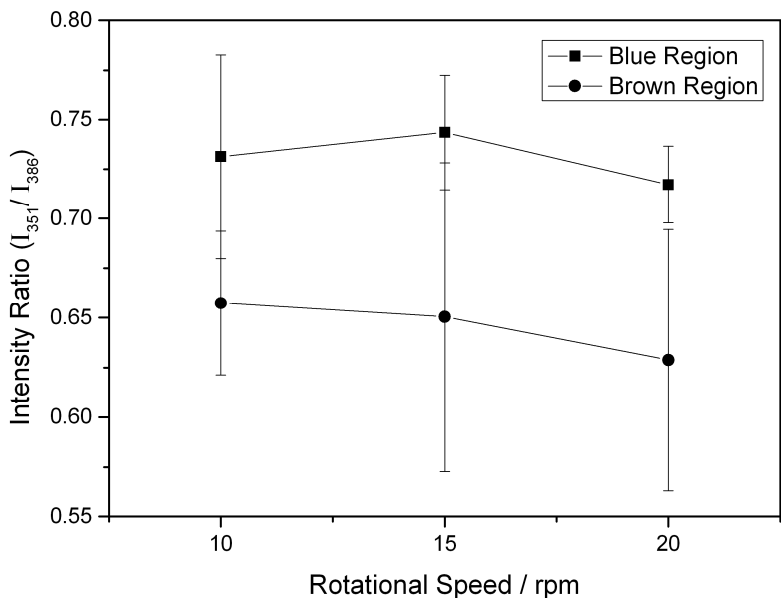
Figure 5. Intensity ratio of the peak attributed to $(Zn_{0.88}Fe_{0.12})S_{1.00}$ (351 cm^{-1}) over the peak of FeS (386 cm^{-1}), between Raman spectra of blue and brown film regions.

Figure 6a shows a bright-field electron micrograph of the analyzed zone. Four different regions are noticed being from top-right to bottom-left: Ion-deposited Pt protective layer, electron beam-deposited Pt protective layer, the respective tribolayer, the tribomutation layer and finally the steel substrate. The protective Pt layers are necessary for the FIB preparation in order to avoid damaging the region of interest. The bright tribolayer has a thickness between 70 and 140 nm and the deformed tribomutation

layer between 250 and 450 nm which is in a good agreement with values listed in literature [8]. The thickness mainly varies because of roughness differences and the subjected loading profile (see Figure 1 magnified insert) from the inner to outer ring segment. Selected area electron diffraction (SAED) was performed on two regions of interest (the tribolayer and the substrate) at 200 kV with a diffraction aperture of 180 nm. The diffraction pattern of the tribolayer (Figure 6b) resembles an amorphous structure, with some reflections from the substrate. This is an unavoidable feature, due to the aforementioned size of the diffraction aperture of 180 nm. The diffraction pattern of the substrate (Figure 6c) has been indexed and fully corresponds to ferrite (ICDD International Centre for Diffraction Data, PDF-2-file: 06-0696), being observed the main six reflections. The layered structure and the amorphous nature of the tribolayer fits well to the layer model proposed by Schmaltz and Bec *et al.* who describe the existence of a fine-crystalline and deformed tribomutation layer followed by a crystalline layer of sulphides and oxides and finally an amorphous tribolayer consisting of polyphosphates on top [8,24]. The crystalline layer of sulphides and oxides cannot be clearly identified in the TEM image. The typical thickness of this layer would be about 20 nm [24]. In contrast to that, the tribomutation layer is well pronounced due to the relatively high Hertzian contact pressure of around 1.92 GPa. Furthermore, chemical analysis was performed on the substrate and the blue film region by TEM-EDS due to its higher spatial resolution compared to conventional SEM-EDS (see Figure 7). In Figure 7a, the presence of distinct Zn, P, and S peaks is visible compared to the substrate spectrum.
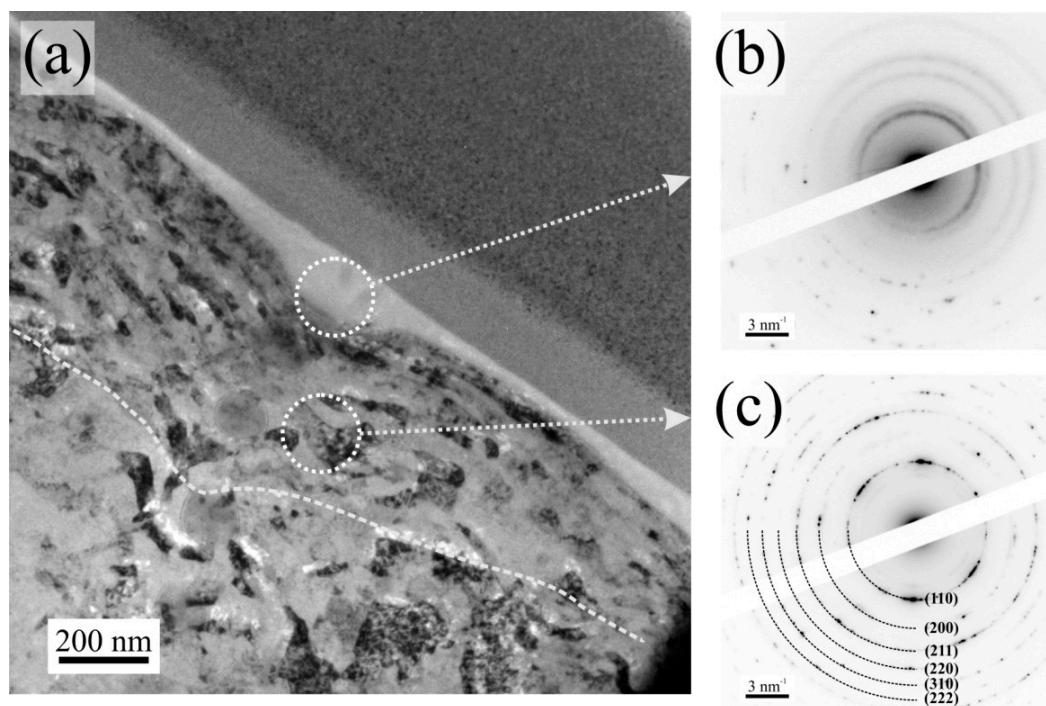

Figure 6. (**a**) Bright field TEM micrograph of the cross section of the wear track; (**b**) Electron diffraction pattern of the tribolayer; (**c**) Electron diffraction pattern of the substrate.
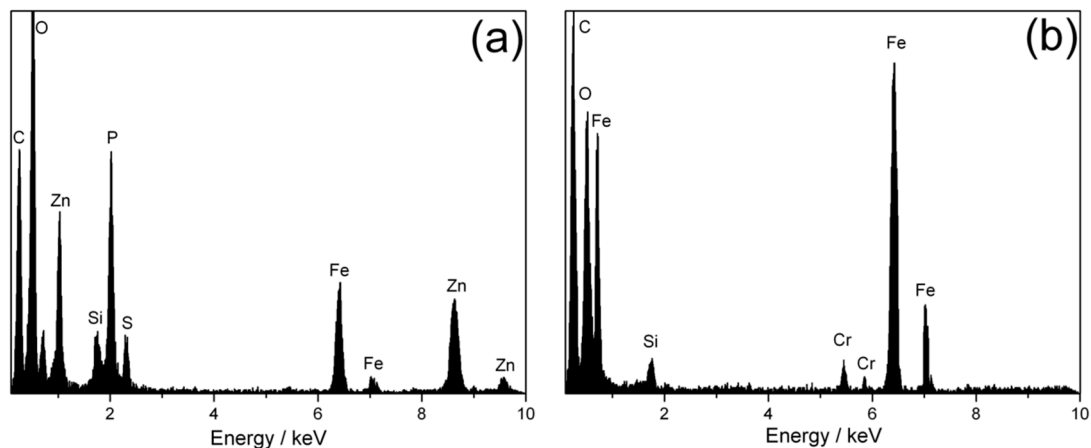
Figure 7. TEM-EDS spectra of blue-film region (**a**) and substrate (**b**).

The question regarding which film is more beneficial concerning the tribological performance cannot be answered in a straightforward manner. As soon as the colored tribolayers form (blue or brown), the bearings last until the end of the FE8 test without failing. The reaction pathways are still a matter of debate and the operating conditions provide a quite complex set of parameters with a difficult interplay between each other. By increasing the speed, more energy will be stored in the tribosystem and additionally the contact will be more effectively replenished with lubricant and so additive molecules thus facilitate the formation of potential wear resistant tribolayers. Mosey's MD simulations suggested a contact pressure induced cross-linking of zinc phosphate molecules [15]. According to Gosvami *et al.*, the nucleation and growth of tribolayers can be well described by a stress and thermally activated Arrhenius model. In this context, it is then assumed that the nucleation and growth are significantly influenced by surface heterogeneities, such as roughness, thus lowering the necessary activation energy for the tribolayer formation by varying contact areas and stresses [25]. On the other hand, a certain regeneration time between two rolling events is needed to allow for the formation of the layers [20]. With increasing speed, the time between two rolling events is shortened and therefore impeding the layer formation. It will be interesting to systematically elucidate the lower boundaries for the respective operating conditions under which a successful tribolayer can still be generated and to further reveal the reaction pathways of the tribolayers especially for highly loaded thrust bearings.

4. Conclusions

The tribolayer formation on the surface of highly loaded cylindrical roller thrust bearing rings at 1.92 GPa has been examined in a modified FE8 test for different rotational speeds. The resulting tribolayers were subsequently characterized by Raman spectroscopy, TEM, and TEM-EDS. The key findings of the research article may be summarized as follows.

- Below a rotational speed of 10 rpm no tribolayer was observed. Therefore, 10 rpm represents a lower boundary at the given operating conditions of 80 kN normal load and 60 °C temperature. With increasing speed, the amounts of blue- and brown-colored regions vary. The most intense blue color appearance could be found for 20 rpm. The blue layer is not homogeneous but patchy as reported in literature.
- Raman spectroscopy could prove that the blue-layers are enriched with ZnS and FeS whereas the brown layers are characterized by a larger amount of Fe_3O_4. As far as polyphosphates are concerned, no distinct differences could be found for both colored layers in the respective Raman spectra. This experimental finding reveals that the color appearance may be due to chemical composition and not only because of thickness effects. The question regarding the performance

differences of the blue- and brown-colored regions cannot be answered within this research work and will be part of a follow-up paper.

- Microstructural studies by TEM verified the layered morphology with a 250–450 nm thick deformed tribomutation layer followed by 70–140 nm thick amorphous tribolayer with clear signatures of Zn, P, and S based upon TEM-EDS measurements.

Author Contributions: Carsten Gachot wrote the article and analyzed the overall data. Chia Jui Hsu designed the experiments for optical microscopy and analyzed Raman data. Sebastián Suárez performed TEM experiments and analyzed data. Philipp Grützmacher performed Raman experiments and provided discussion on gained results. Andreas Rosenkranz analyzed EDS data and wrote experimental part. Andreas Stratmann designed the test rig, provided specimens and analyzed data for color formation depending on experimental conditions. Georg Jacobs supervised work, discussed the basic design of experiments with Andreas Stratmann and Carsten Gachot, provided suggestions for final discussion of data.

Conflicts of Interest: The authors declare no conflict of interest.

References

1. Spikes, H. The history and mechanisms of ZDDP. *Tribol. Lett.* **2004**, *17*, 469–489. [CrossRef]
2. Varlot, K.M.; Kasrai, M.; Martin, J.M.; Vacher, B.; Bancroft, G.M.; Yamaguchi, E.S.; Ryason, P.R. Antiwear film formation of neutral and basic ZDDP: Influence of the reaction temperature and of the concentration. *Tribol. Lett.* **2000**, *8*, 9–16. [CrossRef]
3. Spikes, H. Friction modifier additives. *Tribol. Lett.* **2015**, *60*, 1–26. [CrossRef]
4. Kubiak, K.J.; Mathia, T.G.; Bigerelle, M. Influence of roughness on ZDDP tribofilm formation in boundary lubricated fretting. *Tribol. Mater. Surf. Interfaces* **2012**, *6*, 182–188. [CrossRef]
5. International Lubricant Standardization and Approval Committee. *ILSAC GF-5 Standard for Passenger Car Engine Oils*; US/Europe/Japan, 2009.
6. Fujita, H.; Spikes, H.A. The formation of zinc dithiophosphate antiwear films. *J. Eng. Tribol.* **2004**, *218*, 265–278. [CrossRef]
7. Bancroft, G.M.; Kasrai, M.; Fuller, M.; Yin, Z.; Fyfe, K.; Tan, K.H. Mechanisms of tribochemical film formation: Stability of tribo and thermally generated ZDDP films. *Tribol. Lett.* **1997**, *3*, 47–51. [CrossRef]
8. Schmaltz, G. *Technische Oberflächenkunde*; Verlag von Julius Springer: Berlin, Germany, 1936.
9. Martin, J.M. Antiwear mechanisms of zinc dithiophosphate: A chemical hardness approach. *Tribol. Lett.* **1999**, *6*, 1–8. [CrossRef]
10. Martin, J.M.; Mansot, J.L.; Berbezier, I.; Dexpert, H. The nature and origin of wear particles from boundary lubrication with a zinc dialkyl dithiophosphate. *Wear* **1984**, *93*, 117–126. [CrossRef]
11. Martin, J.M.; Belin, M.; Mansot, J.L.; Dexpert, H.; Lagarde, P. Friction induced amorphization with ZDDP—an EXAFS study. *ASLE Trans.* **1986**, *29*, 523–531. [CrossRef]
12. Martin, J.M.; Mansot, J.L.; Berbezier, I.; Belin, M.; Balossier, G. Microstructural aspects of lubricated mild wear with zinc dialkyldithiophosphate. *Wear* **1986**, *107*, 355–366. [CrossRef]
13. Belin, M.J.; Martin, J. L.; Martin, J.M.; Mansot, J.L. Role of iron in the amorphization process in friction-induced phosphate glasses. *Tribol. Trans.* **1989**, *32*, 410–413. [CrossRef]
14. Onodera, T.; Martin, J.M.; Minfray, C.; Dassenoy, F.; Miyamoto, A. Antiwear chemistry of ZDDP: Coupling classical MD and tight-binding quantum chemical MD methods (TB-QCMD). *Tribol. Lett.* **2013**, *50*, 31–39. [CrossRef]
15. Mosey, N.J.; Woo, T.K.; Kasrai, M.; Norton, P.R.; Bancroft, G.M.; Müser, M.H. Interpretation of experiments on ZDDP anti-wear films through pressure-induced cross-linking. *Tribol. Lett.* **2006**, *24*, 105–114. [CrossRef]
16. Gauvin, M.; Minfray, C.; Belin, M.; Aquilanti, G.; Martin, J.M.; Dassenoy, F. Pressure-induced amorphization of zinc orthophosphate—Insight in the zinc coordination by XAS. *Tribol. Int.* **2013**, *67*, 222–228. [CrossRef]
17. Berkani, S.; Dassenoy, F.; Minfray, C.; Martin, J.M.; Cardon, H.; Montagnac, G.; Reynard, B. Structural changes in tribo-stressed zinc polyphosphates. *Tribol. Lett.* **2013**, *51*, 489–498. [CrossRef]

18. Hsu, S.M. Boundary lubrication of materials. *MRS Bull.* **1991**, *16*, 54–58.

19. DIN 51819-3. *Testing of Lubricants-Mechanical Dynamic Testing in the Roller Bearing Test Apparatus FE8—Part 3: Test Method for Lubricating Oils, Axial Cylindrical Roller Bearing*; 2005.

20. Stratmann, A. Formation of anti-wear films in rolling bearings due to run-in procedures. In Proceedings of the WTC 2013, Torino, Italy, 8 September 2013.

21. Ushioda, S. Raman scattering from phonons in iron pyrite (FeS$_2$). *Solid State Commun.* **1972**, *10*, 307–310. [CrossRef]

22. Brafman, O.; Mitra, S.S. Raman effect in wurtzite-and zinc-blende-type ZnS single crystals. *Phys. Rev.* **1968**, *171*, 931. [CrossRef]

23. Integrated Database for Raman Spectra, XRD and Chemistry Data of Minerals. Available online: http://www.rruff.info (accessed on 15 March 2016).

24. Bec, S.A.; Tonck, A.; Georges, J.M.; Coy, R.C.; Bell, J.C.; Roper, G.W. Relationship between mechanical properties and structures of zinc dithiophosphate anti-wear films. *Proc. R Soc. Lond. A Math. Phys. Eng. Sci.* **1999**, *455*, 4181–4203. [CrossRef]

25. Gosvami, N.N.; Bares, J.A.; Mangolini, F.; Konicek, A.R.; Yablon, D.G.; Carpick, R.W. Mechanisms of antiwear tribofilm growth revealed *in situ* by single-asperity sliding contacts. *Science* **2015**, *348*, 102–106. [CrossRef] [PubMed]

9. PAPER I

Dissertation, Chia-Jui HSU

10. PAPER II

Title:

Revealing the Interface Nature of ZDDP Tribofilm by X-ray Photoelectron Spectroscopy and Atom Probe Tomography

Authors:

Chia-Jui Hsu[1,2,*], Jenifer Barrirero[1], Rolf Merz[3], Andreas Stratmann[4], Hisham Aboulfadl[5], Georg Jacobs[4], Michael Kopnarski[3], Frank Mücklich[1], Carsten Gachot[2]

[1] Department of Material Science and Engineering, Saarland University, Saarbrücken, Germany

[2] Institute of Engineering Design and Product Development, Vienna University of Technology, Vienna, Austria

[3] Institute for Surface and Thin Film Analysis IFOS GmbH, Kaiserslautern, Germany

[4] Institute for Machine Elements and Machine Design, RWTH Aachen University, Aachen, Germany

[5] Department of Physics, Chalmers University of Technology, Gothenburg, Sweden

Owned contributions: Experiments design; data analyses; paper writing.

10. PAPER II

Dissertation, Chia-Jui HSU

Revealing the interface nature of ZDDP tribofilm by X-ray photoelectron spectroscopy and atom probe tomography

Chia-Jui Hsu
Institute of Engineering Design and Product Development, Vienna University of Technology, Vienna, Austria

Jenifer Barrirero
Department of Materials Science, Saarland University, Saarbrücken, Germany

Rolf Merz
Institute for Surface and Thin Film Analysis IFOS GmbH, Kaiserslautern, Germany

Andreas Stratmann
Institute for Machine Elements and Systems Engineering, RWTH Aachen University, Aachen, Germany

Hisham Aboulfadl
Department of Physics, Chalmers University of Technology, Gothenburg, Sweden

Georg Jacobs
Institute for Machine Elements and Systems Engineering, RWTH Aachen University, Aachen, Germany

Michael Kopnarski
Institute for Surface and Thin Film Analysis IFOS GmbH, Kaiserslautern, Germany

Frank Mücklich
Department of Materials Science, Saarland University, Saarbrücken, Germany, and

Carsten Gachot
Institute of Engineering Design and Product Development, Vienna University of Technology, Vienna, Austria

Abstract

Purpose – To decrease wear and friction, zinc dialkyldithiophosphate (ZDDP) has been used in engine oil for several decades, but the mechanism of the tribofilm formation is still unclear. The purpose of this study is to characterize the chemical details of the tribofilm by using high-resolution approaching.

Design/methodology/approach – An ISO VG 100 mineral oil mixed with ZDDP was used in sliding tests on cylindrical roller bearings. Tribofilm formation was observed after 2 h of the sliding test. X-ray photoelectron spectroscopy (XPS) and atom probe tomography (APT) were used for chemical analysis of the tribofilm.

Findings – The results show that the ZDDP tribofilm consists of the common ZDDP elements along with iron oxides. A considerable amount of zinc and a small amount of sulfur were observed. In particular, an oxide interlayer with sulfur enrichment was revealed by APT between the tribofilm and the steel substrate. The depth profile of the chemical composition was obtained, and a tribofilm of approximately 40 nm thickness was identified by XPS.

Originality/value – A sulfur enrichment at the interface is observed by APT, which is beneath an oxygen enrichment. The clear evidence of the S interlayer confirms the hard and soft acids and bases principle.

Peer review – The peer review history for this article is available at: https://publons.com/publon/10.1108/ILT-01-2020-0035/

Keywords ZDDP, Boundary lubrication, Atom probe tomography, Roller bearing, Tribochemistry

Paper type Research paper

The current issue and full text archive of this journal is available on Emerald Insight at: **https://www.emerald.com/insight/0036-8792.htm**

1. Introduction

Zinc dialkyldithiophosphate (ZDDP) is a multi-functional additive that has been widely used for formulating lubricants because of its excellent performance and relatively low cost (Spikes, 2004). The addition of ZDDP contributes to the formation of an anti-wear tribofilm, which prevents direct contact between two surfaces acting a role of a barrier. The tribofilm also has the capability of capturing harmful hard particles such as iron oxide, thus reducing the wear of the sliding surfaces (Minfray et al., 2004b; Onodera et al., 2008). The tribofilm is present as solid-like pads formed in the contact area that is commonly described as blue-colored tribofilm (Kubiak et al., 2012; Onodera et al., 2013; Gachot et al., 2016). It is generally accepted that the presence of a ZDDP tribofilm is correlated with the reduction of wear and friction. ZDDP was used in various applications because of its benefits in tribological performance. However, the usage of ZDDP in engine oil is now facing restrictions, as the phosphorous and sulfur oxides reduce the effective life of exhaust catalysts (Spikes, 2004). To find a proper substitute, several open questions have to be answered.

The formation of ZDDP tribofilm is a complex mechanism induced by thermal activation and tribomechanical reactions (i.e. shearing) (Fujita and Spikes, 2004; Fuller et al., 1997). Shear-induced tribofilms showed a better stability and wear-resistance, according to Bancroft et al. (Bancroft et al., 1997). Based on molecular dynamics simulations, it is suggested that the pressure/shear-induced cross-linking is the key mechanism in the formation of anti-wear films (Mosey et al., 2005). In addition, the driving force of the tribochemical reaction of ZDDP is not directly attributed to the temperature but to the entropy mixing contribution (Martin et al., 2012). Gosvami et al. (Gosvami et al., 2015) proved by using *in-situ* sliding tests with atomic force microscopy that the formation of the tribofilm is a thermally activated and stress-assisted reaction. Furthermore, it is suggested that nano-crystallization within the material caused by the sliding process enhanced the tribofilm formation.

The composition of the main part of tribofilm, namely, the bulk tribofilm, is based on the ZDDP related elements, such as Zn, P and S. Longer chain of zinc/iron polyphosphates were found at the top of the tribofilm; whereas lower chain at the bottom region (Spikes, 2004). Various methods have been applied to reveal the chemical detail of the ZDDP tribolayer, such as Raman spectroscopy (Berkani et al., 2013), time of flight secondary ion mass spectrometry (Minfray et al., 2004a), auger electron spectroscopy (Martin et al., 2000) and X-ray absorption near edge structure (XANES) (Nicholls et al., 2003). The morphology of the tribofilm can be described as island-like pads, which consists mainly of glassy phosphates (Martin et al., 2001).

A high concentration of oxygen was commonly found in the bulk tribofilm caused by the sliding motion. Martin et al. (2001) observed a considerable amount of oxygen in the tribolayer and approximately 4 per cent of sulfur in the top of the bulk tribofilm. Miranda-Medina et al. (Miranda-Medina et al., 2019) indicated iron oxide particles captured by the tribolayer in a cross-section observation. Hence, Guo et al. (2017) identified a clear iron oxide layer at the bottom of the tribofilm, which revealed that there is an oxygen enrichment at the interface between the bulk tribofilm and the steel substrate.

In addition to oxygen, sulfur has also been identified in the tribofilm; however, it is still unclear whether there is an enrichment at the interface. Based on the hard and soft acids and bases (HSAB) principle, the chemical reaction between sulfur and nascent steel substrate has been proposed as an initial step of film formation (Martin, 1999). Bell et al. (1992), Smith and Bell (1999) found an enrichment of S/O at the interface with about 5-10 per cent of sulfur content. Some recent works present the existence of the sulfur-enriched layer differently by various methods, Shimizu and Spikes (2016) found the enrichment of S at the initial state of sliding, but it was afterward pushed to the edge of the contact zone and transformed to be P- and Zn-enriched. Soltanahmadi et al. (2017) have made the sulfide interlayer visualized by using transmission electron microscopy (TEM)/energy dispersive X-ray spectroscopy (EDS). Moreover, X-ray photoelectron spectroscopy (XPS) identified a sulfur/oxygen enrichment at the bottom side of the bulk tribofilm (Heuberger et al., 2007; Dorgham et al., 2018). However, there are some studies claimed that no sulfur interlayer was identified (Martin, 1999; Martin et al., 2001; Zhou et al., 2017). According to the literature mentioned above, the S enrichment at the interface is still ambiguous. The thinness and the mixture of oxygen and sulfur increase the difficulty of identifying the interface nature of the tribofilm.

Atom probe tomography (APT) is a high-resolution analytical technique, which provides three-dimensional (3D) chemical compositional analysis at the nanometer scale (Kelly and Miller, 2007; Miller and Forbes, 2009). The chemical sensitivity limit of APT is around 10 ppm, and it is accordingly an ideal tool to reveal quantitative chemical information of segregation and near interfaces. The spatial resolution limit of this technique is approximately 0.1 nm in z-direction (depth) and 0.2 nm in xy-directions (lateral), which takes a longer time for the sample preparation, but gives a prominent three-dimensional representation of the elemental distribution at high-resolution. So far, there are only a few APT studies aiming at tribofilms. Kim et al. (2016) applied APT to prove the little content of boron in the tribofilm formed by boron added lubricants. Guo et al. (2017), Zhou et al. (2017) identified the existence of an iron oxide interlayer, but no sulfur enrichment was found. Therefore, APT was used in this study to examine the interface region between the ZDDP tribofilm and the steel substrate.

2. Experiments

2.1 Zinc dialkyldithiophosphate tribofilm formation

Tribofilm was formed after a tribological sliding test operated by a modified FE8 test rig according to DIN 51819-3. Cylindrical roller thrust bearings (Type 81212) comprised of two washers, a cage, and 15 cylindrical rollers made of 100Cr6 bearing steel (AISI 52100) were tested in lubricated conditions. The bearings were installed in the vertical plane, i.e. with a horizontal axis of rotation. The test was run with a rotational speed of 20 rpm and an axial load of 80 kN for 2 h. A mineral oil of class ISO VG 100 was used as a base oil and mixed with a secondary ZDDP additive in a concentration of 0.02 Wt.% of

phosphorous. Sufficient lubricant was fed to the contact area by a pumping system. The working temperature was 80°C. The maximum contact pressure according to Hertzian calculation was 1.92 GPa. More experimental details can be found in Table 1. In addition, the minimum oil film thickness was estimated according to the Dowson-Higginson equation (Dowson *et al.*, 1962) as boundary lubrication. After the sliding test, the surface was cleaned by benzene and isopropanol to remove the residual lubricant, abrasives and contaminants.

2.2 X-ray photoelectron spectroscopy

The depth profile of the tribofilm was examined by XPS. The instrument is equipped with a monochromatic Al Kα (1486.6 eV) source based on a 500 mm circle geometry, a delay-line detector (DLD), a 165 mm mean radius hemispherical analyzer plus spherical mirror analyzer (SMA) for parallel chemical imaging and runs under ultra-high vacuum conditions with a working pressure below 10^{-8} mbar in the main chamber. The spectrometer was used in small spot spectroscopy mode, where the virtual probe on the surface of the samples is defined by choosing a suited aperture inside the electrostatic column of the detector. The place of measurement was set to a size of 0.3 x 0.7 mm, matching the tribofilm regions within the wear track. Congruence of the region of interest and place of measurement was controlled by parallel chemical imaging. The chemical composition of the surface of the sample was analyzed by XPS survey spectra with a typical information depth of less than 5 nm. Elemental concentrations in atomic percentages for the detected elements were calculated from the peak areas of photoelectron lines. Depth information of the tribofilm was obtained by XPS sputter profiles. All ZDDP tribofilm related elements including zinc, phosphorus, sulfur, oxygen and iron were considered. For sputter etching, the standard Argon ion gun was used with a raster size of 2 x 2 mm and an ion energy of 2 keV. The depth scale is given in regard to a Ta_2O_5 reference sample, which would be sputtered up to this deep with the same adjustments of the ion gun.

2.3 Atom probe tomography

Sample preparation for APT was processed in a dual beam scanning electron microscope/focused ion beam workstation (SEM/FIB). A 200 nm Cr sacrificial capping layer was deposited above the ZDDP tribofilm by physical vapor deposition (PVD). The specimens were prepared by the lift-out technique described in (Thompson *et al.*, 2007). The last step of low energy milling at 2 kV was performed to minimize Ga induced damage. Laser pulsed APT measurements were performed at a repetition rate of 100 kHz, specimen temperature of about 60 K, a pressure lower than $1 \times 10 - 10$ Torr (1.33×10^{-8} Pa) and a laser pulse energy of 0.7 nJ. The evaporation rate was set to 2 atoms per 1,000 pulses. Data sets were reconstructed and analyzed by a computational analysis software.

3. Results and discussions

A ZDDP anti-wear tribofilm was formed at the contact area after 2 h of the sliding test. The surface overview of the bearing washer obtained by optical microscopy is shown in Figure 1(a) and (b). In the wear track area, a tribofilm with brown and blue coloration was found along the wear track. The correlation between the Slide-Roll Ratio (SRR) and the thickness of the tribofilm on roller bearings has been presented previously (Stratmann *et al.*, 2017). By means of the formation of the anti-wear tribofilm, no severe wear damage was observed. The presence of the ZDDP tribofilm enhances the tribological performance and prolongs the lifetime of the thrust bearings (Hsu *et al.*, 2017; Rosenkranz *et al.*, 2016). Furthermore, it has been proven by Gachot *et al.* (2016) that the blue regions are enriched in phosphates, whereas the brown-colored film fractions show significant amounts of iron oxides. As a consequence, the blue region at SRR +7 per cent was selected for further investigation by XPS and APT. In addition, the cross-section profile obtained by SEM is shown in Figure 2. The thickness of the tribofilm is up to a maximum of 80 nm. It can be observed that the average thickness is around 40 nm. The inhomogeneity of the tribofilm can be attributed to the complex tribochemical reaction, which is in good agreement with the literature (Kalin, 2004; Topolovec-Miklozic *et al.*, 2007).

XPS analysis presents the chemical composition of the ZDDP tribofilm at its surface and by sputtering along with the depth. In Figure 3(a), the depth profile shows the concentration of the elements identified, and Figure 3(b) shows the concentration profile of the uppermost 100 nm. According to the depth profile, the tribofilm was approximately 40 nm in thickness. The tribofilm was composed of the ZDDP related elements, including 11 Wt.% of P, 2 Wt.% of S and 24 Wt.% of Zn; meanwhile around 50 Wt.% of oxygen was found. The analysis reveals a considerable amount of oxygen in the tribofilm, which could be composed of the products of the decomposition of ZDDP itself, iron oxides from the wear debris, or even caused by the exposure to ambient air after testing. In addition, iron has been detected in the tribofilm. This can be attributed either to the diffusion of Fe from the iron-based substrate, or to the deposition of wear debris (Martin, 1999; Martin *et al.*, 2001). For further examination into the interface, the tribofilm was cut and shaped into the form of a tip by SEM/FIB lift-out process. An SEM image of an APT tip specimen from the respective sample is shown in Figure 1(c).

APT atom maps are shown in Figure 4. The data set shows the spatial distribution of the elements in the specimen, including the Cr capping layer, anti-wear tribofilm and steel substrate (Figure 4(a)). Figure 4(b) shows the spatial distribution of single ions as well as some complex ions. The Cr capping layer can be observed at the top of the specimen, whereas the tribofilm and its related elements such as P, S, Zn and O are dominant in the region below. Fe atoms are located mainly beneath the region of tribofilm (steel substrate) but also

Table 1. Lubricant properties and lubrication conditions for tribofilm growth in sliding test

	Oil properties at 80°C		Sliding and lubrication condition		
Kinematic Viscosity	Density	Pressure-viscosity coefficient	Rolling speed	Max. pressure	Temp.
18.4 mm²/s	856.9 kg/m³	1.59 x 10⁻⁸ Pa⁻¹	0.04 m/s	1.92 GPa	80°C

Figure 1 General view of the sample preparation
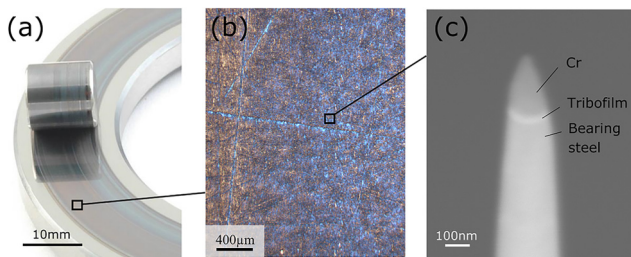
Notes: (a) Overview of the wear track on the surface of thrust ring with a cylindrical roller; (b) the ZDDP tribofilm in the wear track obtained by optic microscopy; (c) the shaped tip specimen of the tribofilm for APT analysis

Figure 2 STEM image showing the cross-section of the tribofilm in the wear track. From top to bottom are Pt protective layer, ZDDP tribofilm and Fe substrate
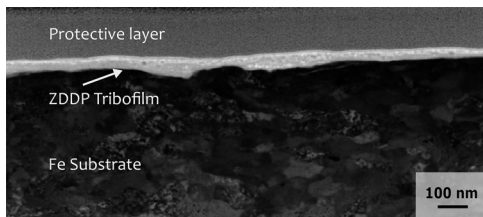

Figure 3 (a) Chemical composition profile of the ZDDP tribofilm by XPS, sputtering from the top of the film to the steel substrate and (b) a concentration profile for the uppermost 100 nm
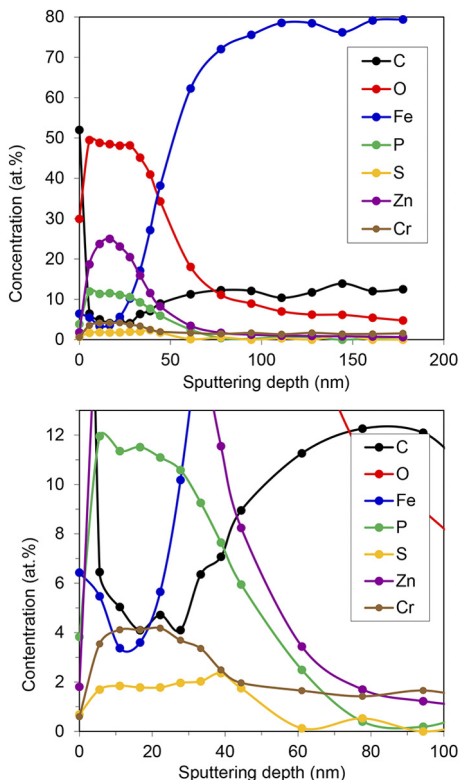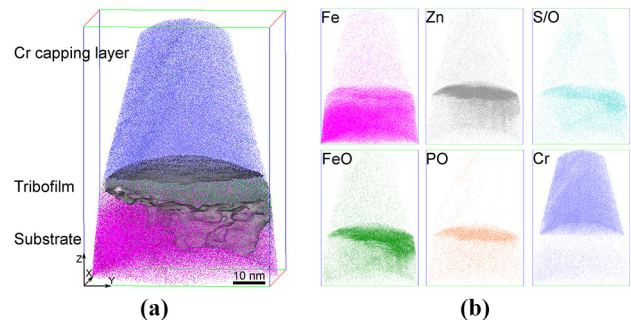

Figure 4 (a) 3 D APT reconstruction showing the Cr capping layer, ZDDP tribofilm and steel substrate. A 5 Wt.% of Zn iso-concentration surface (grey) is used to delimitate the tribofilm and (b) spatial distribution of Fe, Zn, S/O, FeO, PO and Cr atoms in the reconstruction

found in the tribofilm. Several peak-overlaps exist in the APT mass-to-charge-state ratio spectrum such as Zn^{2+} (m/n = 32-35) with SiO_2^{2+} (m/n = 30-33), FeO^{2+} (m/n = 35-38) and CrO^{2+} (m/n = 33-36). Furthermore, the overlap in the mass spectrum between O^{+1} and S^{+2} at m/n = 16 and between O_2^{+1} and S^{+1} at m/n = 32, makes it difficult to differentiate these elements in the spatial maps clearly. A peak decomposition algorithm was used to correct the overlaps based on the natural isotopic abundance (Gault *et al.*, 2012).

Table 2 shows the average composition of the tribofilm measured by APT. The tribofilm was delimited by a 5 Wt.% of Zn iso-concentration surface [Figure 4(a)], and the composition was calculated considering the atoms inside this volume. The compositions of the Cr-capping layer and the steel substrate are therefore excluded from such analysis. The results show that the tribofilm was composed of approximately 26 Wt.% of Zn and approximately 3 Wt.% of S, which is similar to the results of XPS. On the contrary, a higher amount of Fe and a lower amount of O and P were identified. The differences between these two methods could be attributed to the inhomogeneity of the tribofilm, which was also found in the previous study by TEM (Gachot *et al.*, 2016). Additionally, APT analysis required high-level cleanliness of sample preparation. The organic phosphate layer could have been partially removed by solvent cleaning before APT sample preparation (Smith and Bell, 1999). However, the interlayer covered by the inorganic layer was fully conserved. A clear insight into the interface between the tribofilm and the substrate was then obtained.

**Table 2.** Chemical composition of the tribofilm measured by APT, calculated from within a volume enclosed by iso-concentration surfaces of 5 Wt.% Zn

	Composition Wt.%		
Zn	25.74	±	0.08
P	0.73	±	0.01
S	2.79	±	0.02
O	15.08	±	0.01
Cr	3.98	±	0.03
Fe	48.33	±	0.09
C	0.61	±	0.01

In Figure 5, two-dimensional (2D) contour plots highlight the elemental distributions and compositions within two mutually perpendicular 5 nm thick slices through the APT data set at the tribofilm, namely, *x-z* and *y-z* planes [correlated to Figure 4 (a)]. From top to bottom, Zn enrichment at the upper part of the tribofilm is presented in Figure 5(a) and (b), and the enrichment of FeO underneath the Zn-rich region is shown in Figure 5(c) and (d). Finally, enrichment of S/O at the bottom of the substrate is shown in Figure 5(e) and (f). The disambiguation between S and O was done by the FeS complex ion peaks, showing the presence of S in the lowest part of the tribofilm [Figure 5(g) and (h)].

At the upper part of the tribofilm, a higher amount of Zn was found, which was mixed with iron and oxygen. The composition of the tribofilm shows the participation of ZDDP elements, which can be attributed to the aforementioned shearing influence by sliding. Moreover, an iron oxide layer was formed beneath the Zn-rich area, which can be attributed to the entrapment of wear debris. The observation of the oxygen enrichment is in good agreement with the literature, which suggested that the shearing causes the oxidation of the surface and the tribofilm (Zhang *et al.*, 2005). Wear particles removed from the steel surface by mechanical motion were first carried into the lubricant; the particles would then be embedded into

Figure 5 Two-dimensional (2 D) contour plots showing the elemental distribution and composition profiles at two mutually perpendicular slices through the tribofilm (*x-z* and *y-z* planes)
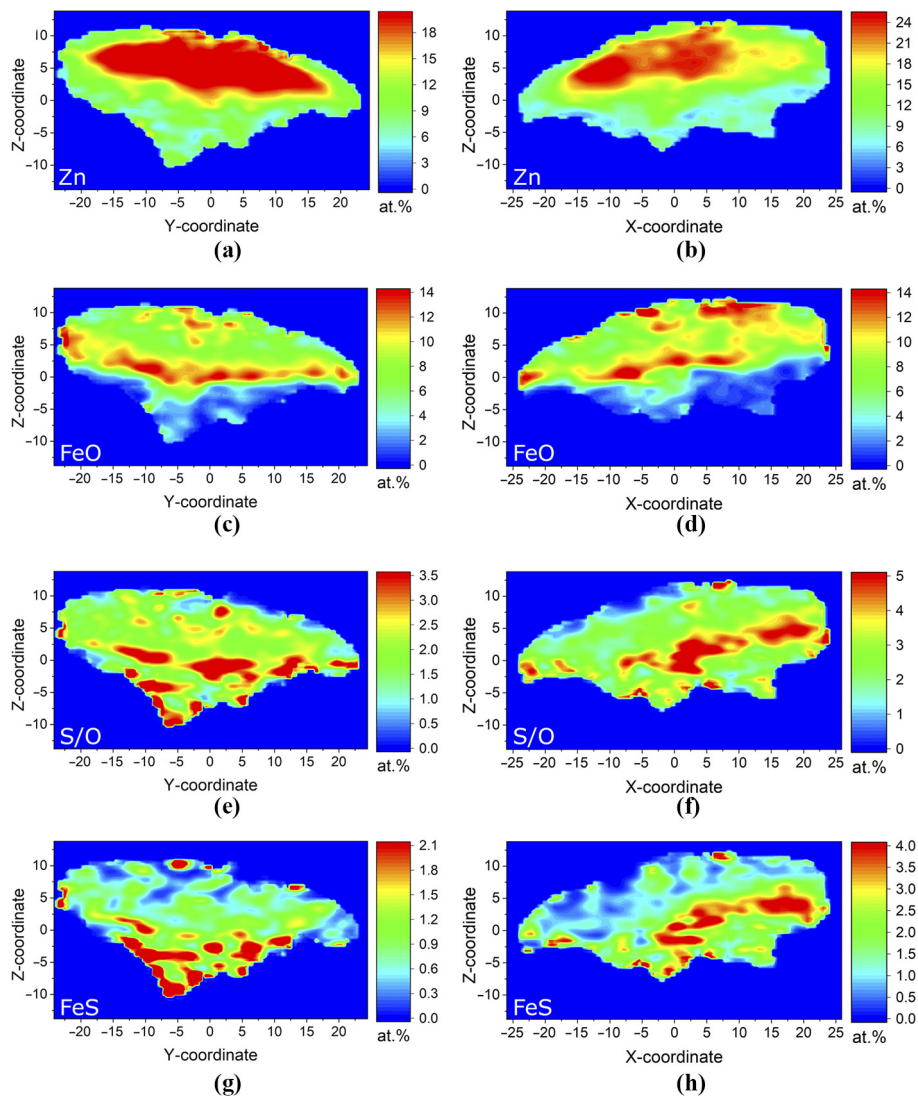
Notes: (a,b) Zn enrichment at the upper part of the tribofilm; (c,d) enrichment of FeO underneath the Zn rich region; (e,f) enrichment of S/O on the substrate. The overlap in the mass spectrum between O+1 and S+2 at m/n = 16 makes it difficult to clearly differentiate the e elements. the presence of S on the substrate is then confirmed by the separate plot of the distribution and concentration of FeS in the film (g,h)

the tribofilm because of the "digestion" mechanism (Martin, 1999; Minfray *et al.*, 2006; Spikes, 2004).

The specific observation of the sulfur enrichment by APT dedicates to understanding the structure of the ZDDP tribofilm. According to the HSAB principle, a thin sulfur layer (FeS) would be formed at the nascent steel surface by following the soft reaction, which happens at the beginning of sliding tests (Martin, 1999). Although some aforementioned studies found no S enrichment at the interface, the present study supports its existence with a high-resolution insight. By separating the mass-to-charge peaks based on the abundance of isotopes, the correlation between the distribution of sulfur and oxygen was distinguished.

A hypothetical construction of the ZDDP anti-wear tribofilm is illustrated in Figure 6 based on the observation from XPS and APT. The construction of the tribofilm is generally corresponding to the Schmaltz model (Schmaltz, 1936). From top to bottom, it comprises a tribofilm, an oxide interlayer, a sulfur enrichment and the steel substrate. Zinc dominated in the tribofilm and mixed with a considerable amount of iron and oxide. Beneath the tribofilm, an oxide interlayer and a sulfur enrichment at the bottom appeared. The oxide layer was attributed to the mixture of oxides, which mainly came from wear debris because of the severe sliding conditions. Furthermore, the sulfur enrichment was formed by the tribochemical reaction that nascent iron surfaces react with sulfur species (De Barros *et al.*, 2003).

Two different methods, XPS and APT, were both used for chemical analyses. In this study, XPS is used as a kind of fast preparatory screening technique for APT analysis. Regarding the complex load situation of macroscopic technical samples and its roughness, the tribofilm formation is understood to be inhomogeneous, at least on a micro-scale. The XPS depth profiles cover a representative area of the tribofilm and give a first impression of the chemistry concerning the average depth distribution of its components. Based on these results, including STEM lamella, the best-suited sites for APT analysis, with a high probability of matching locally pronounced tribolayer and the relevant depth scale, could be selected. In the next step, the introduction of APT revealed the tribofilm at the nanometer scale that provided further details of the tribofilm composition, which would be difficult to obtain by using other analytical techniques. Consequently, adequate preliminary examinations should be manipulated prior to running in an APT experiment in future studies for a better insight of characterization (Kelly *et al.*, 2007).

Figure 6 Schematic representation of the ZDDP anti-wear tribofilm. From top to bottom are Fe/Zn polyphosphate tribofilm (10-100 nm), oxide layer ($\cong$ 10 nm), sulfur enrichment ($\cong$ 5 nm) and steel substrate. The sulfur enrichment is shown to be unevenly distributed according to the findings by APT (Figure 5)
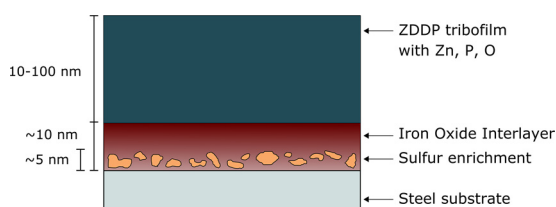
4. Conclusions

In the present study, ZDDP anti-wear tribofilms formed on the surface of a cylindrical roller thrust bearing have been analyzed by XPS and APT. The chemical composition and constituents of the tribofilm are revealed. The findings show:

- Analysis from both the XPS and APT demonstrate a well-established tribofilm formed under high pressure, including a Zn-rich tribofilm, an oxide layer, and S enrichment. Higher content of Zn was found at the upper part of the tribofilm; in contrast, a more massive amount of Fe can be found at the lower part of the tribofilm.
- Sulfur enrichment was found between the tribofilm and the steel substrate. The sulfur-rich region distributed heterogeneously beneath the oxide layer in a range of approximately 5 nm. With the advantage of using APT, it is the first time that clear evidence has proven the existence of a sulfur enrichment covered by ZDDP tribofilm.
- The finding of sulfur enrichment supports the predictions according to the HSAB principle. The reaction between sulfide ions and nascent iron substrate, namely the soft reaction, triggers the formation of the tribofilm.

Acknowldgements

References

Bancroft, G.M., Kasrai, M., Fuller, M., Yin, Z., Fyfe, K. and Tan, K.H. (1997), "Mechanisms of tribochemical film formation: stability of tribo- and thermally-generated ZDDP films", *Tribology Letters*, Vol. 3 No. 1, pp. 47-51.

Bell, J.C., Delargy, K.M. and Seeney, A.M. (1992), "The removal of substrate material through thick zinc dithiophosphate anti-Wear films", *Tribology Series*, Vol. 21, pp. 387-396.

Berkani, S., Dassenoy, F., Minfray, C., Martin, J.M., Cardon, H., Montagnac, G. and Reynard, B. (2013), "Structural changes in tribo-stressed zinc polyphosphates", *Tribology Letters*, Vol. 51 No. 3, pp. 489-498.

De Barros, M.I.I., Bouchet, J., Raoult, I., Le Mogne, T., Martin, J.M.M., Kasrai, M. and Yamada, Y. (2003), "Friction reduction by metal sulfides in boundary lubrication studied by XPS and XANES analyses", *Wear*, Vol. 254 No. 9, pp. 863-870.

Dorgham, A., Azam, A., Morina, A. and Neville, A. (2018), "On the transient decomposition and reaction kinetics of zinc dialkyldithiophosphate", *ACS Applied Materials & Interfaces*, Vol. 10 No. 51, pp. 44803-44814.

Dowson, D., Higginson, G.R. and Whitaker, A.V. (1962), "Elasto-hydrodynamic lubrication: a survey of isothermal solutions", *Journal of Mechanical Engineering Science*, Vol. 4 No. 2, pp. 121-126.

Fujita, H. and Spikes, H.A. (2004), "The formation of zinc dithiophosphate antiwear films', proceedings of the institution of mechanical engineers", *Part J: Journal of Engineering Tribology*, Vol. 218 No. 4, pp. 265-278.

Fuller, M., Yin, Z., Kasrai, M., Bancroft, G.M., Yamaguchi, E.S., Ryason, P.R., Willermet, P.A. and Tan, K.H., (1997), "Chemical characterization of tribochemical and thermal films generated from neutral and basic ZDDPs using X-ray absorption spectroscopy", *Tribology International*, Vol. 30 No. 4, pp. 305-315.

Gachot, C., Hsu, C., Suárez, S., Grützmacher, P., Rosenkranz, A., Stratmann, A. and Jacobs, G. (2016), "Microstructural and chemical characterization of the tribolayer formation in highly loaded cylindrical roller thrust bearings", *Lubricants*, Vol. 4 No. 2, pp. 1-11.

Gault, B., Moody, M.P., Cairney, J.M. and Ringer, S.P. (2012), "Atom probe crystallography", *Materials Today.*, Vol. 15 No. 9.

Gosvami, N.N., Bares, J.A., Mangolini, F., Konicek, A.R., Yablon, D.G. and Carpick, R.W. (2015), "Mechanisms of antiwear tribofilm growth revealed in situ by single-asperity sliding contacts", *Science*, Vol. 348 No. 6230, pp. 102-106.

Guo, W., Zhou, Y., Sang, X., Leonard, D.N., Qu, J. and Poplawsky, J.D. (2017), "Atom probe tomography unveils formation mechanisms of wear-protective tribofilms by ZDDP, ionic liquid, and their combination", *ACS Applied Materials & Interfaces*, Vol. 9 No. 27, pp. 23152-23163.

Heuberger, R., Rossi, A. and Spencer, N.D. (2007), "XPS study of the influence of temperature on ZnDTP tribofilm composition", *Tribology Letters*, Vol. 25 No. 3, pp. 185-196.

Hsu, C.-J., Stratmann, A., Rosenkranz, A. and Gachot, C. (2017), "Enhanced growth of ZDDP-Based tribofilms on Laser-Interference patterned cylinder roller bearings", *Lubricants*, Vol. 5 No. 4, p. 39.

Kalin, M. (2004), "Influence of flash temperatures on the tribological behaviour in low-speed sliding: a review", *Materials Science and Engineering: A*, Vol. 374 Nos 1/2, pp. 390-397.

Kelly, T.F., Larson, D.J., Thompson, K., Alvis, R.L., Bunton, J.H., Olson, J.D. and Gorman, B.P. (2007), "Atom probe tomography of electronic materials", *Annual Review of Materials Research*, Vol. 37 No. 1, pp. 681-727.

Kelly, T.F. and Miller, M.K. (2007), "Invited review article: atom probe tomography", *Review of Scientific Instruments*, Vol. 78 No. 3, doi: 10.1063/1.2709758.

Kim, Y.J., Baik, S., Il, Bertolucci-Coelho, L., Mazzaferro, L., Ramirez, G., Erdermir, A. and Seidman, D.N. (2016), "Atom-probe tomography of tribological boundary films resulting from boron-based oil additives", *Scripta Materialia*, Vol. 111, pp. 64-67.

Kubiak, K.J., Mathia, T.G. and Bigerelle, M. (2012), "Influence of roughness on ZDDP tribofilm formation in boundary lubricated fretting", *Tribology - Materials Surfaces & Interfaces*, Vol. 6 No. 4, pp. 182-188.

Martin, J.M. (1999), "Antiwear mechanisms of zinc dithiophosphate: a chemical hardness approach", *Tribology Letters*, Vol. 6 No. 1, pp. 1-8.

Martin, J.M., Grossiord, C., Le Mogne, T., Bec, S. and Tonck, A. (2001), "The two-layer structure of zndtp tribofilms, part I: AES, XPS and XANES analyses", *Tribology International*, Vol. 34 No. 8, pp. 523-530.

Martin, J.M., Grossiord, C., Le Mogne, T. and Igarashi, J. (2000), "Transfer films and friction under boundary lubrication", *Wear*, Vol. 245 Nos 1-2, pp. 107-115.

Martin, J.M., Onodera, T., Minfray, C., Dassenoy, F. and Miyamoto, A. (2012), "The origin of anti-wear chemistry of ZDDP", *Faraday Discussions*, Vol. 156, p. 311.

Miller, M.K. and Forbes, R.G. (2009), "Atom probe tomography", *Materials Characterization*, doi: 10.1016/j.matchar.2009.02.007.

Minfray, C., Le Mogne, T., Lubrecht, AA. and Martin, J.M. (2006), "Experimental simulation of chemical reactions between ZDDP tribofilms and steel surfaces during friction processes", *Tribology Letters*, Vol. 21 No. 1, pp. 65-76.

Minfray, C., Martin, J.M., De Barros, M.I., Le Mogne, T., Kersting, R. and Hagenhoff, B. (2004a), "Chemistry of ZDDP tribofilm by ToF-SIMS", *Tribology Letters*, Vol. 17 No. 3, pp. 351-357.

Minfray, C., Martin, J.M., Esnouf, C., Le Mogne, T., Kersting, R. and Hagenhoff, B. (2004b), "A multi-technique approach of tribofilm characterisation", *Thin Solid Films*, Vols 447/448, pp. 272-277.

Miranda-Medina, M. de, L. Tomastik, C. Truglas, T. Groiss, H. and Jech, M. (2019), "Effect of engine oil additives reduction on the tribofilm structure of a cylinder liner model surface", *Industrial Lubrication and Tribology*, doi: 10.1108/ilt-05-2019-0193.

Mosey, N.J., Müser, M.H. and Woo, T.K. (2005), "Molecular mechanisms for the functionality of lubricant additives", *Science*, Vol. 307 No. 5715, pp. 1612-1615.

Nicholls, M.A., Do, T., Norton, P.R., Bancroft, G.M., Kasrai, M., Capehart, T.W., Cheng, Y.T. and Perry, T., (2003), "Chemical and mechanical properties of ZDDP antiwear films on steel and thermal spray coatings studied by XANES spectroscopy and nanoindentation techniques", *Tribology Letters*, Vol. 15 No. 3, pp. 241-248.

Onodera, T., Martin, J.M., Minfray, C., Dassenoy, F. and Miyamoto, A. (2013), "Antiwear chemistry of ZDDP: coupling classical MD and tight-binding quantum chemical MD methods (TB-QCMD)", *Tribology Letters*, Vol. 50 No. 1, pp. 31-39.

Onodera, T., Morita, Y., Suzuki, A., Sahnoun, R., Koyama, M., Tsuboi, H., Hatakeyama, N., Endou, A., Takaba, H., Kubo, M. and Del Carpio, C.A., (2008), "A theoretical investigation on the abrasive wear prevention mechanism of ZDDP and ZP tribofilms", *Applied Surface Science*, Vol. 254 No. 23, pp. 7976-7979.

Rosenkranz, A., Stratmann, A., Gachot, C., Burghardt, G., Jacobs, G., Mücklich, F., Rosenkranz, B.A. (2016), "Improved wear behavior of cylindrical roller thrust bearings by three-beam laser interference", *Advanced Engineering Materials*, Vol. 18 No. 5, pp. 854-862.

Schmaltz, G. (1936), *Technische Oberflächenkunde, Technische Oberflächenkunde*, Springer Berlin, doi: 10.1007/978-3-642-51820-1.

Shimizu, Y. and Spikes, H.A. (2016), "The tribofilm formation of ZDDP under reciprocating pure sliding conditions", *Tribology Letters*, Vol. 64 No. 3, pp. 1-11.

Smith, G.C. and Bell, J.C. (1999), "Multi-technique surface analytical studies of automotive anti-wear films", *Applied Surface Science*, Vols 144/145, pp. 222-227.

Soltanahmadi, S., Morina, A., van Eijk, M.C.P., Nedelcu, I. and Neville, A. (2017), "Experimental observation of zinc dialkyl dithiophosphate (ZDDP)-induced iron sulphide formation", *Applied Surface Science*, Vol. 414, pp. 41-51.

Spikes, H. (2004), "The history and mechanisms of ZDDP", *Tribology Letters*, Vol. 17 No. 3, pp. 469-489.

Stratmann, A., Jacobs, G., Hsu, C.-J., Gachot, C. and Burghardt, G. (2017), "Antiwear tribofilm growth in rolling bearings under boundary lubrication conditions", *Tribology International*, Vol. 113, pp. 43-49.

Thompson, K., Lawrence, D., Larson, D.J., Olson, J.D., Kelly, T.F. and Gorman, B. (2007), "In situ site-specific specimen preparation for atom probe tomography", *Ultramicroscopy*, Vol. 107 Nos 2/3, pp. 131-139.

Topolovec-Miklozic, K., Forbus, T.R. and Spikes, H.A. (2007), "Film thickness and roughness of ZDDP antiwear films", *Tribology Letters*, Vol. 26 No. 2, pp. 161-171.

Zhang, Z., Yamaguchi, E.S., Kasrai, M. and Bancroft, G.M. (2005), "Tribofilms generated from ZDDP and DDP on steel surfaces: part 1, growth, wear and morphology", *Tribology Letters*, Vol. 19 No. 3, pp. 211-220.

Zhou, Y., Leonard, D.N., Guo, W. and Qu, J. (2017), "Understanding tribofilm formation mechanisms in ionic liquid lubrication", *Scientific Reports*, Vol. 7 No. 1, pp. 1-8.

Corresponding author

Chia-Jui Hsu can be contacted at: chiajui.hsu@uni-saarland.de

11. PAPER III

Title:

Enhanced Growth of ZDDP-Based Tribofilms on Laser-Interference Patterned Cylinder Roller Bearings

Authors:

Chia-Jui Hsu[1,*], Andreas Stratmann[2], Andreas Rosenkranz[3], Carsten Gachot[4]

[1] Chair of Functional Materials, Saarland University, 66123 Saarbrücken, Germany

[2] Institute for Machine Elements and Machine Design, 52062 RWTH Aachen, Aachen, Germany

[3] Center for Memory and Recording Research, University of California, San Diego, La Jolla, CA 92093, USA

[4] Institute for Engineering Design and Logistics Engineering, TUWien, 1060 Vienna, Austria

Owned contributions: Laser texturing; Raman spectroscopy and surface characterization; data analyses; paper writing.

11. PAPER III

Enhanced Growth of ZDDP-Based Tribofilms on Laser-Interference Patterned Cylinder Roller Bearings

Chia-Jui Hsu [1],* [ID]**, Andreas Stratmann** [2] [ID]**, Andreas Rosenkranz** [3] **and Carsten Gachot** [4] [ID]

[1] Chair of Functional Materials, Saarland University, 66123 Saarbrücken, Germany
[2] Institute for Machine Elements and Machine Design, 52062 RWTH Aachen, Aachen, Germany;
    andreas.stratmann@ime.rwth-aachen.de
[3] Center for Memory and Recording Research, University of California, San Diego, La Jolla, CA 92093, USA;
    arosenkranz@ucsd.edu
[4] Institute for Engineering Design and Logistics Engineering, TU Wien, 1060 Vienna, Austria;
    carsten.gachot@tuwien.ac.at
*   Correspondence: chiajui.hsu@uni-saarland.de; Tel.: +49-681302-70543

Abstract: Laser surface texturing has been successfully applied in the past to various machine elements in order to improve their tribological performance. In this study, direct laser interference patterning was used to produce periodic cross-like surface patterns on commercial cylinder roller bearings. The wear behavior of as-patterned bearings was studied by a modified FE8 test rig under boundary lubrication. A mineral oil (ISO VG 100) as a base oil additivated with 0.02 wt % zinc dialkyldithiophosphate (ZDDP) was used for the tribological tests which were performed under a Hertzian pressure of 1.92 GPa and maintained at 80 °C and 20 rpm for 2 h. The laser-patterned bearings showed a significantly reduced mass loss by two orders of magnitude compared to the unpatterned reference bearings. A closer look at the samples proved the formation of the characteristic blue-colored ZDDP tribofilm on top of the laser-induced topography maximum positions. Due to the higher contact pressure at the laser-induced peaks, the tribofilm formation was preferable at those positions thus protecting against wear. The laser patterns nearly remained unworn compared to the reference samples. A subsequent Raman analysis of the laser-patterned bearings clearly revealed the formation of zinc and iron sulfides as well as phosphates at the peak points.

Keywords: laser surface treatment; direct laser interference patterning; boundary lubrication; ZDDP; roller bearings

1. Introduction

In tribology, boundary lubrication is a lubrication regime which typically appears in the interfaces of gears, bearings, and piston rings, etc., for relatively low sliding speeds and rather high loads [1]. In this lubrication regime, the oil film thickness is generally significantly lower than the combined surface roughness of both rubbing partners, which can be reflected in a λ-parameter smaller than 1. As a consequence, the surface asperities play an important role since the load is mainly carried by those asperities. Wear occurs inevitably under boundary lubrication, and it is well known that the formation of an anti-wear tribolayer is the solution to protect the substrate and to prevent severe wear [2,3]. In terms of tribofilm formation, zinc dialkyldithiophosphate (ZDDP) can be named as a popular lubricant additive, which has been widely studied and utilized for more than 70 years due to its outstanding anti-wear performance and its additional multi-functional characteristics such as anti-corrosion and antioxidant properties. Those properties can help to provide protection against damage from wear and to extend the component's lifetime. In general, ZDDP tribofilms are described as blue and brown-colored patchy layers formed in the rubbing area [4]. Those layers are composed

of, for example, iron sulfides and amorphous orthophosphates [5]. There are two ways to generate ZDDP reaction layers, either by thermal activation or tribomechanical reactions [6,7]. In this context, Bancroft et al. demonstrated that tribomechanically induced tribofilms are more stable against wear [8]. Gosvami et al. proved that the tribofilm formation is pressure-induced and not thermally induced. [9]. Furthermore, Gachot et al. proved that the blue-colored tribofilm areas contain a high amount of phosphates and zinc sulfides [10]. Even though the mechanism of the ZDDP tribofilm formation and the detailed reaction paths are still not clear and well understood, there is a consensus that the presence of the tribofilm can help to protect the rubbing surface, thus improving the friction and wear performance [11].

Despite the aforementioned beneficial effects, there are more and more restrictions for the usage of ZDDP because phosphorous and sulphur oxides reduce the effective lifetime of exhaust catalysts [12]. It is necessary to introduce other methods that can reduce both the wear and the usage of ZDDP. Lately, laser surface texturing (LST) has become a powerful tool for surface modification due to its ability to precisely tailor materials [13–15]. Lasers using pulses with short and ultra-short pulse duration such as nano- and femtoseconds have been typically used in this context because of their high flexibility towards various materials. However, one shortcoming that can be named is the processing time. Complex pattern geometries require a relatively long time to be fabricated. In addition to that, in order to modify large surfaces, the individual laser pulses need to be overlapped, which might lead to slight inhomogeneities in the overlapping areas [3]. Therefore, direct laser interference patterning (DLIP) was developed to produce complex patterns on a relatively large area in just a single laser shot. DLIP ensures a time-efficient and fast surface modification by superimposing two or more coherent laser beams [12,16]. This technique produces periodic patterns onto the surface of interest and has been proven to give characteristic patterns for versatile functions, such as friction and wear reduction [17–19], reduction of the electrical contact resistance [20], and modifications of wetting properties [21,22]. For the frictional modification induced by DLIP, Gachot et al. suggested that the surface geometry is the most significant influencing factor [19]. Rosenkranz et al. demonstrated that dot-like patterns on the surface of bearings produced by three beams interference perform well and show a wear reduction of 83% compared to the reference state. The patterns were able to store wear particles in the topographic valleys, thus reducing abrasive wear and therefore lowering the wear volume. Even though DLIP would create an additional artificial roughness on the contact surface, which might lead to an increased contact pressure, the ability to store wear particles seems to be promising in terms of wear reduction [23].

The aim of the present research study is to investigate the effects of specific surface patterns created by DLIP on the wear performance of highly loaded cylinder roller bearings under boundary lubrication, as well as the interaction between the resulting surfaces patterns and the ZDDP additivated oil. Moreover, the formation of the tribolayer and its properties are demonstrated and discussed.

2. Experiments

2.1. FE8 Test Rig

In the present study, cylinder roller bearings (Type 81212), consisting of two washers, a cage, and several cylinder rollers made of $100Cr_6$ bearing steel (AISI 52100) were tested in a modified FE8 test rig corresponding to DIN 51819-3. A mineral oil of class ISO VG 100 was used as base oil and mixed with ZDDP additive using a concentration of 0.02 wt %phosphorus and short secondary chains (C3–C8). During the test, sufficient lubricant was supplied to the contact area by a pumping system. The rotational speed was set to 20 rpm. The test was run at 80 °C with an axial load of 80 kN, which corresponds to a Hertzian pressure of 1.92 GPa. The total testing time was 2 h. The lubricating condition was calculated as boundary lubrication according to Dowson et al. [24], with a minimum film height $h_0 = 4.88$ nm. After the test, the surface was cleaned by using benzene and isopropanol to

remove the residual lubricant, abrasives, and contaminants. More details regarding the test rig and testing parameters can be found elsewhere [25].

2.2. Direct Laser Interference Patterning (DLIP)

DLIP is a surface treatment conducted by applying interfering sub-beams onto the target samples which can produce a relatively large patterning area in a short period of time. A pulsed Nd:YAG laser (Quanta Ray Pro 290, Spectra Physics, Santa Clara, CA, USA) was used providing a wavelength of 532 nm. The repetition rate of the laser was 10 Hz with pulse duration of 10 ns. The peak power of the laser was 0.83 J·cm^{-2}. Figure 1 shows the experimental setup needed to realize DLIP.
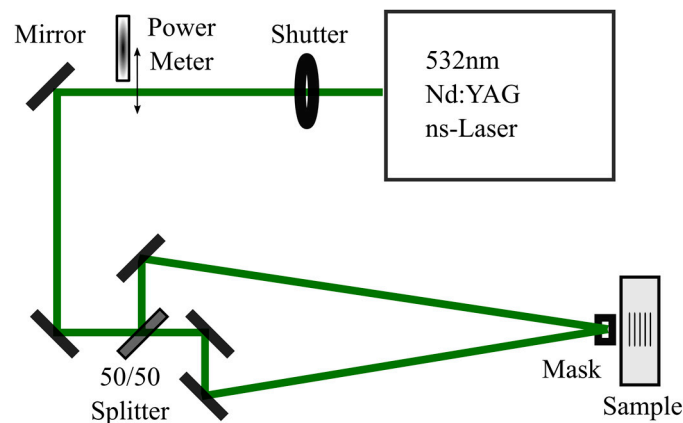

Figure 1. Schematic diagram of direct laser interference patterning (DLIP) in order to realize two-beam interference.

The primary beam (circular beam of around 10 mm in diameter) was then controlled by a mechanical shutter system (VS25S2ZMO, Uniblitz Electronic, Rochestern, NY, USA), allowing only one pulse passing by for each shot. The laser power was measured by a pyrometric power meter (EnergyMax Sensors, Coherent, Palo Alto, CA, USA). The primary beam was split into two sub-beams by using a beam splitter. Afterwards, highly reflective mirrors were used to superimpose the sub-beams onto the sample. Two-beam interference generated a periodic line-like surface topography. By changing the incident angle between the two sub-beams the periodicities could be modified in a range from 1 to 30 μm. Finally, the overlapping area was selected and shaped as 1×1 mm^2 by applying a squared refractory mask. Therefore, the line-like pattern was formed on the surface of the bearing washer. In addition, the position of the sample was controlled by a programmable *x-y* stage. In this study, the bearing washer was rotated by 90° after the first patterning step in order to produce cross-like surface patterns.

2.3. Characterization

Surface chemistry was examined by Raman spectroscopy (confocal Raman microscope, Renishaw, Wotton-under-Edge, UK) equipped with a grating of 2400 lines mm^{-1} and a spectral resolution up to 1.2 cm^{-1}. A laser producing an excitation wavelength of 532 nm was used to provide a power of 500 mW. The laser power was set as 10% to prevent thermal damage of the tribolayer. The spectrum between 200 and 1300 cm^{-1} was obtained using an acquisition time of 200 s. In addition, the overall morphology and topography of the laser-patterned samples and the wear tracks were imaged using laser scanning microscopy (LSM, LEXT OLS4100, Tokyo, Japan) and white light interferometry (WLI, Zygo NewView 7300, Harpenden, UK). The wear loss of the bearing was evaluated after the tribological experiments using a precision balance (CP324S Sartorius, Elk Grove Village, IL, USA).

3. Results and Discussions

3.1. Surface topography

The surface topography of the bearing washer after DLIP is shown in Figure 2, which clearly shows the cross-like patterns with a mean structural depth (peak to valley) of 1.2 µm and a lateral periodicity of 30 µm. In a previous review paper summarizing the effects of surface patterning on friction and wear, it was suggested that the structural depth of the laser pattern should be in the micron range for boundary lubrication [3]. DLIP typically produces pattern geometries with a mean structural depth of roughly 1–2 µm which makes DLIP an interesting approach to influence the tribological performance under boundary lubrication. The roughness parameters of the reference and patterned surfaces are summarized in Table 1, including values of R_{rms}, R_{tm}, and R_{sk}. It can be clearly seen that the surface roughness increased after DLIP because R_{rms} increases from 0.07 to 0.3 µm. The value R_{tm} (mean of maximum peak to valley height) can be used to evaluate the performance of the patterned surface showing the depth below the contact surface which will store lubricant and supply lubricant to the contact area when needed. Moreover, the value R_{sk} (skewness) also provides information about the lubricant preservation. For positive R_{sk} values, a high amount of valleys can be found indicating a larger capacity to store lubricant [26]. Based upon the presented values, the surface roughness increases after DLIP. Although a possible storage of lubricant can be ensured, the induced surface topography by DLIP might increase friction and wear due to edge effects and stress concentrations.

Table 1. Summary of the roughness parameters of the reference and the laser-patterned surface, prior to and after rubbing (R_{rms}: root mean square; R_{tm}: mean of maximum peak to valley height; R_{sk}: skewness).

	Prior to Rubbing			After Rubbing		
	R_{rms}/µm	R_{tm}/µm	R_{sk}	R_{rms}/µm	R_{tm}/µm	R_{sk}
Reference	0.07 ± 0.01	0.28 ± 0.05	-0.60 ± 0.05	0.08 ± 0.01	0.03 ± 0.01	-0.88 ± 0.27
Cross-patterned	0.30 ± 0.02	1.39 ± 0.07	0.15 ± 0.13	0.20 ± 0.01	0.81 ± 0.07	-0.23 ± 0.04

In this case, the formation of the tribolayer would be the solution to prevent severe wear damage. As long as an anti-wear tribofilm is formed on the contact surface, the harmful abrasive particles would not be generated, thus protecting the surface from wear.
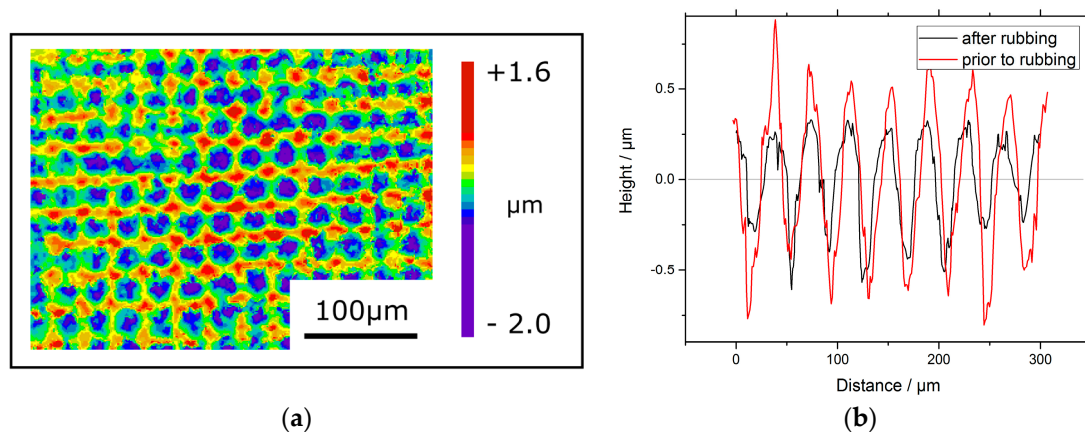

Figure 2. Surface morphology (**a**) and surface profile (**b**) of the laser-patterned cross-like structure with a periodicity of 30 µm imaged by white light interferometry (WLI). In (**b**), a comparison of the surface profile prior to and after rubbing is presented.

3.2. Tribological Performance

In Table 1, the roughness parameters prior to and after rubbing are shown in order to evaluate the effect of DLIP on the tribological performance. After rubbing, the R_{tm} value also decreases from 1.39 to 0.81 µm, indicating unpreventable wear damage. However, the value is still much higher than the respective value of the untreated reference sample. Additionally, it should be emphasized that the periodical cross-like patterns remain intact with a reduced structural depth (approximately 40% of the initial value) after rubbing. This effect can be well seen in Figure 2b. Both results show that the capacity of DLIP to store lubricant and to trap abrasive particles remains, even after 2 h of testing under severe conditions. Furthermore, R_{sk} shifts from positive to negative values, indicating a more plateau-like topography along the rubbed surface. According to the decrease of both R_{tm} and R_{sk}, it can be concluded that the sharp peaks were flattened to blunt asperities during rubbing, thus leading to a better load-carrying capacity.

The coefficient of friction was measured during rubbing. The average coefficient of friction (COF) of the reference sample is 0.14, whereas the value for the cross-patterned surface is about 0.1. The COF of the DLIP sample decreases approximately 30%, and the measurement of wear mass losses was further introduced. In Table 2, the respective wear losses of the washer and the roller set (reference and laser-patterned) are presented. The mass loss was evaluated by comparing the weight of the washer and the roller set prior to and after rubbing. For the reference washer without DLIP, it can be seen that after two hours a rather large mass loss of 62.5 mg can be measured. In contrast to that, the wear damage of the laser-patterned surface can be barely seen. It can be stated that the respective mass loss could be reduced by two orders of magnitude. In addition, for the roller set, the same experimental trends in terms of mass loss can be detected. This implies that DLIP offers the possibility of preventing the bearing from severe wear, which could be attributed to the topography due to abrasive particles and insufficient lubricant supply. Moreover, the formation of ZDDP tribofilm which was mentioned earlier prevents direct contact between two metal surfaces thus decreasing the damage from wear.

Table 2. Summary of the total mass loss of the washer and roller set of the roller bearings for the reference and laser-patterned sample.

	Washer Mass Loss Δm/mg	Roller Set Mass Loss Δm/mg
Reference	62.5	80.5
Cross-patterned	0.1	0.1

In Figure 3, the surface topography after rubbing imaged by optical and laser scanning microscopy is depicted. It can be observed that the cross-like structure remains intact with a reduced mean depth of 0.9 µm. Furthermore, it should be mentioned that P_1 marks a blue spot in Figure 3a,b. By comparing both figures, the blue spots typically formed by the tribofilm can be found in the topographic maximum positions. It is worth mentioning that a second spot, P_2, was marked in the figures, representing the area of the topographic minimum position. In those regions, there is no sign of tribofilm formation in the topographic valleys (P_2 in Figure 3a,b). Since ZDDP tribolayers can be described as a mixture of blue- and brown-colored films distributed in the contact region [4,27], the blue tribofilm can be traced back to pressure and sliding friction. Consequently, the blue spots appearing in those figures can be attributed to the ZDDP tribofilm, which is the key feature to provide protection of the contact surfaces against wear [8,11]. Finally, those two points (P_1 and P_2) were selected to analyze the surface chemistry by Raman spectroscopy dependent on the surface topography (topographic maximum and minimum positions).
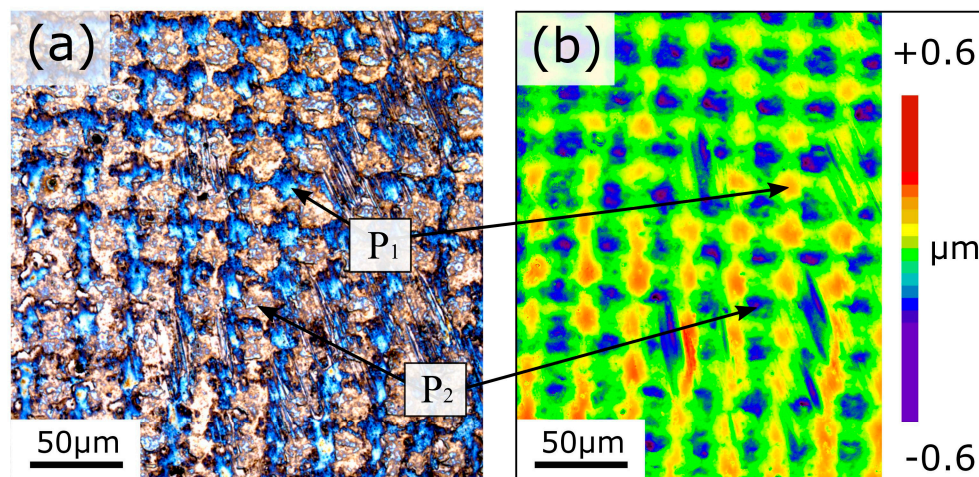
Figure 3. Surface topography after rubbing imaged by (**a**) optical microscopy and (**b**) laser scanning microscopy (LSM). P_1 marks a position with blue-colored tribofilm on the top of patterns, whereas P_2 highlights a region of valleys without blue color.

3.3. Raman Spectroscopy

The surface chemistry of the ZDDP tribofilms on the cross-like patterns was studied by Raman spectroscopy. In Figure 4, the corresponding Raman spectra for P_1 and P_2 are depicted. The spectrum measured at P_1 shows pronounced peaks related to Zn–S, Fe–S, and P–O at Raman shifts of 351, 386, and 965 cm^{-1} [28–30], whereas P_2 reveals peaks related to Fe$_3$O$_4$ at 320 and 670 cm^{-1} [31]. The peaks assigned to P_1 correlate well with the composition of ZDDP, which goes hand in hand with previously published results [10]. This in turn implies that the tribolayer was formed on top of the pattern induced by the increased contact pressure. As shown by Bancroft et al. [8], the pressure-induced tribofilms exhibit better tribological performance compared to the thermally induced films. Under tribological contact, the tribofilm grows faster due to the applied pressure [7]. The presence of the blue tribofilm appears only on top of the patterns, which significantly reduces the wear loss, and proves the pressure-induced film formation.
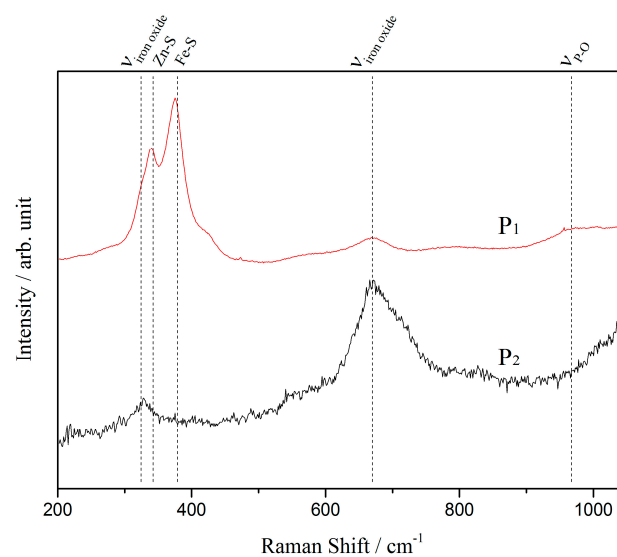

Figure 4. Raman spectra measured at P_1: blue-colored tribofilm on the topographical maximum of the patterns, and P_2: valley area of the patterns after rubbing.

4. Conclusions

In this study, the effects of periodic cross-like patterns produced by DLIP on the tribological and wear performance of cylinder roller bearings were studied by using a modified FE8 test rig. The mass loss was evaluated by a precision balance and the topography was measured and described by WLI and LSM. Moreover, the surface chemistry was analyzed by Raman spectroscopy.

Topographic parameters such as R_{tm} and R_{sk} demonstrated that the periodic laser patterns, which are able to store lubricant and trap abrasive particles during rubbing, remain intact even after severe rubbing. The surface has no obvious wear marks, and the characteristic blue-colored tribolayer was only formed at the laser-induced topographic maximum positions of the patterned surface with the highest contact pressure, thus confirming the formation of a pressure-induced tribofilm. A subsequent Raman analysis clearly revealed peaks related to Zn–S, Fe–S, and P–O in the Raman spectra typical for the blue-colored tribolayer. Because the successful tribofilm formation at the topographic maxima positions were in contact with the counter-body, the wear loss could be significantly decreased in comparison to the unpatterned reference sample.

Author Contributions: In this study, Chia-Jui Hsu and Carsten Gachot conceived and designed the experiments; Chia-Jui Hsu and Andreas Stratmann performed the experiments; Chia-Jui Hsu, Carsten Gachot, Andreas Stratmann and Andreas Rosenkranz analyzed and discussed the data as well as wrote the manuscript.

Conflicts of Interest: The authors declare no conflict of interest.

References

1. Hsu, S.M.; Gates, R.S. Boundary lubricating films: Formation and lubrication mechanism. *Tribol. Int.* **2005**, *38*, 305–312. [CrossRef]
2. Spikes, H.A. Boundary Lubrication and Boundary Films. *Tribol. Ser.* **1993**, *25*, 331–346.
3. Gachot, C.; Rosenkranz, A.; Hsu, S.M.; Costa, H.L. A critical assessment of surface texturing for friction and wear improvement. *Wear* **2017**, *372–373*, 21–41. [CrossRef]
4. Hsu, S.M. Boundary Lubrication of Materials. *MRS Bull.* **1991**, *16*, 54–58. [CrossRef]
5. Martin, J.M. Antiwear mechanisms of zinc dithiophosphate: A chemical hardness approach. *Tribol. Lett.* **1999**, *6*, 1–8. [CrossRef]
6. Fuller, M.; Bancroft, G.M.; Tan, K.H.; Yamaguchi, E.S.; Ryason, P.R.; Wiliermet, P.A. Chemical characterization of chemical and thermal films generated from neutral and basic ZDDPs using X-ray absorption spectroscopy. *Tribol. Int.* **1997**, *30*, 305–315. [CrossRef]
7. Fujita, H.; Spikes, H.A. The formation of zinc dithiophosphate antiwear films. *Proc. Inst. Mech. Eng. Part J J. Eng. Tribol.* **2004**, *218*, 265–278. [CrossRef]
8. Bancroft, G.M.; Kasrai, M.; Fuller, M.; Yin, Z.; Fyfe, K.; Tan, K.H. Mechanisms of tribochemical film formation: Stability of tribo- and thermally-generated ZDDP films. *Tribol. Lett.* **1997**, *3*, 47–51. [CrossRef]
9. Gosvami, N.N.; Bares, J.A.; Mangolini, F.; Konicek, A.R.; Yablon, D.G.; Carpick, R.W. Mechanisms of antiwear tribofilm growth revealed in situ by single-asperity sliding contacts. *Science* **2015**, *348*, 102–106. [CrossRef] [PubMed]
10. Gachot, C.; Hsu, C.; Suárez, S.; Grützmacher, P.; Rosenkranz, A.; Stratmann, A.; Jacobs, G. Microstructural and Chemical Characterization of the Tribolayer Formation in Highly Loaded Cylindrical Roller Thrust Bearings. *Lubricants* **2016**, *4*, 19. [CrossRef]
11. Spikes, H. The history and mechanisms of ZDDP. *Tribol. Lett.* **2004**, *17*, 469–489. [CrossRef]
12. Lasagni, A.; Holzapfel, C.; Weirich, T.; Mücklich, F. Laser interference metallurgy: A new method for periodic surface microstructure design on multilayered metallic thin films. *Appl. Surf. Sci.* **2007**, *253*, 8070–8074. [CrossRef]
13. Etsion, I.; Halperin, G.; Brizmer, V.; Kligerman, Y. Experimental investigation of laser surface textured parallel thrust bearings. *Tribol. Lett.* **2004**, *17*, 295–300. [CrossRef]

14. Etsion, I. State of the Art in Laser Surface Texturing. *J. Tribol.* **2005**, *127*, 248. [CrossRef]

15. Li, X.; Bhushan, B. Micromechanical and tribological characterization of hard amorphous carbon coatings as thin as 5 nm for magnetic recording heads. *Wear* **1998**, *220*, 51–58. [CrossRef]

16. Mücklich, F.; Lasagni, A.; Daniel, C. Laser interference metallurgy—Periodic surface patterning and formation of intermetallics. *Intermetallics* **2005**, *13*, 437–442. [CrossRef]

17. Duarte, M.; Lasagni, A.; Giovanelli, R.; Narciso, J.; Louis, E.; Mücklich, F. Increasing lubricant film lifetime by grooving periodical patterns using laser interference metallurgy. *Adv. Eng. Mater.* **2008**, *10*, 554–558. [CrossRef]

18. Rosenkranz, A.; Jaeger, S.; Gachot, C.; Vogel, S.; Mücklich, F. Wear Behavior of Laser-Patterned Piston Rings in Squeeze Film Dampers. *Adv. Eng. Mater.* **2015**, *17*, 1208–1214. [CrossRef]

19. Gachot, C.; Rosenkranz, A.; Reinert, L.; Ramos-Moore, E.; Souza, N.; Müser, M.H.; Mücklich, F. Dry friction between laser-patterned surfaces: Role of alignment, structural wavelength and surface chemistry. *Tribol. Lett.* **2013**, *49*, 193–202. [CrossRef]

20. Trinh, K.E.; Tsipenyuk, A.; Varenberg, M.; Rosenkranz, A.; Souza, N.; Mücklich, F. Wear debris and electrical resistance in textured Sn-coated Cu contacts subjected to fretting. *Wear* **2015**, *344–345*, 86–98. [CrossRef]

21. Hans, M.; Müller, F.; Grandthyll, S.; Hüfner, S.; Mücklich, F. Anisotropic wetting of copper alloys induced by one-step laser micro-patterning. *Appl. Surf. Sci.* **2012**, *263*, 416–422. [CrossRef]

22. Grützmacher, P.G.; Rosenkranz, A.; Gachot, C. How to guide lubricants—Tailored laser surface patterns on stainless steel. *Appl. Surf. Sci.* **2016**, *370*, 59–66. [CrossRef]

23. Rosenkranz, A.; Stratmann, A.; Gachot, C.; Burghardt, G.; Jacobs, G.; Mücklich, F. Improved wear behavior of cylindrical roller thrust bearings by three-beam laser interference. *Adv. Eng. Mater.* **2016**, *18*, 854–862. [CrossRef]

24. Dowson, D.; Higginson, G.R.; Whitaker, A.V. Elasto-hydrodynamic Lubrication: A Survey of Isothermal Solutions. *J. Mech. Eng. Sci.* **1962**, *4*, 121–126. [CrossRef]

25. Stratmann, A.; Jacobs, G.; Hsu, C.J.; Gachot, C.; Burghardt, G. Antiwear tribofilm growth in rolling bearings under boundary lubrication conditions. *Tribol. Int.* **2017**, *113*, 43–49. [CrossRef]

26. Gadelmawla, E.S.; Koura, M.M.; Maksoud, T.M.A.; Elewa, I.M.; Soliman, H.H. Roughness parameters. *J. Mater. Process. Technol.* **2002**, *123*, 133–145. [CrossRef]

27. De Barros, M.I.; Bouchet, J.; Raoult, I.; Le Mogne, T.; Martin, J.M.; Kasrai, M.; Yamada, Y. Friction reduction by metal sulfides in boundary lubrication studied by XPS and XANES analyses. *Wear* **2003**, *254*, 863–870. [CrossRef]

28. Brafman, O.; Mitra, S.S. Raman effect in wurtzite- and zinc-blende-type ZnS single crystals. *Phys. Rev.* **1968**, *171*, 931–934. [CrossRef]

29. Ushioda, S. Raman scattering from phonons in iron pyrite (FeS2). *Solid State Commun.* **1972**, *10*, 307–310. [CrossRef]

30. Berkani, S.; Dassenoy, F.; Minfray, C.; Martin, J.M.; Cardon, H.; Montagnac, G.; Reynard, B. Structural changes in tribo-stressed zinc polyphosphates. *Tribol. Lett.* **2013**, *51*, 489–498. [CrossRef]

31. De Faria, D.L.A.; Silva, S.V.; de Oliveira, M.T. Raman microspectroscopy of some iron oxides and oxyhydroxides. *J. Raman Spectrosc.* **1997**, *28*, 873–878. [CrossRef]

12. PAPER IV

Title:

Do Laser Surface Textures really decrease Fatigue Lifetime of Components under Boundary Lubrication Regime?

Authors:

Chia-Jui Hsu[1, 2, 3]*, Andreas Stratmann[4], Simon Medina[1], Georg Jacobs[4], Frank Mücklich[2], Carsten Gachot[1]

[1] Institute for Engineering Design and Product Development, TU Wien, 1060 Vienna, AUSTRIA

[2] Chair of Functional Materials, Saarland University, Campus D3.3, 66123 Saarbrücken, GERMANY

[3] AC2T Research GmbH, Viktor-Kaplan-Straße 2/C, 2700 Wiener Neustadt, AUSTRIA

[4] Institute for Machine Elements and Systems Engineering, RWTH Aachen, Schinkelstraße 10, 52062 Aachen, GERMANY

12. PAPER IV

Does laser surface texturing really have a negative impact on the fatigue lifetime of mechanical components?

Chia-Jui HSU[1,2,3,*], **Andreas STRATMANN**[4], **Simon MEDINA**[1], **Georg JACOBS**[4], **Frank MÜCKLICH**[2], **Carsten GACHOT**[1]

[1] *Institute for Engineering Design and Product Development, TU Wien, Lehárgasse 6, Campus Getreidemarkt, Vienna 1060, Austria*

[2] *Chair of Functional Materials, Saarland University, Campus D3.3, Saarbrücken 66123, Germany*

[3] *AC2T Research GmbH, Viktor-Kaplan-Straße 2/C, Wiener Neustadt 2700, Austria*

[4] *Institute for Machine Elements and Systems Engineering, RWTH Aachen, Schinkelstraße 10, Aachen 52062, Germany*

Abstract: Laser surface texturing (LST) has been proven to improve the tribological performance of machine elements. The micro-scale patterns manufactured by LST may act as lubricant reservoirs, thus supplying oil when encountering insufficient lubrication. However, not many studies have investigated the use of LST in the boundary lubrication regime, likely due to concerns of higher contact stresses that can occur with the increasing surface roughness. This study aims to examine the influence of LST on the fatigue lifetime of thrust rolling bearings under boundary lubrication. A series of periodic patterns were produced on the thrust rolling bearings, using two geometrically different designs, namely cross and dimple patterns. Base oil ISO VG 100 mixed with 0.05 wt% P of zinc dialkyldithiophosphate (ZDDP) was supplied. The bearings with cross patterns reduce the wear loss by two orders of magnitude. The patterns not only retain lubricant in the textured pockets but also enhance the formation of an anti-wear tribofilm. The tribofilm generation may be improved by the higher contact stresses that occur when using the textured surface. Therefore, in contrast to the negative concerns, the ball bearings with cross patterns were instead found to increase the fatigue life by a factor of three.

1 Introduction

The occurrence of pitting failure often limits the lifetime of machine components operating under rolling/sliding contacts, such as bearings and gears. Rolling contact fatigue (RCF) is initiated by micro-cracks, and the growth of cracks eventually leads to surface pitting and failures. Pitting failures can be categorized by the location of the micro-cracks: either in the sub-surface zone or on the surface of the material. Sub-surface failures have become less frequent due to improvements in steelworks, which has decreased the amount of

inclusions [1]. However, surface-initiated pitting, which begins with cracks initiated by defects, wear debris, or asperities on the surface, has caused a rising percentage of failures in modern applications [2]. This is attributed to the lower thickness of oil film that occurs when pursuing increased efficiency via reducing lubricant viscosity or adopting higher machining power, which makes the machine components operate in severe lubrication conditions, namely the boundary lubrication regime. Boundary lubrication is defined as the regime with a small ratio of the oil film thickness to the mean roughness value, and is mostly associated

---

* Corresponding author: Chia-Jui HSU, E-mail: chia-jui.hsu@tuwien.ac.at

with a high load and a low sliding speed, where only monolayers of a lubricant cover the interacting surfaces [3, 4]. In principle, wear is unavoidable in this lubrication regime, and wear debris can further damage the surface, which promotes the initiation of pitting [5]. Consequently, surface engineering and anti-wear tribofilms are recommended, to enhance wear resistance in boundary lubrication [6–9].

Novel methods of surface engineering, such as laser surface texturing (LST), have been proven to be beneficial for the tribological performance [10]. It is suggested that LST provides positive contributions in every lubrication condition, from the boundary to the hydrodynamic regime [11, 12]. The unique topography of the laser patterns can retain lubricants in the contact zone, thus providing the necessary lubrication when external supply is insufficient. In addition, the space within patterns can trap harmful wear debris in the valleys and prevent them from causing further damage on the contacting surfaces [6]. Laboratory tests have demonstrated promising improvements to tribological performance. LST has been evaluated and shown to decrease wear and friction in industrial applications such as roller bearings [13], ball bearings [14], valves [15], and pistons [16]. In case of conformal contacts, many studies have highlighted positive results by texturing with the area coverage between 10%–30%. In case of non-conformal contacts, smaller sizes and shallower depths (around 1 μm or less) have led to better performances [7]. Nevertheless, further experimental results using LST are required to fully determine the limitation and the applicability of LST.

Another approach to avoiding direct contact in the boundary lubrication regime is to generate a protection layer. The so-called anti-wear tribofilm is usually produced by the introduction of certain lubricant additives. Zinc dialkyldithiophosphate (ZDDP), which is one of the most popular oil additives, was used in this study. It has been shown that the presence of the ZDDP tribofilm reduces wear [17–19]. The layer is often described as an island-like thin-film, with a thickness of around 100 nm and width from 0.5 to several micrometers [8, 20]. The origin of the layer formation is the energy input to the contact area [21], driven by shear and temperature. Moreover, the growth of the tribofilm is confirmed to be more efficient when induced by tribological/shearing action [22].

Compared to the film generated only by temperature, the shear-induced tribolayer is more stable and has better wear resistance [17].

According to previous studies, the combined use of LST and anti-wear tribofilm reduces sliding induced damage [7, 23–26]. Rosenkranz et al. tested and confirmed the enhancement of the frictional performances on thrust roller bearings with dot patterns [12, 13]. Hsu et al. have found a fully formed ZDDP tribofilm at the topographical maximum of a periodic laser pattern, indicating an enhancement of the formation of ZDDP tribofilm by direct laser interference patterning (DLIP) [27]. Furthermore, the proven ability of surface protection by LST can further reduce fatigue failures. As an illustration, the fatigue lifetime of roller bearings under elastohydrodynamic lubrication was increased by mechanical surface texturing [28]. However, to the best of our knowledge, there is still no fatigue study under boundary lubrication considering laser textured samples. Therefore, this study aims at evaluating the fatigue lifetime of laser textured rolling bearings. Four different patterns geometry designs were initially tested for performance in terms of wear, and the best of these designs were used for the subsequent fatigue tests. The results are statistically analyzed by Weibull distribution. Finally, the effect of the laser patterns on the contact pressure distribution has been examined through contact simulation models.

2 Experiments and methods

2.1 Laser surface texturing

Two geometrically different LST patterns were tested in the present study: dimple and cross patterns. Samples were cleaned by ethanol and isopropanol before laser treatments. The surface preparation details can be found in Table 1, and the schematic of the LST pattern is shown in Fig. 1.

The dimple patterns with a depth of approximate 0.9 μm and a diameter of 30 μm were manufactured by a Ti-sapphire femtosecond pulsed laser (Spitfire Pro, Spectra Physics). The laser was applied with a wavelength of 800 nm, a frequency of 1 kHz, and a pulse duration of 150 fs. Each dimple was created from one laser pulse by using a controlled shutter.

Table 1 Experimental details of the patterns by laser surface texturing.

Samples	Peak energy (J/cm^2)	Pulse duration	Pattern type	Periodicity (μm)	Height (μm)
Dimple500	12.7	150 fs	Dimple	500	0.9
Dimple200	12.7	150 fs	Dimple	200	0.9
Cross9	1.2	10 ns	Cross	9	1.1
Cross30	1.2	10 ns	Cross	30	1.1
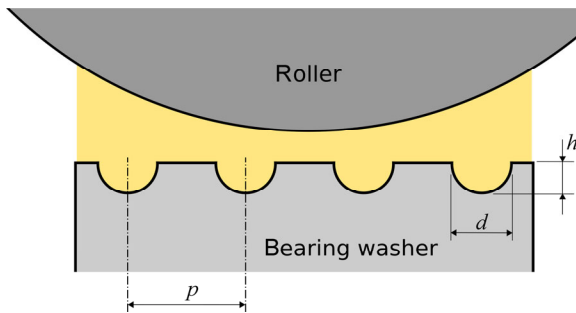
Fig. 1 A schematic of the profile of the laser textured surface in the lubricated contact condition; h shows the height from the valley to top, d shows the diameter of the holes or the ditches, and p shows the distance of the periodicity.

The applied energy fluence was measured as 12.7 J·cm^{-2}. The texturing position on the surface was manipulated by a programmable x-y motion controller, which moves the stage to the required position with a synchronized link to the laser shutter. The periodic distance between dimples was set as 200 and 500 μm. The parameters have been proven for friction reduction under the boundary lubrication regime [11]. It is noted that the stepping resolution of the stage movement in the x direction was limited, and this resulted in alternating 160 and 240 μm distances between dimples when setting the periodicity as 200 μm. Nevertheless, the average periodicity was measured as 200 μm.

Moreover, cross patterns were produced by DLIP, which uses interference for LST. A Nd:YAG nanosecond pulse laser (Quanta Ray Pro 290, Spectra Physics) was used with a wavelength of 532 nm, a pulse frequency of 10 Hz, and a pulse duration of 10 ns. The applied energy fluence was measured as 1.2 J·cm^{-2}. The primary laser beam was split into two sub-beams by a

50/50 beam-splitter. Subsequently, the two sub-beams were superposed onto the surface with a certain incident angle, which creates the interference patterns. The incident angle is used to control the periodic distance of the line patterns. The cross pattern can be finally produced by an additional laser shot at the same position with a 90° of rotation. More details of the DLIP setup can be found in the previous study [29]. Furthermore, the surface topography was then evaluated by using a white light interferometer (WLI, Zygo NewView 7300).

2.2 Rolling bearing test rig

A test rig FE8 according to DIN51819-1 was used for both an initial wear evaluation of all four textures plus reference sample, and then for a fatigue lifetime assessment of the best-performing textured sample (that showed minimum wear). For the initial wear tests, commercial thrust cylindrical roller bearings (Type 81212) were installed with a horizontal axis of rotation. The bearings are made of steel 100Cr6 (AISI 52100), and the roughness R_a of the washers was measured as 0.06 μm. The LST patterns were manufactured onto the surfaces of the bearing washers. Base oil ISO VG 100 mixed with ZDDP as an additive of C3C4-alkyl-chain with 0.05 wt% P was used in a 2 hours test; the load, rotational speed, and working temperature were set as 80 kN, 20 rpm, and 60 °C, respectively. The lubrication condition based on the film thickness was calculated according to Dowson et al. [30, 31]. The lambda values of the experiments were between 0.04 and 0.12, indicating that all the tests were conducted under boundary lubrication conditions [32]. Further information on the experiments can be found in Table 2. After the test, the surface was rinsed with benzene and isopropanol to clean the residual oil, abrasives, and contaminants. The wear tracks were measured by WLI.

For the fatigue lifetime evaluation, thrust ball bearings (Type 51212) were used in place of the roller bearings. Despite the plane surface of the roller bearings being more suitable for LST, ball bearings

Table 2 Experimental details and lubricant properties of the tribological tests by using an FE8 test rig.

Experimental parameters			Oil properties at 60 °C		
Rolling speed	Max. pressure	Temp.	Kinematic viscosity	Density	Pressure-viscosity coefficient
0.04 m/s	1.92 GPa	60 °C	38.3 mm^2/s	869.1 kg/m^3	1.82×10^{-8} Pa^{-1}

were chosen to avoid wear loss by shearing. The rolling motion of the balls features only a small amount of sliding (in comparison to the cylindrical rollers), and thus minimizes abrasive and adhesive wear. This helps ensure that the fatigue life would predominantly be determined by pitting failure alone.

The same test rig and the same ZDDP-containing oil were used. The test conditions were set as 80 kN, 750 rpm, and 90 °C, thus a significant increase in rotational speed compared to the initial tests but maintaining the same applied load. The tests were stopped as soon as surface damage (either on a ball or a washer) was detected by a vibration sensor. Further information on the fatigue experiments can be found in Table 3.

2.3 Contact simulation

The normal contact between each bearing surface and a roller was modelled, using boundary elements, to estimate the contact pressures and contact areas for each different surface pattern. The analysis used a 3D surface profile of the textured and reference samples, with a smooth cylindrical roller counterbody. The model assumes a homogeneous half-space for each surface and uses an iterative conjugate-gradient method to obtain valid contact pressures for the imposed loading [33].

A 3D profile of a section of the textured or reference bearing surface was measured using WLI to provide a representative surface for analysis of 640 × 480 nodes. Since the measured surface area did not enclose the full roller-washer contact, the measured surface was expanded by mirroring and tiling the surface profile data. This helps avoid edge effects at the ends of the roller (or solution domain) while maintaining realistic contact behavior. Results for the contact pressures and contact area were subsequently obtained over the original, as-measured profile only. The simulation was restricted to an elastic analysis without any plasticity considerations; whilst this does lead to some excessive localized pressures, it does enable an appropriate comparison of the extent of loading stresses

without complications associated with the hardness of the laser-modified surfaces.

3 Results and discussions

3.1 Morphology of the laser textured surfaces

The surface topography profiles of the LST patterns are shown in Fig. 2, and the details of the profile are listed in Table 1. The dimple patterns produced by femtosecond pulsed laser are shown in Figs. 2(a) and 2(b). The dimples are distributed with a periodicity of 500 and 200 μm, whereas the cross patterns are shown in Figs. 2(c) and 2(d) with periodicity of 9 and 30 μm. The samples are subsequently referred to as Dimple500, Dimple200, Cross9, and Cross30, respectively. Further, the profile is similar to a sine wave with a height of approximately 1 μm. The roughness parameters listed in Table 4 show an increase of surface roughness by LST for all geometries. The patterns with shorter periodic distance have greater values of S_a and S_q. Since the LST structural height is larger than the untextured roughness, the higher concentration of patterns increases the mean roughness value, which theoretically causes higher contact stress. However, the capacity of lubricant storage may not be directly obtained by the mean roughness values such as S_a. Additional topographical parameters were thus calculated to describe the ability of lubricant storage.

The bearing ratio curve, which is also known as Abbott-Firestone curve, represents the height distribution of the laser patterns in Fig. 3. The curves of the dimple patterns (see Fig. 3(a)) have a similar shape to the untextured reference surface, which indicates a geometrical similarity. This is expected because the surface is only modified at dimple locations and most of the surface remains nearly unchanged. However, the higher value at both ends represents a larger volume near the topographical maximum and minimum, caused by concentrated sharp edges of the dimples. Therefore, shorter LST periodic distance was associated with greater values of S_{pk} and S_{vk}. In contrast, the bearing ratio curves of the cross patterns,

Table 3 Experimental details and lubricant properties of the fatigue tests by FE8 test rig.

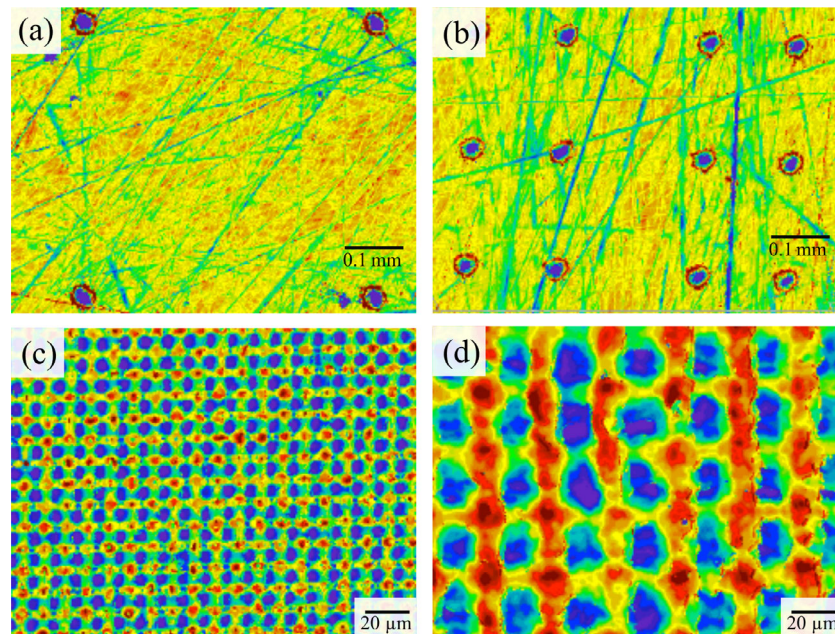| Experimental parameters			Oil properties at 90 °C		
Rolling speed	Max. pressure	Temp.	Kinematic viscosity	Density	Pressure-viscosity coefficient
1.53 m/s	3.5 GPa	90 °C	13.6 mm^2/s	850.8 kg/m^3	1.50×10^{-8} Pa^{-1}

Fig. 2 Surface topography profiles of the LST patterns on the washers of bearings. The dimple pattern was made by femtosecond pulsed laser with a periodicity of (a) 500 µm and (b) 200 µm; the cross pattern was made by DLIP with a periodicity of (c) 9 µm and (d) 30 µm.

Table 4 Roughness and bearing ratio parameters of the surface by laser surface texturing[*].

	S_a	S_q	S_k	S_{pk}	S_{vk}	A_p	A_v
Reference	0.06	0.08	0.18	0.12	0.11	0.003	0.006
Dimple500	0.09	0.16	0.13	0.33	0.30	0.008	0.009
Dimple200	0.15	0.25	0.24	0.46	0.45	0.015	0.013
Cross9	0.32	0.39	1.04	0.28	0.20	0.008	0.008
Cross30	0.27	0.33	0.68	0.27	0.18	0.007	0.007

[*]All values are shown in µm.

S_a—Arithmetic average height; S_q—Root mean square deviation; S_k—Core roughness depth; S_{pk}—Reduced peak height; S_{vk}—Reduced valley depth; A_p—Material volume in peak zone; A_v—Void volume in valley zone.

shown in Fig. 3(b), indicate a clear difference to the reference samples. The slopes are higher compared to the dimples, indicating a larger topographical variation over the total surface. Compared to the dimple patterns, which were still similar to the reference surface, the cross patterns had modified the surface more significantly.

In Table 4, the dimple patterns present larger values of S_{vk}, the valley height of the profile, whereas the cross patterns show greater values of S_k, the core height of the profile. It has been suggested that the S_{vk} value extracted from a bearing ratio curve is a suitable index of the ability for lubricant storage [34]. An increase of S_{vk} indicates a larger valley area, which provides space that acts as a reservoir. When comparing only S_{vk} values, the dimple patterns could

retain more lubricant than the cross samples. However, when the overall geometry differs between the two pattern types, the assessment of lubricant storage should involve both S_k and S_{vk}. Therefore, the possible storage space within the core height S_k can be also inlcuded. It is noted that the values of peak and valley area, A_v and A_p, show a similar tendency to the S_{pk} and S_{vk} values.

3.2 Wear performances of LST samples

In Fig. 4, the mass and volume loss of the bearing after testing is shown, revealing the extent of wear of the bearings. The volume loss is an average value obtained from WLI measurements. It can be seen that all of the laser patterns showed less wear loss than the untextured pristine specimens, which can be
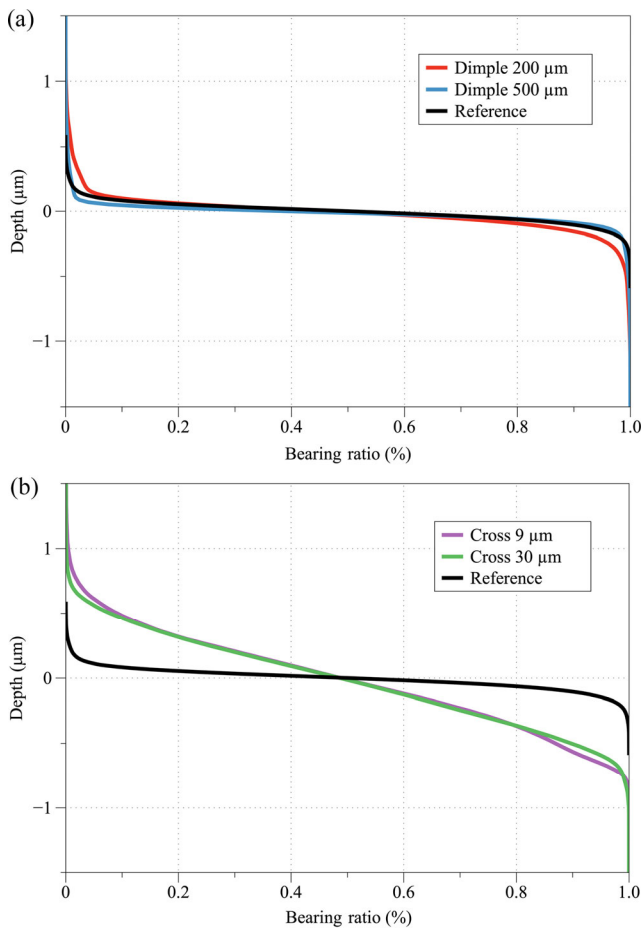
Fig. 3 The Abbott-Firestone curves of (a) the dimple patterns by femtosecond pulsed laser with a periodicity of 200 and 500 µm; (b) the cross patterns by DLIP with a periodicity of 9 and 30 µm.
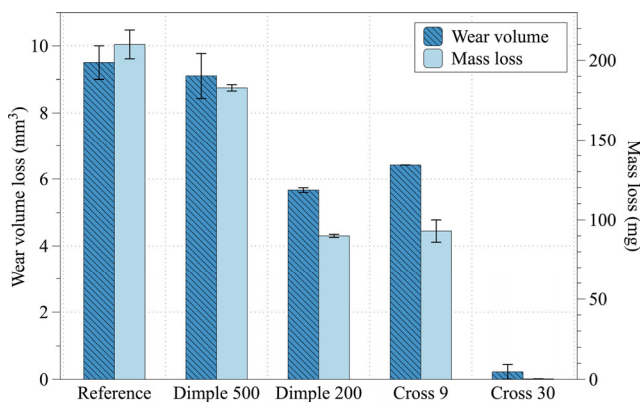

Fig. 4 Wear measurement of the bearings after tribotests in volume loss and mass loss.

attributed to the lubricant storage capability of the textured surface. Only mild wear was measured on sample Cross30, which indicates a significant wear protection by LST.

The sample Cross30 has a wear reduction of

two orders of magnitude compared to all the other samples. The reasons for this significant reduction are presumably due to two points. Firstly, the surface patterns act as lubricant reservoirs, which supports lubrication when encountering starved situations. Both types of patterns can retain lubricants in the valleys, but the cross patterns have an increased capacity, which was shown by the aforementioned bearing ratio curve. Secondly, a fully-established ZDDP antiwear tribofilm was observed on the Cross30 sample. The tribofilm can be also found on Cross9 and Dimple200, but the wear tracks were only partially covered by the protecting tribofilm due to a higher wear rate, since the antiwear mechanism is in a dynamic equilibrium between chemical formation and mechanical removal [8]. The tribofilm on Cross30 was identified completely covering the contact area, indicating the growth rate was sufficient to mitigate wear. More characterization details have been published by Hsu et al. [27] in a previous paper, which indicated that the formation of tribofilm can be encouraged by the LST patterns. In summary, the combination of lubricant retention and tribofilm generation appears to reduce wear for all textures but is most effective with the Cross30 pattern.

3.3   Contact simulation

To better understand the causes of the tribofilm formation on the bearings, the pressure distribution was analyzed by contact simulation. According to a series of *in-situ* measuring experiments by Gosvami et al. [22], the growth rate of tribofilm increases five-fold when increasing the contact pressures from 3 to 5 GPa, and the formation rate will be saturated above around 6.5 GPa. Consequently, each node from the simulation results has been classified by pressure value range. The parts of the contact area that experience normal stress between 3 and 7 GPa are expected to be suitable for the formation of the protecting tribofilm.

The area of contact for the Dimple200 and Cross30 samples is shown in Fig. 5 and the overall contact area coverage for all samples is represented in Fig. 6(a). In Fig. 6(b), the proportion of the nodes that experience contact pressures in the indicated ranges is presented. The pressure distribution on the dimple patterns is similar to the untextured reference, and higher stress can be found surrounding the dimples. When the
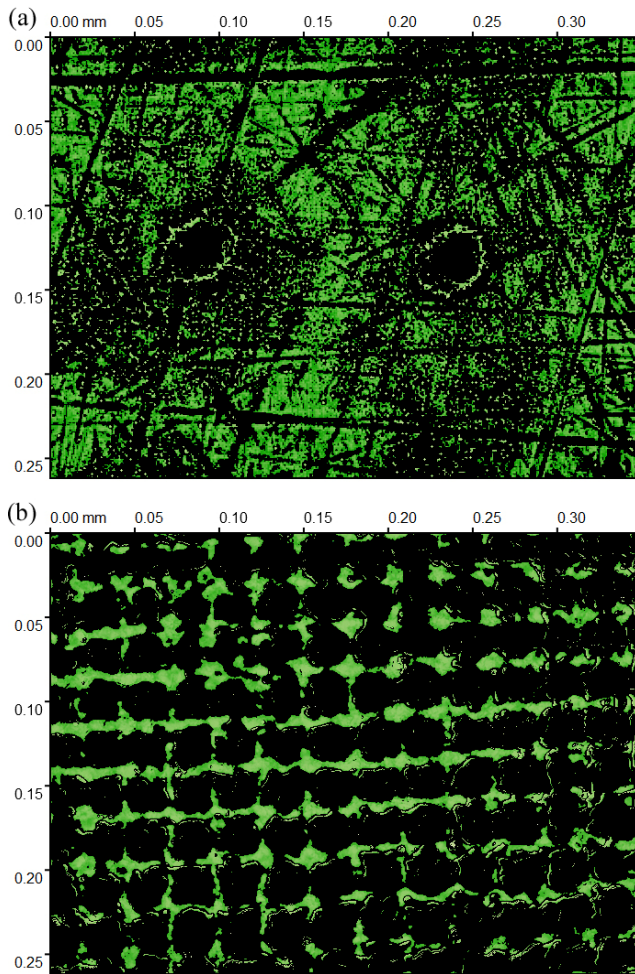
Fig. 5 The contact area of the bearing washers by the results of the contact simulations of (a) the dimple pattern with the periodicity of 200 μm and (b) the cross pattern with the periodicity of 30 μm. The contact area is shown in green.

Fig. 6 The coverage of the contact area on the patterned surfaces and the reference by BEM simulation (a), and the proportion of the contact pressure within the contact area (b). (*P*: contact pressure in GPa)

periodic interval decreases from 500 to 200 μm, the total contact area decreases. The topographical spikes observed around the dimples, which were caused by the LST, lead to higher pressure spikes which affect the full pressure distribution. This increase of contact pressure can be identified by the shift of the histogram chart to the right. The cross patterns are shown to have more higher-pressure regions due to the overall smaller contact area. Again, the shape of the histogram chart shifts to the right, indicating a greater area with high contact pressure. Compared to the dimples, the cross patterns demonstrated a greater difference in contact geometry with respect to the untextured sample. With the cross patterns, the effect of pattern geometry dominates over the surface roughness in controlling the contact stress.
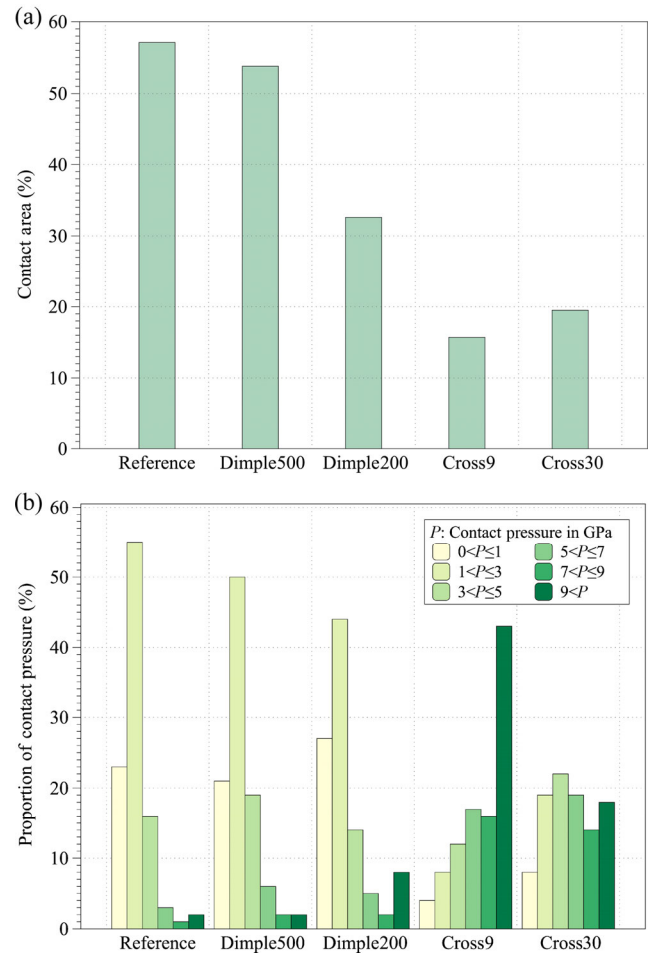
Despite the growth rate of tribofilm increasing when the contact pressure is greater, higher contact stress can also cause more wear. The pattern Cross9 has a distinct peak showing a high percentage of nodes with pressure greater than 9 GPa (see Fig. 6(b)). While both of the cross patterns have higher contact pressure, especially in the range between 5 to 7 GPa, the pressure value of Cross9 was probably beyond the optimum pressure range for ZDDP promotion, thus leading to a higher wear rate. On the contrary, Cross30 enhanced the formation of tribofilm with sufficient pressures, but without the excessive pressures that would further increase wear.

3.4 Fatigue lifetime evaluation

Following the results of the wear evaluation, the

Cross30 textured sample was selected for the fatigue lifetime experiments. Compared to the reference (untextured) bearings, no macroscopic abrasive or adhesive wear was observed on the wear track, and only pitting cracks could be found, as shown in Fig. 7. Fatigue damages occurred on either the washers or the balls, and the contour of the laser patterns can still be identified. A comparison of the fatigue lifetime by using the Weibull distribution is shown in Fig. 8. The Weibull slopes of the reference and Cross30 are similar, being 1.3 and 1.37, respectively. Since the distributions are parallel to each other, the damage mechanisms for both surface types are identical. Compared to the reference, the slope of Cross30 shifts to the right, indicating an increase of fatigue lifetime by a factor of three. Furthermore, the values were in accordance with the slope expected for cases of RCF [2].

The use of LST in rolling element bearings is still rare compared to other machine components, due to concern about their potential detrimental effect on RCF life [12]. It is evident that the increase of surface roughness by LST (see Table 4) can lead to higher contact stresses. However, the test results show no negative effect on the fatigue lifetime of the ball
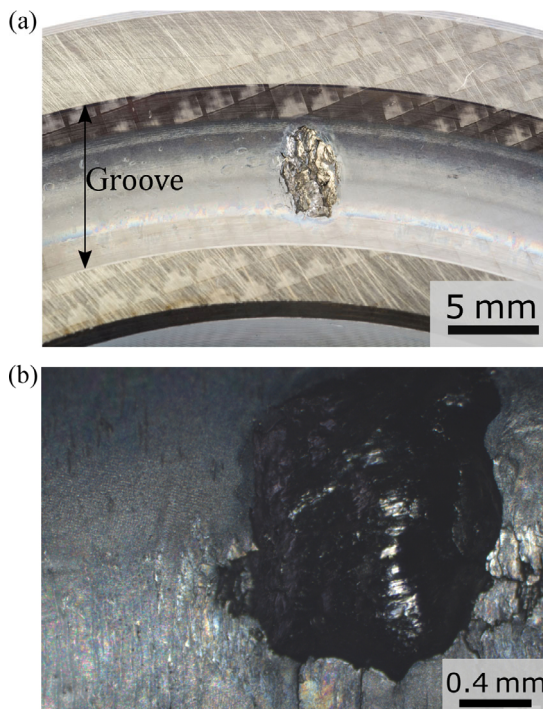

Fig. 7 Pitting damage on Cross30 of the fatigue test (a), and an enlargement (b). The pit occurred in the groove of a bearing washer with a diameter of approximately 3 mm.
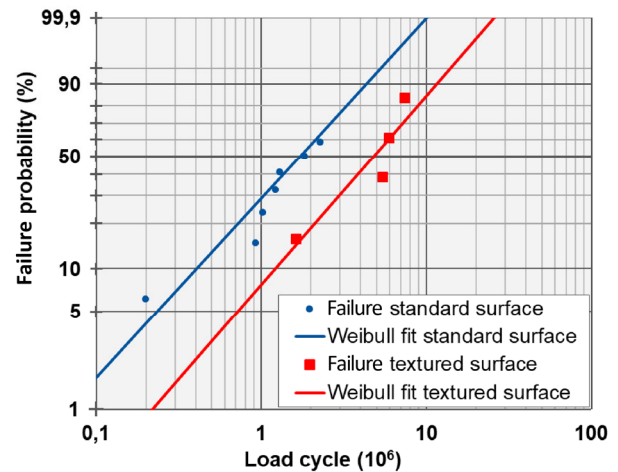

Fig. 8 Weibull distribution of the fatigue tests of the reference and the Cross30 laser textured thrust rolling bearing.

bearings. In contrast to the concerns, the LST surfaces achieved a significantly longer fatigue lifetime, and with better wear protection. Therefore, the use of LST in ball and roller bearings should be considered, with the aid of further investigations into their use under different operating conditions and geometries.

Although friction is generally one of the main factors for the occurrence of RCF, there was no notable difference between Cross30 and the reference, with the values of friction coefficient being in the same range for both cases. Accordingly, the longer RCF life can be attributed to the enhancement of the anti-wear tribofilm formation and the capacity of the textured pockets that supplied sufficient lubrication.

4   Conclusions

In summary, the LST patterns make the surface able to retain lubricants within the contact, which ensures sufficient lubrication under such high-load conditions. Furthermore, the growth of the ZDDP tribofilm promoted by LST prevents direct contact between surfaces that reduce wear.

The conclusions for the tribological performance based on the tests and simulations carried out are:

1) A three-fold increase in fatigue lifetime was demonstrated for the laser textured thrust rolling bearings with cross periodic patterns. This is attributed to the ability of the LST patterns to retain lubricants within the contact, which ensures sufficient lubrication under such high-load conditions, combined with

the enhanced formation of the ZDDP tribofilm that prevents direct contact between surfaces. LST has been proven to reduce wear of roller bearings in the boundary lubrication regime.

2) Geometry and area density of the laser patterns alter the tribological performances. A higher area density of the patterns leads to a higher roughness, and thus higher contact stresses. Both the S_k and S_{vk} parameters of the Abbott-Firestone curve (rather than S_{vk} alone) should be involved for assessing the ability for lubricant storage when the geometry of the LST patterns is different.

3) An increase of the contact pressure enhances the formation of ZDDP tribofilm on the cross patterns. However, high LST area density led to excessively high contact stress at the texture peaks, negating the beneficial effect and causing a higher wear rate.

Acknowledgements

References

[1] Rycerz P, Olver A, Kadiric A. Propagation of surface initiated rolling contact fatigue cracks in bearing steel. *Int J Fatigue* **97**: 29–38 (2017)

[2] Sadeghi F, Jalalahmadi B, Slack T S, Raje N, Arakere N K. A review of rolling contact fatigue. *J Tribol* **131**: 041403 (2009)

[3] Johnson K L, Keer L M. Contact Mechanics. *J Tribol* **108**: 659 (1986)

[4] Richard Booser E. *Tribology Data Handbook.* 2010

[5] Hsu S M. Boundary lubrication: Current understanding. *Tribol Lett* **3**: 1–11 (1997)

[6] Etsion I. State of the Art in Laser Surface Texturing. *J Tribol Trans ASME* **127**: 248–253 (2005)

[7] Gachot C, Rosenkranz A, Hsu S M, Costa H L. A critical assessment of surface texturing for friction and wear improvement. *Wear* **372–373**: 21–41 (2017)

[8] Spikes H. The history and mechanisms of ZDDP. *Tribol Lett* **17**: 469–489 (2004)

[9] Martin J M, Grossiord C, Le Mogne T, Igarashi J. Transfer films and friction under boundary lubrication. *Wear* **245**: 107–115 (2000)

[10] Erdemir A. Review of engineered tribological interfaces for improved boundary lubrication. *Tribol Int* **38**: 249–256 (2005)

[11] Kovalchenko A, Ajayi O, Erdemir A, Fenske G, Etsion I. The effect of laser surface texturing on transitions in lubrication regimes during unidirectional sliding contact. *Tribol Int* **38**: 219–225 (2005)

[12] Rosenkranz A, Grützmacher P G, Gachot C, Costa H L. Surface Texturing in Machine Elements−A Critical Discussion for Rolling and Sliding Contacts. *Adv Eng Mater* **21**: 1900194 (2019)

[13] Rosenkranz A, Stratmann A, Gachot C, Burghardt G, Jacobs G, Mücklich F, et al. Improved wear behavior of cylindrical roller thrust bearings by three-beam laser interference. *Adv Eng Mater* **18**: 854–862 (2016)

[14] Rosenkranz A, Martin B, Bettscheider S, Gachot C, Kliem H, Mücklich F. Correlation between solid-solid contact ratios and lubrication regimes measured by a refined electrical resistivity circuit. *Wear* **320**: 51–61 (2014)

[15] Wang Z, Gu L, Li L. Experimental studies on the overall

efficiency performance of axial piston motor with a laser surface textured valve plate. *Proc Inst Mech Eng Part B J Eng Manuf* **227**: 1049–1056 (2013)

[16] Ryk G, Kligerman Y, Etsion I. Experimental investigation of laser surface texturing for reciprocating automotive components. *Tribol Trans* **45**: 444–449 (2002)

[17] Bancroft G M, Kasrai M, Fuller M, Yin Z, Fyfe K, Tan K H. Mechanisms of tribochemical film formation: Stability of tribo- and thermally-generated ZDDP films. *Tribol Lett* **3**: 47–51 (1997)

[18] Zhang Z, Yamaguchi E S, Kasrai M, Bancroft G M. Tribofilms generated from ZDDP and DDP on steel surfaces: Part 1, growth, wear and morphology. *Tribol Lett* **19**: 211–220 (2005)

[19] Stratmann A, Jacobs G, Hsu C-J, Gachot C, Burghardt G. Antiwear tribofilm growth in rolling bearings under boundary lubrication conditions. *Tribol Int* **113**: 43–49 (2017)

[20] Gachot C, Hsu C, Suárez S, Grützmacher P, Rosenkranz A, Stratmann A, Jacobs G. Microstructural and Chemical Characterization of the Tribolayer Formation in Highly Loaded Cylindrical Roller Thrust Bearings. *Lubricants* **4**: 1–11 (2016)

[21] Martin J M, Onodera T, Minfray C, Dassenoy F, Miyamoto A. The origin of anti-wear chemistry of ZDDP. *Faraday Discuss* **156**: 311 (2012)

[22] Gosvami N N, Bares J A, Mangolini F, Konicek A R, Yablon D G, Carpick R W. Mechanisms of antiwear tribofilm growth revealed in situ by single-asperity sliding contacts. *Science* **348**: 102–106 (2015)

[23] Rosenkranz A, Grützmacher P G, Murzyn K, Mathieu C, Mücklich F. Multi-scale surface patterning to tune friction under mixed lubricated conditions. *Appl Nanosci* **11**: 751–762 (2019)

[24] Etsion I, Halperin G, Brizmer V, Kligerman Y. Experimental investigation of laser surface textured parallel thrust bearings. *Tribol Lett* **17**: 295–300 (2004)

[25] Vlǎdescu S C, Olver A V., Pegg I G, Reddyhoff T. Combined friction and wear reduction in a reciprocating contact through laser surface texturing. *Wear* **358–359**: 51–61 (2016)

[26] He D, Zheng S, Pu J, Zhang G, Hu L. Improving tribological properties of titanium alloys by combining laser surface texturing and diamond-like carbon film. *Tribol Int* **82**: 20–27 (2015)

[27] Hsu C-J, Stratmann A, Rosenkranz A, Gachot C. Enhanced Growth of ZDDP-Based Tribofilms on Laser-Interference Patterned Cylinder Roller Bearings. *Lubricants* **5**: 39 (2017)

[28] Vrbka M, Šamánek O, Šperka P, Návrat T, Křupka I, Hartl M. Effect of surface texturing on rolling contact fatigue within mixed lubricated non-conformal rolling/sliding contacts. *Tribol Int* **43**: 1457–1465 (2010)

[29] Lasagni A, Holzapfel C, Weirich T, Mu F, Mücklich F. Laser interference metallurgy: A new method for periodic surface microstructure design on multilayered metallic thin films. *Appl Surf Sci* **253**: 8070–8074 (2007)

[30] Dowson D, Higginson G R, Whitaker A V. Elasto-hydrodynamic lubrication: A survey of isothermal solutions. *J Mech Eng Sci* **4**: 121–126 (1962)

[31] Lubrecht A A, Venner C H, Colin F. Film thickness calculation in elasto-hydrodynamic lubricated line and elliptical contacts: The Dowson, Higginson, Hamrock contribution. *Proc Inst Mech Eng Part J J Eng Tribol* **223**: 511–515 (2009)

[32] Stratmann A, Jacobs G, Hsu C, Gachot C, Burghardt G. Antiwear tribo film growth in rolling bearings under boundary lubrication conditions. *Tribol Int* **113**: 43–49 (2017)

[33] Polonsky I A, Keer L M. A numerical method for solving rough contact problems based on the multi-level multi-summation and conjugate gradient techniques. *Wear* **231**: 206–219 (1999)

[34] Petropoulos G P, Torrance A A, Pandazaras C N. Abbott curves characteristics of turned surfaces. *Int J Mach Tools Manuf* **43**: 237–243 (2003)

Chia-Jui HSU. He is a tribologist doing research at Vienna University of Technology. He has a background in both mechanical engineering and material science. His current study is focusing on surface engineering, particularly on laser surface texturing and antiwear tribofilm. Moreover, microstructural and chemical characterization methods such as SEM, Raman, and nano-indentation are also his expertise.